Wetting, Diffusion and Active Motion of Colloidal Particles at the Fluid Interface

Antonio Stocco

Université de Montpellier

Habilitation à Diriger des Recherches

Spécialité : Physique

Ecole doctorale : I2S (Information, Structures, Systèmes)

Wetting, Diffusion and Active Motion of Colloidal Particles at the Fluid Interface

Antonio Stocco

Laboratoire Charles Coulomb (L2C), UMR-5221

Soutenu le 11 Décembre 2018 devant le jury composé de :

M.	**Martin IN**	**Président du jury**
M.me	**Cécile COTTIN-BIZONNE**	**Rapporteur**
M.	**Colin BAIN**	**Rapporteur**
M.	**Hans-Jürgen BUTT**	**Rapporteur**
M.me	**Véronique SCHMITT**	**Examinateur**
M.	**Maurizio NOBILI**	**Examinateur**

I dedicate this dissertation to my family,
my mentor Helmuth Möhwald (1946-2018),
and my mother Fina Gattuso (1941-2014),
who have always encouraged me.

Contents

Track record

I am an experimentalist working in physics and physical chemistry of interfaces, wetting, active colloids, nanoparticles, amphiphilic polymers and surfactants. I obtained my PhD in Physical Chemistry in 2007 (Max Planck Institute of Colloids and Interfaces, Potsdam University, Germany) and in the last 11 years I have developed my research designing new experimental setups, investigating complex or simple soft matter systems showing unexpected interactions and dynamics.

Understanding and controlling particle-interface interactions and dynamics is one of my main research goals. During my PhD, I designed and built an experimental setup, which combined ellipsometry and evanescent wave dynamic light scattering at the gas-liquid and liquid-liquid interfaces (i.e. fluid interfaces). The translational diffusion of nanoparticles and polymers adsorbed at the fluid interfaces was measured for the first time without the need of using fluorescence based systems. A slowing down of the translational diffusion coefficient of nanoparticles at the interface was measured, which could not be explained by current hydrodynamic models. In Boniello et al. (Nature Materials, 2015), a systematic investigation of the slowing down of the translational and rotational diffusions of partially wetted colloids at the gas-liquid interface allowed us to introduce a new form of friction due to the three phase contact line fluctuations. This new interfacial friction allows to interpret previous and current experimental unexpected results for nanoparticles, colloids and microswimmers at the fluid interfaces.

Starting from my PhD, I have also used ellipsometric and light reflectivity experiments, which I have been continuing to use, to reveal new phenomena on: (i) the interfacial structure of bare interfaces, (ii) to assess the contact angle of nanoparticles adsorbed at the liquid-gas or liquid-liquid interfaces, (iii) and the roughness of fluid interfaces induced by MHz ultrasound.

During my postdoc in 2008-2009, I worked with Dominique Langevin (Laboratoire de Physique des Solides, Orsay, France) on fumed silica nanoparticles at the gas-water interfaces and investigated the static and dynamic properties of aqueous foams made solely of water and nanoparticles in absence of surfactants or any other surface active species. Simple interfaces, liquid films, bubbles and macroscopic foams were studied by a combination of techniques including advanced methods such as x-ray microtomography and diffusing wave spectroscopy. By measuring the structure and dynamics of the bubbles inside the foams and of particles at the interface, we elucidated on the remarkable long time stability of these particle stabilised foams.

During my postdoc in 2010, I worked with Dayang Wang and Helmuth Möhwald (Max Planck Institute of Colloids and Interfaces, Potsdam, Germany) on the bidirectional phase transfer of stimuli responsive nanoparticles across oil-water interfaces. Recently in collaboration with H. Mutin and coworkers (ICG, Montpellier), I have also investigated the phase transfer of nanoparticles across ionic liquid-fluid interfaces. Both wetting and colloidal forces play important roles in these experimental systems, whose dynamics is dictated by the Brownian motion, surface forces and wetting transitions.

In October 2011 as a CNRS researcher, I started to work at the Laboratoire Charles Coulomb in Montpellier and I began a new activity in the lab on active colloids: particles able to self-propel and move autonomously over distances much longer than the ones of thermal Brownian motion. I have also obtained funding to install equipment and develop many activities on fluid interfaces, which were not present in the lab before. I have also worked to bridge the Chemistry and Physics communities in Montpellier. I have participated in the Labex Chemisyst (Chemistry) and Numev (Physics) and I have organized workshops involving both communities on: (i) particle stabilised emulsions and foams, (ii) water treatment, and (iii) ultrasounds for phase transfer. In collaboration with Maurizio Nobili, Martin In and Christophe Blanc, I have developed independently my research in Montpellier on passive and active Janus colloids at the fluid interface investigating fundamental aspects and applications. We have performed dedicated experiments in order to elucidate on the coupling between the active motion and partial wetting dynamics. In terms of applications, one recent project I have been developing makes use of the enhanced transport properties of active porous colloids to decontaminate the surface of water.

Publication List

35) The Central Role of Bicarbonate Anions in Charging Water/Hydrophobic Interfaces,
X Yan, M Delgado, J Aubry, O Gribelin, A Stocco, F Boisson-Da Cruz, J Bernard, F Ganachaud,
Journal Physical Chemistry Letters, 9, 96–103 (2018)

34) Janus colloids actively rotating on the surface of water,
X Wang, M In, C Blanc, A Würger, M Nobili, A Stocco*,
Langmuir, 33 (48), 13766–13773 (2017)

33) Phase transfer of TiO_2 nanoparticles from water to ionic liquid triggered by phosphonic acid grafting
R Bhandary, JG Alauzun, P Hesemann, A Stocco, M In, PH Mutin,
Soft Matter, 13, 8023-8026 (2017)

32) A comparison between liquid drops and solid particles in partial wetting,
A Stocco*, M Nobili,
Advances in Colloid and Interface Science, 247C, 223-233 (2017)

31) Emulsion electro-oxidation of kraft lignin,
D Di Marino, V Aniko, A Stocco, S Kriescher, M Wessling,
Green Chemistry, 19, 4778-4784 (2017)

30) Comment on "Brownian diffusion of a particle at an air/liquid interface: elastic (not viscous) response of the surface",
G Boniello, A Stocco, C Blanc, M Nobili,
Physical Chemistry Chemical Physics 19 (33), 22592-22593 (2017)

29) Janus and patchy nanoparticles: general discussion, A Striolo et al., Faraday discussions 191, 117-139 (2016)

28) Wetting and orientation of catalytic Janus colloids at the surface of water,
X Wang, M In, C Blanc, P Malgaretti, M Nobili, A Stocco*,
Faraday discussions 191, 305-324 (2016)

27) MHz ultrasound induced roughness of fluid interfaces,
R Boubekri, M Gross, M In, O Diat, M Nobili, H Möhwald, A Stocco*,
Langmuir 32 (40), 10177-10183 (2016)

26) Translational viscous drags of an ellipsoid straddling an interface between two fluids,
G Boniello, A Stocco, M Gross, M In, C Blanc, M Nobili,
Physical Review E 94 (1), 012602 (2016)

25) Multiwalled carbon nanotube/cellulose composite: from aqueous dispersions to pickering emulsions,
C Avendano, N Brun, O Fontaine, M In, A Mehdi, A Stocco, A Vioux,
Langmuir 32 (16), 3907-3916 (2016)

24) Particles at interfaces: general discussion, A Striolo et al., Faraday discussions 191, 407-434 (2016)

23) Nanocomposites with both structural and porous hierarchy synthesized from Pickering emulsions,
C Avendano, N Brun, E Mourad, O Fontaine, CL Sarroste, M Baccour, M In, A Mehdi, A Stocco, A Vioux,
New Journal of Chemistry 40 (5), 4344-4350 (2016)

22) The influence of long-range surface forces on the contact angle of nanometric droplets and bubbles,
A Stocco*, H Möhwald,
Langmuir 31 (43), 11835-11841 (2015)

21) Brownian diffusion of a partially wetted colloid,
G Boniello, C Blanc, D Fedorenko, M Medfai, NB Mbarek, M In, M Gross, A Stocco, M. Nobili,
Nature Materials 14 (9), 908-911 (2015)

20) Droplet Liquid/Liquid Interfaces Generated in a Microfluidic Device for Assembling Janus Inorganic Nanohybrids,
N Hassan, A Stocco, A Abou-Hassan,
The Journal of Physical Chemistry C 119 (19), 10758-10765 (2015)

19) Enhanced active motion of Janus colloids at the water surface,
X Wang, M In, C Blanc, M Nobili, A Stocco*,
Soft Matter 11 (37), 7376-7384 (2015)

18) In situ assessment of the contact angles of nanoparticles adsorbed at fluid interfaces by multiple angle of incidence ellipsometry,
A Stocco*, G Su, M Nobili, M In, D Wang,
Soft Matter 10 (36), 6999-7007 (2014)

17) Thermodynamics and kinetics of mixed protein/surfactant adsorption layers at liquid interfaces, R Miller et al. Proteins in Solution and at Interfaces: Methods and Applications in in Biotechnology and Materials Science (2013)

16) Bidirectional Nanoparticle Crossing of Oil–Water Interfaces Induced by Different Stimuli: Insight into Phase Transfer,
A Stocco*, M Chanana, G Su, P Cernoch, BP Binks, D Wang,
Angewandte Chemie International Edition 51 (38), 9647-9651 (2012)

15) Interfacial rheology and conformations of triblock copolymers adsorbed onto the water–oil interface,
P Ramírez, A Stocco*, J Muñoz, R Miller,
Journal of colloid and interface science 378 (1), 135-143 (2012)

14) Dynamics of adsorption of polyallylamine hydrochloride/sodium dodecyl sulphate at water/air and water/hexane interfaces,
A Sharipova, S Aidarova, VB Fainerman, A Stocco, P Cernoch, R Miller,
Colloids and Surfaces A: Physicochemical and Engineering Aspects 391 (1), 112-118 (2011)

13) Dynamics of amphiphilic diblock copolymers at the air–water interface,
A Stocco*, K Tauer, S Pispas, R Sigel,
Journal of colloid and interface science 355 (1), 172-178 (2011)

12) Evanescent-wave dynamic light scattering at an oil-water interface: Diffusion of interface-adsorbed colloids,
A Stocco, T Mokhtari, G Haseloff, A Erbe, R Sigel, Physical Review E 83 (1), 011601 (2011)

11) Pickering emulsions stabilized by stacked catanionic micro-crystals controlled by charge regulation,
N Schelero, A Stocco, H Möhwald, T Zemb,
Soft Matter 7 (22), 10694-10700 (2011)

10) Two-mode dynamics in dispersed systems: the case of particle-stabilized foams studied by diffusing wave spectroscopy,

A Stocco, J Crassous, A Salonen, A Saint-Jalmes, D Langevin,
Physical Chemistry Chemical Physics 13 (8), 3064-3072 (2011)

9) Particle-stabilised foams: structure and aging,
A Stocco*, F Garcia-Moreno, I Manke, J Banhart, D Langevin,
Soft Matter 7 (2), 631-637 (2011)

8) Aqueous foams stabilized solely by particles,
A Stocco*, E Rio, BP Binks, D Langevin,
Soft Matter 7 (4), 1260-1267 (2011)

7) Interfacial behavior of catanionic surfactants,
A Stocco*, D Carriere, M Cottat, D Langevin,
Langmuir 26 (13), 10663-10669 (2010)

6) High-resolution ellipsometric studies on fluid interfaces,
A Stocco*, K Tauer,
The European Physical Journal E, 30, 431-438 (2009)

5) Dynamics at the air-water interface revealed by evanescent wave light scattering,
A Stocco*, K Tauer, S Pispas, R Sigel,
The European Physical Journal E, 29, 95-105 (2009)

4) Densification of oxide nanoparticle thin films by irradiation with visible light,
MF Bertino, B Smarsly, A Stocco, A Stark,
Advanced Functional Materials 19 (8), 1235-1240 (2009)

3) The solidification behavior of a PBT/PET blend over a wide range of cooling rate,
A Stocco, V La Carrubba, S Piccarolo, V Brucato,
Journal of Polymer Science Part B: Polymer Physics 47 (8), 799-810 (2009)

2) An ellipsometry study of silica nanoparticle layers at the water surface,
D Zang, A Stocco*, D Langevin, B Wei, BP Binks,
Physical Chemistry Chemical Physics 11 (41), 9522-9529 (2009)

1) Particle-stabilised foams: an interfacial study,
A Stocco*, W Drenckhan, E Rio, D Langevin, BP Binks,
Soft Matter 5 (11), 2215-2222 (2009)

*corresponding author

Curriculum Vitae

Antonio Stocco, CRCN (CR1) CNRS
Soft Matter Team, Laboratoire Charles Coulomb (L2C),
UMR 5521, Univ. Montpellier and CNRS
Email: Antonio.Stocco@umontpellier.fr

Personal Data:
Date of Birth: 1980
Place of Birth: Palermo, Italy
Nationality: Italian
Married, two children

Positions, Postdocs, PhD, education:

since 2016	CR1 CNRS Position, L2C, Montpellier, France
2014-2015	Alexander von Humboldt Research Fellowship for Experienced Researcher, DWI RWTH, Aachen, Germany.
2012-2016	CR2 CNRS Position, L2C, Montpellier, France.
2011	Post Doctorate Position, Helmholtz Zentrum Berlin (HZB), Berlin, Germany. Supervision: Dr. M. Russina.
2010	Post Doctorate Position, Max Planck Institute of Colloids and Interfaces, Department of Interfaces, Potsdam, Germany. Supervision: Prof. D. Wang, Prof. H. Möhwald.
2008-2009	Marie Curie (ITN) Postdoctoral fellow at the Laboratoire de Physique des Solides (University of Paris-Sud, Orsay). Supervision: Dr. D. Langevin.
2005-2007	PhD at Max Planck Institute of Colloids and Interfaces (Potsdam, Germany). Title: ”Amphiphilic block copolymers at the liquid-fluid interface, investigated by evanescent light scattering and ellipsometry”. Supervision: Dr. R. Sigel, Prof. M. Antonietti.
1999-2004	Degree in Chemical Engineering at University of Palermo (5-year degree) with top marks (110/110). Title of the Thesis: ”Solidification behaviour of a commercial blend PBT/PET. Comparison and modeling with constituents”. Founded by DSM Research (Geleen, Netherlands). Coordinator: Prof. S. Piccarolo.

Publications:

- Peer-reviewed papers in scientific journals/books indexed by ISI: 35
- Communications as presenting author in scientific meetings: 23
- Number of invited conferences: 6
- Number of invited seminars: 21

Researchgate profile: https://www.researchgate.net/profile/Antonio_Stocco
Google Scholar profile: https://scholar.google.fr/citations?user=2G2I_6UAAAAJ&hl=fr

Fields of Research:

- Active colloids
- Wetting
- Interfaces, Emulsions and Foams
- Nanoparticles and Polymers
- Interfacial Optical methods

Supervision:

• X. Wang (PhD student): “Motion of Active Colloids at the Fluid Interface” (2012-2015). Co-supervisor: Martin In.

• R. Boubekri (Postdoc): “Transfer of particles through liquid-liquid interface assisted by ultrasounds” (2013-2014). Co-supervisors: Olivier Diat and Helmuth Möhwald.
• E. Azar (Postdoc): “Cleaning the surface of water by active porous colloids” (2017-2018). Co-supervisor: Maurizio Nobili.
• M. Oubalouk (Master student): “The viscosity of a surface” (2017). Co-supervisor: Laurence Ramos.

Co-supervision:

• D. Zang (PhD student): “Silica particles at the air-water interface” (2008),
• M. Cottat (Master student): “Interfacial behaviour of Catanionic surfactants” (2009),
• A. Sharipova (PhD student): “Adsorption of polyelectrolytes/surfactants at the fluid interface” (2010),
• C. Avendano (Postdoc): “Carbon nanotube Pickering emulsions” (2014),
• G. Boniello (PhD student): “Brownian motion of partially wetted colloids” (2012-2014),
• R. Bahndary (Postdoc): “Phase transfer of TiO_2 nanoparticles across ionic liquid-fluid interfaces” (2016-2017),
• B. Chollet (Postdoc): “Diffusions of Janus colloids at the interface” (2016-2017),
• A. Poirier (PhD student): “Interfacial behaviour of plant based proteins” (2016-2018),
• S. Villa (PhD student): “Diffusion dynamics of colloids close to liquid-gas interfaces” (2015-2018).

Fellowships and Funding:

• “Post-laurea” fellowship, University of Palermo, Italy (MPIKG, Potsdam, 2007).
• Funding for a PhD position (X. Wang), Scientific Council University Montpellier 2 (2012-2015).
• Funding for 1.5 year postdoc position (R. Boubekri), Labex Chemisyst. PI: Olivier Diat (2013-2014).
• Funding for equipment, Labex Numev (2013).
• “Alexander von Humboldt” Fellowship for Experienced Researcher (RWTH, Aachen, 2014-2015).
• Participation (15 person.month) in “Assembly and dynamics of active and passive micro-ellipsoids at a fluid interface”, ANR. PI: Maurizio Nobili (11/2014-10/2018).
• Participation (3 hours/month) in “A soft matter approach for thickening liquid oils”, Pivert. PI: Martin In (10/2015-04/2019).
• Funding for 1 year postdoc position (E. Azar), University Montpellier and Labex Chemisyst. PI: Maurizio Nobili (2017-2018).
• Funding for 1 year postdoc position, EMERGENCE@INC, CNRS (2018-2019).

Collaborators:

Alois Würger (LOMA, Bordeaux, France),
Paolo Malgaretti (MPI-IS, Stuttgart, Germany),
Helmuth Möhwald (MPI-KG, Potsdam, Germany),
Dayang Wang (Jilin University, Changchun, China),
Ali Abou-Hassan (UPMC, Paris, France),
Davide Di Marino (RWTH, Aachen, Germany),
Francois Ganachaud (INSA, Lyon, France),
Veronique Pimienta (IMRCP, Toulouse, France),
Hubert Mutin, Ahmad Mehdi, Andre Vioux (ICG, Montpellier France),
Marc Héran (IEM, Montpellier, France),
Benjamin Nottelet, Hervé Cottet (IBMM, Montpellier, France).

Experimental skills:

Skills in the use of the following techniques for the characterization of colloidal materials, interfaces and dispersions: static and dynamic light scattering, diffusing wave spectroscopy, surface light scattering, ellipsometry, interfacial tension and rheology, contact angle measurements, particle tracking videomicroscopy, optical microscopy, calorimetry, AFM, SEM, UV-vis spectroscopy.

Computer skills:

Good skills on data analysis, programming and fitting procedures. Origin, C, C++, IDL.

Peer Reviewing Activity:

Peer-review expertise for: Agence Nationale de la Recherche (ANR) and “Research in Paris”. Reviewing of scientific papers in the following journals: Langmuir, Soft Matter, Physical Chemistry Chemical Physics, Advanced in Colloid and Interface science, Journal of Colloid and Interface Science, European Physical Journal E, Colloids and Surfaces A.

Conference Organizing Committee:

• International Workshop “New Horizons of Colloidal Science” Sète (2012).
• Labex Numev Workshop “Water Treatment: Fundamentals and Applications”, Montpellier (2014).
• Labex Chemisyst Workshop “Ultrasounds and Fluid Interfaces”, Montpellier (2014).
• Workshop “Soft Matter and Glasses days”, Montpellier (2013 and 2016).
• MonToulouse - Workshop on Soft Matter research conducted in Toulouse and in Montpellier, Montpellier (2017).

Collective and Administrative responsibilities:

• Soft Matter Team seminars (2012-2014)
• Soft Matter Team website (2012-2017)
• Elected member of the administration council of “La ComUE Languedoc-Roussillon Universités” (2017-2018)

Teaching:

Semester course “Fundamentals of Interface and Colloid Science”. Faculty of Physics, Potsdam University (2007).

Language Competences:

English (speak, read, and write fluently), German (speak and read good, write intermediate knowledge), French (speak and read good, write intermediate knowledge), Italian (native language).

Other skills:

Good organization. High communication skills. Adapt fast to new work environments. High motivation and job dedication.

Part 1: Wetting at the Colloidal Scale

The first part of this Habilitation dissertation "Wetting at the colloidal scale" focuses on the statics of wetting for two particular geometries: drops/bubbles on planar solid surfaces and particles on planar fluid interfaces. Before starting this comparison in Chapter 2, the role of long range surface forces in the wetting of nano- droplets and bubbles will be reviewed in Chapter 1. Some aspects related to the contact line dynamics are also introduced (Chapter 2). Finally, experimental results on nanoparticle contact angle at the fluid interfaces measured by ellipsometry will be described in Chapter 3 and compared with the corresponding contact angles of sessile drops on planar substrates.

Chapter 1 is based on the selected publication: "The influence of long-range surface forces on the contact angle of nanometric droplets and bubbles", A Stocco*, H Möhwald, Langmuir 31 (43), 11835-11841 (2015).

Chapter 2 is based on the selected publication: "A comparison between liquid drops and solid particles in partial wetting", A Stocco*, M Nobili, Advances in Colloid and Interface Science, 247C, 223-233 (2017)

Chapter 3 is based on the selected publication: "In situ assessment of the contact angles of nanoparticles adsorbed at fluid interfaces by multiple angle of incidence ellipsometry", A Stocco*, G Su, M Nobili, M In, D Wang, Soft Matter 10 (36), 6999-7007 (2014).

Chapter 1

On the Contact Angle of Nano- Droplets and Bubbles

1.1 Introduction

Wetting at the nanoscale is a most relevant field of fundamental research and applications. Nanobubbles play key roles for the control of interfacial friction and for the propulsion mechanism of some artificial microswimmers.[1,2] Nanosized liquid drops are also important in microelectronics, microfluidics and are relevant for biomedical coatings and textile processes.[3]

At length scales between a nanometer and a micron, long-range surface forces play a key role for the equilibrium states of a given multiphase system. Such forces include long range Van der Waals, electrostatic, hydrophobic and hydration interactions.[4,5,6]

If the system under consideration is composed of two fluids and a solid, an equilibrium state can be described by partial wetting, where a drop or a bubble adopts a shape which minimizes the interactions at play. If the solid is a planar substrate, a drop tends to minimize its interfacial energy which leads to a spherical cap shape, if the drop dimension is smaller than few millimeters and gravity can be neglected. The spherical cap shape is found in many experiments for drops and bubbles sitting on smooth and clean substrates even when their dimensions become micrometric or even smaller.[7,8,9,10] In any case, for millimetric, micrometric or submicrometric drops, the interfacial profile deviates from the spherical cap shape close to the triple line at the nanoscale. This is expected since capillarity competes with long-range surface forces, which eventually dominate for distances close to few nanometers.[11] This deviation of the profile may be neglected for macroscopic bubbles or drops, since it represents only a negligible part of the profile. However, this is not the case for nanometric drops and bubbles, for which long-range surface forces play a central role in the statics and dynamics of wetting.

Some recent investigations have been focused on the formation and stability of nanobubbles, which are observed mostly on hydrophobic surfaces immersed in a liquid. Nanobubbles possess heights lower than 10-100 nm and in many experiments they are found to be very stable.[2,9,10,12,13] This long time stability is somewhat surprising and many theoretical models attempted to quantify the experimental observations. Recently, an explanation based on contact line pinning and gas oversaturation of the liquid, which balance the gas diffusion driven by the Laplace pressure, has been proposed.[14,15] Line tension, collective diffusion effects have been also discussed in the literature to explain some aspects of the stability and the contact angle of nanobubbles.[2,16,17] One remarkable feature is also represented by the difference in contact angle between those nanobubbles and the corresponding macroscopic air bubbles. However, some questions such as the value of the capillary pressure inside the nanobubbles and the role of surface forces on the contact angle remain open,[2,10,16,18] and the desirable control on the formation and stability of nanobubbles is not yet fully achieved, which represents a major drawback for applications.

Many issues related to the physics of surface nanobubbles are common to the physics of surface nanodrops.[14] Also for nano-sized drops, line tension is usually invoked to describe the contact angle of droplets of decreasing sizes. In many experiments the droplet height can be as small as few nanometers. Negative values of the line tension have been found in most of the experiments.[6,7,16] Negative line tension values would imply that drops are not stable, since the increase of the contact line perimeter results in a decrease of the total energy of the system. This is in contrast to the experimental observations which attest a long time stability of those nanodrops.

In this chapter, we recall the importance of long-range surface forces (which are usually neglected in the recent literature) on the shape of nanometric droplets and bubbles. The focus is on Van der Waals interactions and on the interfacial profiles and contact angles of nanometric drops and bubbles. We expect that the long range nature of the forces affects the domain shape especially near the triple line and consider this in a quantitative way.

1.2 Brief review on wetting statics

1.2.1 Spreading coefficients

A droplet or a gas bubble inside a macroscopic immiscible fluid assumes a spherical shape to minimize its surface free energy. The spherical shape of drops and bubbles could change if a planar interface is present in the system.

Dealing with pure fluids and droplet/bubble, the surface free energy is proportional to the interfacial tensions γ_i (for liquids) and σ_i (for solids), which are the derivatives of the free energy with respect to the area (at constant temperature T, total volume V and number of molecules n), γ_i and $\sigma_i = \left(\frac{dE}{dA_i}\right)_{T,V,n}$.[20] In a gas G atmosphere, for liquid L droplets in contact with a solid S surface, from the interfacial tensions between the media, a dry or initial spreading coefficient S_0, defined as:

$$S_0 = \sigma_{SG} - \sigma_{SL} - \gamma, \tag{1.1}$$

describes the tendency of the liquid to spread on the planar surface. For solid surfaces, $S_0 > 0$ implies complete wetting or spreading of the droplet that tends to form a thin film on the surface. $-2\gamma < S_0 < 0$ represents the partial wetting case with the drop adopting a contact angle:

$$\cos\alpha = 1 + S_0/\gamma. \tag{1.2}$$

$S_0 = 0$ and $S_0 = -2\gamma$ represent the limiting cases of spreading ($\alpha = 0$) and drying ($\alpha = 180°$) states respectively, see Figure 1.1.

1.2.2 Long range surface forces: Van der Waals forces and electrostatics

Van der Waals forces account for dispersion forces, London forces, electrodynamic forces and induce-dipole/induce dipoles forces. Here we consider only non-retarded long range Van der Waals forces. Attractive and repulsive Van der Waals interactions can be found as a function of the dielectric properties ε_i and refractive indexes n_i of the media under investigation.

Hamaker constants calculated on the basis of the Lifshitz theory were reported by Israelachvili for two media 1 and 2 interacting across a medium 3:[5]

$$A_H = A_{H,0} + A_{H,\upsilon} \tag{1.3}$$

$$A_{H,0} = \frac{3}{4} k_B T \left(\frac{\varepsilon_1 - \varepsilon_3}{\varepsilon_1 + \varepsilon_3}\right)\left(\frac{\varepsilon_2 - \varepsilon_3}{\varepsilon_2 + \varepsilon_3}\right)$$

$$A_{H,\upsilon} = \frac{3h_P\nu_e}{8\sqrt{2}} \frac{(n_1^2 - n_3^2)(n_2^2 - n_3^2)}{(n_1^2+n_3^2)^{0.5}(n_2^2+n_3^2)^{0.5}\left[(n_1^2+n_3^2)^{0.5}+(n_2^2+n_3^2)^{0.5}\right]},$$

where k_B is the Boltzmann constant, h_P is the Planck constant ($6.626\ 10^{-34}$ J.s) and ν_e is the main electronic absorption frequency ($\approx 3\ 10^{15}\ s^{-1}$).

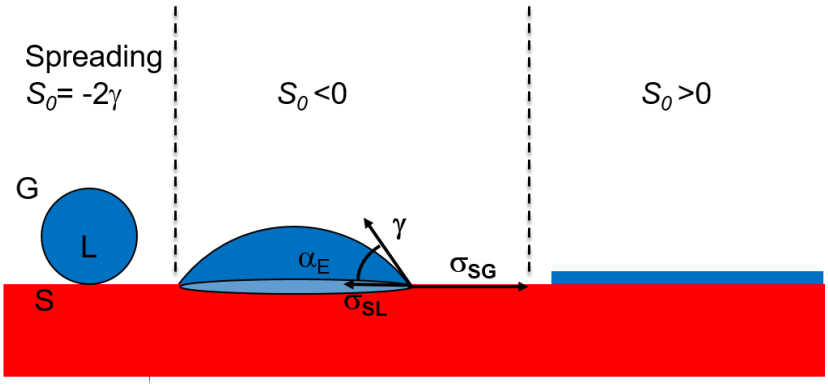

Figure 1.1 Sketches of liquid L drops at a solid S interface. Equilibrium of interfacial tensions is sketched in partial wetting at the solid interface ($S_0 < 0$). $S_0 > 0$ corresponds to total wetting or spreading. G = gas, S = solid, L = liquid.

Attractive interactions are usually found for symmetric (or similar) systems such as in freely suspended liquid films (air-liquid-air interfaces) which tend to shrink and disappear under the effect of attractive Van der Waals forces. Repulsive interactions are usually (but not always observed for non-symmetric system) such as solid-liquid-gas or water-oil-air interfaces. The latter system indeed show repulsive Van der Waals interactions for alkane (i.e. oil) films with higher carbon chain numbers (e.g. dodecane) between air and water, but it vanishes for low number alkanes (e.g. pentane).[21]

Free energy per unit area between two planar surfaces spaced by a distance h due to Van der Waals long range force is:

$$V_{VdW} = -\frac{A_H}{12\pi h^2}\,. \tag{1.4}$$

Positive Hamaker constants correspond to attractive interactions between the surfaces; whilst negative constants correspond to repulsive interactions.

If water is the medium across which the two interface interact, electrostatic double layer interactions are also relevant and a characteristic length scale to be considered is the Debye screening length. Free energy per unit area for two planar surfaces immersed in a 1:1 electrolyte solution in the weak overlap approximation reads:

$$V_{EDL} = \frac{64 k_B T c_{ion,bulk}}{\kappa}\left(\tanh\frac{e\psi_0}{4k_BT}\right)^2 \exp(-\kappa h), \tag{1.5}$$

where $c_{ion,bulk}$ is the ion concentration in the bulk, e is the elementary charge, ψ_0 is the surface potential and $1/\kappa$ is the Debye length, which follows:

$$\kappa^2 = \sum_i \frac{c_i e^2}{\varepsilon\varepsilon_0 k_B T} \tag{1.6}$$

Note that $1/\kappa$ could varies from about 1 µm in pure water at pH = 7 to 0.3 nm in 1 M NaCl solution.

1.2.3. Wetting regimes and films

Considering a liquid (L) film of thickness h between a gas and a solid media, we can define an energy (per unit area) $P(h)$ which accounts for long range surface forces. For large h (> 1 µm) these forces are negligible and $P(+\infty) = 0$, whilst for $h = 0$, $P(0) = S = \sigma_{SG} - (\sigma_{SL} + \gamma)$ if the total energy E (per unit area) is written in the form:

$$E(h) = \sigma_{SL} + \gamma + P(h)\,. \tag{1.7}$$

From $P(h)$ one defines a disjoining pressure as:

$$\Pi(h) = -\frac{dP}{dh}. \tag{1.8}$$

Hence for attractive (repulsive) long range interactions the disjoining pressure Π is negative (positive). In the case of VdW interactions, $P(h) = V_{VdW}$ and $\Pi(h) = -\frac{A_H}{6\pi h^3}$. For repulsive interactions the interfaces L/G and L/S are pushed apart from each other, while the opposite occurs for attractive interactions.

1.2.4. Contact angle

The equilibrium contact angle of a sessile drop on a solid substrate in partial wetting is defined in the far-field, where the minimum energetic state leads to a spherical cap profile of the drop. Zooming on the triple line region where the three phases meet, one finds that the droplet profile deviates from a spherical cap due to long-range surface forces originating from the physicochemical properties of the media, see Fig. 1.2.

Despite the fact that the local contact angle α_L in the colloidal region of a drop is different from a macroscopic contact angle, an equilibrium contact angle α_E can be always defined by considering that in the far field any local change (down to the molecular scale) will not affect the calculation of a free energy balance, if the triple line is simply shifted by an infinitesimal distance.[11] The equilibrium of interfacial energies for a solid (S)-gas (G)- liquid (L) system can be expressed in terms of the work associated with an incremental area change ldx (where l is the line)on the solid substrate, see Fig. 1.2:[11]

$$W_{\text{II-I}} = \sigma_{SG}\, l\mathrm{d}x - \sigma_{SL}\, l\mathrm{d}x - \gamma\, l\mathrm{d}x \cos\alpha_E = 0, \tag{1.9}$$

where σ_{SG}, σ_{SL} and γ are the solid-gas, solid-liquid and liquid-vapour interfacial tensions, respectively. In Eq. 1.9 it is also assumed that local contact angles in the colloidal region simply translate when shifted by dx. Note that we define $x = 0$ at the place where the spherical cap profile touches the solid substrate. The Young equation is obtained from eq. 1.9 :

$$\cos\alpha_E = (\sigma_{SG} - \sigma_{SL}) / \gamma. \tag{1.10}$$

Hence, it is possible to describe an equilibrium contact angle in the far-field, being aware that in the colloidal region the local profile may be very different from the far field profile, i.e. for lengths < 1 µm. The latter distance describes the limit, for which long-range surface forces become significant (see section 1.2.2).

Different theoretical approaches aimed at describing the interface profile at small scales.[22] Long-range surface forces, line tension and contact angle hysteresis have been discussed for the interface profile of macroscopic drops.[22,23]

1.2.5. Line tension

Considering that in partial wetting three bulk phases form three interfaces and a common contact line, a thermodynamic equilibrium can be described in the far field accounting both for three interfacial tension and a line tension terms. The latter is associated to the energy contribution of the triple line. Line tension k is defined as the energy per unit contact line length and represents the leading term of the total energy of the system after subtracting volume and interface contributions [24]. Hence, the line tension is the derivative of the free energy with respect to the contact line l (at constant temperature T, total volume V, area, and number of molecules n), $k = \left(\frac{dE}{dl}\right)_{T,V,A,n}$.[25]

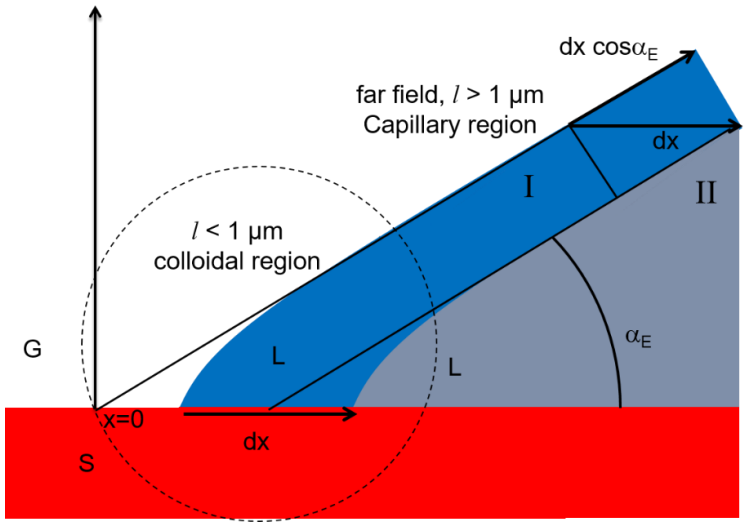

Figure 1.2 Sketch of a droplet profile in the colloidal region for characteristic length scales lower than a micrometer and in the far field region. Upon a shift dx of the triple line, one can always define an equilibrium contact angle accounting only for interfacial energy contributions. $x = 0$ at the place where the spherical cap profile touches the solid substrate. G = gas, S = solid, L = liquid.

Two different sources of excess energy are related to the line tension. On a molecular level, the intermolecular interactions between two media will be affected by the presence of the third one on the triple line, leading to an unsaturation of interactions.[25] The second source of excess energy is related to the interface profile disturbed by long-range surface forces which tend to bend a spherical cap profile in order to minimize the local energy of the system.[25]

However, it is non trivial to calculate and measure the line tension according to the previous definition. One way to evaluate the line tension contribution is to find the microscopic profile of a partially wetting drop and consider the energy associated with the deviation between the microscopic profile and the macroscopic spherical cap profile.[24] Within this approach, the line tension is a constant calculated by the effective interfacial potential for the solid liquid vapour system accounting for three terms: (i) the asymptote of the profile at the contact line (ii), the whole interfacial profile and the corresponding local effective interface potential, (iii) and the interactions between fluid molecules.[24] From these calculations one finds the theoretical line tension for a given system which can be compared to the experimental line tension measured from contact angle experiments performed on droplets or bubbles of different sizes.[7,18,26] Note that in this description the drop dimension is macroscopic, but only the microscopic profile (for characteristic length scale smaller than a micrometer) is relevant for the line tension calculation.[26]

The line tension has also an effect on the equilibrium contact angle. This is apparently in contrast with the definition of the equilibrium contact angle described in the previous section where an equilibrium contact angle can be always defined in the far field (see Fig. 1.2).

A reconciliation between these descriptions could be done accounting for a change of the local interfacial profile upon an infinitesimal translation and introducing a line energy contribution kdl in Eq. 1.9:[25]

$$\sigma_{SG}\, l\mathrm{d}x - \sigma_{SL}\, l\mathrm{d}x - \gamma\, l\mathrm{d}x \cos\mathcal{A}_{eq} - k\mathrm{d}l = 0\,, \qquad (1.11)$$

where $\mathcal{A}_{eq}$ is the equilibrium contact angle accounting for the line tension k. However, it is worth noting that even if the interfacial profile simply translates (Fig. 1.2), one could always write equation 1.11 and associate the line energy term to a cohesive excess energy of the three phase system analogously as one considers the interfacial tension for a two phase system.

From equation 1.11, a far field equilibrium contact angle accounting for a line tension term could be written as:

$$\cos\mathcal{A}_{eq} = \cos\alpha_E - \frac{k}{\gamma}\frac{dl}{ldx}. \quad (1.12)$$

Note that in the partial wetting of a sessile drop, $dl = 2\pi(R_d+dx) - 2\pi R_d = 2\pi dx$ (where R_d is the droplet base radius R_d) and $dl/(ldx) = 1/R_d$ is the curvature of the contact line. Hence Eq. 1.12 becomes:[25]

$$\cos\mathcal{A}_{eq} = \cos\alpha_E - \frac{k}{\gamma R_d} \quad (1.13)$$

The modified Young equation describes as well a far field balance of surface forces where an additional term, the line tension, is introduced. Note that $\mathcal{A}_{eq}$ depends on the droplet size R_d. From eq. 1.13, the linear dependence of the cosine of the contact angle on the inverse of the droplet size was used to calculate the line tension. Within the resolution of the experiments the drop/bubble shapes were found always spherical cap like even for drops/bubbles of nanometric sizes. Analysis of the experimental data was carried out within the modified Young equation and in most of the cases a linear fit of the cosine of the contact angle versus the inverse of the drop size was imposed to evaluate the line tension.[7,8,18]

Note however the way equation 1.10 and 1.13 are derived implies that drop or bubble dimensions extend to the far field.

1.3 Open problem and interfacial profiles

1.3.1 Open problem

Now we ask the following questions: Can we predict the interfacial profile when the drop/bubble dimensions extend only in the colloidal region (i.e. dimensions smaller than a micrometer)? Can the spherical cap profile of submicrometric drops/bubbles be set by the far field equilibrium contact angle accounting or not for a line tension? What is the role of the local contact angle defined in the colloidal region?

We show in Fig. 1.3 that for a 2 μm radius droplet, the spherical cap profile merges a local interfacial profile for a distance of the order of 0.1 μm (5 % of the radius). Hence, the droplet will adopt a spherical cap profile defined by a far field contact angle and only in the colloidal region (well below a distance of 0.1 μm), the interfacial profile will deviate because of a competition between the long-range surface and capillary forces, i.e. for radial distances < 100 nm. Keeping constant the contact angle (α_E = 0.1 rad), we plot spherical cap profiles for submicron sized droplets. Comparison with a calculated local interfacial profile (as described in the following section) reveals that cap profiles cross the local profile for distances of the order of 40 nm, which is almost of the same order as the droplet contact radius. Now it becomes problematic to imagine a matching between a local profile and a spherical cap profile, as the slopes of the two profiles are very different at the crossing points. Moreover, if one would predict that the contact angle of submicron sized droplets can be described by the modified Young equation, it is interesting to notice that the calculation of the line tension may become length scale dependent. In fact, for large drops the line tension is calculated from the deviation of the spherical cap profile due to long-range surface forces, which does not change for a drop radius larger than a micron. On the other hand for submicron sized drops the spherical cap profile is strongly affected by the long-range surface interactions and the deviation of the local profile may be due to short-range molecular forces. Indeed, a dependence of the line tension on the wetting perimeter was already described by Churaev et al..[27]

1.3.2. Interfacial profiles

Here we focus our description of interfacial profiles for length scales larger than a nanometer and smaller than a micrometer, on cases where the interfacial tensions are not length scale dependent and where short-range molecular forces can be neglected.

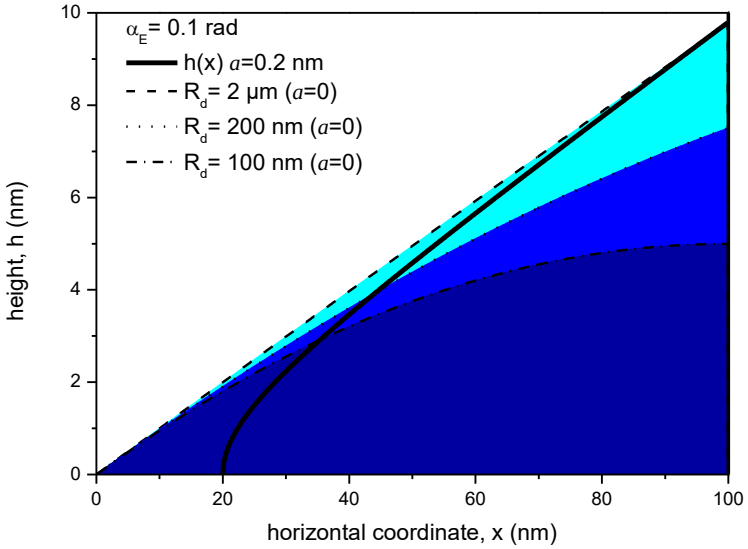

Figure 1.3 Solid line is an interfacial profile accounting for an attractive VdW force (a=0.2 nm, α_E= 0.1 rad, see the text). Three spherical cap profiles for three decreasing droplet radii with α_E= 0.1 rad are also shown. At x=0, h=0 for spherical cap profiles (for null VdW forces, a=0).

The profile of the interface can be calculated by assuming that at equilibrium the chemical potential should be equal along the interface profile. The following equation defines the equilibrium state of a liquid layer of height h :[27]

$$\gamma \Sigma + \Pi(h) = P_0 \,. \tag{1.14}$$

Where γ is the surface tension of the liquid, Σ is the local interface curvature, $\Pi(h)$ is the Derjaguin disjoining pressure and the constant P_0 is the capillary pressure of the meniscus. Note that, given the length scale of interest, gravity is neglected here. In the following we consider the case of nanodroplets, the case of nanobubbles being analogous.

In the colloidal region, the interfacial profile of a droplet can show both positive and negative curvatures, since the Derjaguin disjoining pressure could show a maximum in the range from 1 nm to 1 μm. In fact the interaction between the solid-fluid and fluid-fluid interfaces can be repulsive and attractive depending on the interactions and distance.[28]

Interfacial profiles of droplets accounting for attractive and repulsive VdW forces were calculated and analytical expressions are reported in literature.[29,30,31]

Considering only the effect of VdW forces, the curvature of the interfacial profile is negative for attractive VdW and positive for repulsive VdW forces (see Fig. 1.4). Note that the sign of the curvature depends on the sign of the second derivative of $h(x)$. Those profiles should be found in every drop and bubble. However, it is very challenging from an experimental view point to measure those profiles without introducing any artifacts.

In Figure 1.4 we show the spherical cap profile for α_E = 0.1 rad and R_d = 10 μm together with calculated profiles for attractive VdW interactions. For the spherical cap profile, when zooming into the nm length scale, the drop shape looks as a straight line of $\tan\alpha_E$ slope. Accounting for long-range attractive VdW forces in equation 1.14, the drop profile $h(x)$ becomes hyperbolic: [29]

$$Z^2 = -1 + X^2, \text{ where} \tag{1.15}$$
$$h = \frac{a}{\alpha_E} Z \,, x = \frac{a}{\alpha_E^2} X, \text{ and } a^2 = \frac{A_H}{6\pi\gamma}$$

a is a characteristic length describing the balance between VdW and interfacial tension terms, A_H is the attractive Hamaker constant and γ is the fluid interfacial tension. Note that equation 1.15 contains two free parameters, a that describes the strength of the VdW force, and α_E, which describes the far-field equilibrium.

The three profiles in Fig. 1.4 are plotted for typical values of a = 0.1, 0.2 and 0.3 nm (for a typical value of the Hamaker constant A_H =1×10^{-20} J).[32] The deviation of the profile increases, if the characteristic length a increases.

Note that the deviation of the profile is significant for heights lower than a/α_E, i.e. 1, 2 and 3 nm. Hence, as we discussed in Fig. 1.3, the hyperbolic profile will match the spherical cap profile for heights of the order of a/α_E , as one can expect for droplets of micron size or larger. Note that this will be not the case for nanodrops or nanobubbles. In fact for the latter systems the maximum height could be of the same order or even smaller than a/α_E.

We have also calculated interfacial profiles for repulsive Van der Waals forces (Fig. 1.4(B)). In this case the square of the slope of the profile is given by:[31]

$$\left(\frac{dZ}{dX}\right)^2 = [(1-2b)^{-1} + (2bZ^2)^{-1}] - 1, \qquad (1.16)$$

where $h = \delta_0 Z$, $x - x_0 = \delta_0 X$.

Here δ_0 is a distance defined by: $\delta_0^2 = -\frac{bA_H}{6\pi\gamma}$,($A_H$ is negative), and b is related to the equilibrium contact angle by: $\cos\alpha_E = 1 - 1/(2b)$. x_0 is a constant, which depends on the boundary condition of the profile.

Profiles are calculated subtracting a baseline of height δ_0, which corresponds to the height of the molecular wetting film coexisting with the meniscus. To calculate the profiles in Fig 1.4(B), Eq. 1.16 was solved numerically and in a good approximation can be represented by the analytical function:

$$Z = \tan\alpha_E \left(X - \sqrt{2b}\arctan\left(\frac{X}{\sqrt{2b}}\right)\right). \qquad (1.17)$$

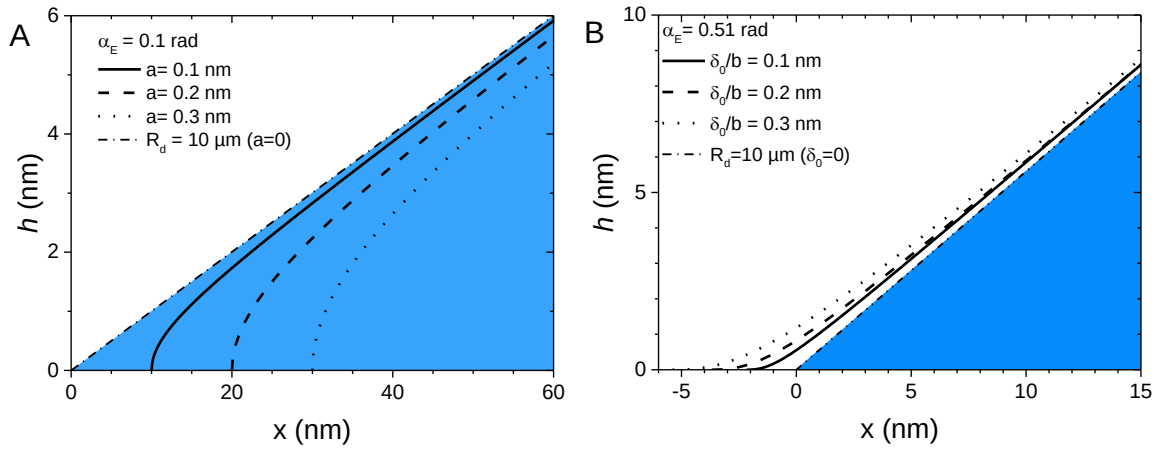

Figure 1.4 (A) Calculated interfacial profile accounting for attractive VdW forces with three characteristic lengths a = 0.1, 0.2, 0.3 nm and a spherical cap droplet profiles of 10 μm contact radius. (B) Calculated interfacial profile accounting for repulsive VdW forces with three characteristic lengths δ_0/b = 0.1, 0.2, 0.3 nm and a spherical cap droplet profiles of 10 μm contact radius. At x=0, h=0 for spherical cap profiles (for null VdW forces, a=0).

In Fig. 1.4(B) we show the interfacial profiles for three typical values of δ_0 together with a spherical cap profile for α_E = 0.51 rad and R_d = 10 μm. As we pointed out, it must be noted that the

height of nanodroplets and nanobubbles corresponds to a length, where the interfacial profile is strongly affected by VdW forces. The nanometric droplet or bubble actually exists only in the colloidal region (see Fig. 1.2), where equation 1.2 and 1.5 can not be strictly applied. Hence, it can be argued that if a droplet exists only in the colloidal region and it adopts a spherical-like cap profile, it does not imply that it will adopt the same contact angle as the one defined in the far field, where only capillarity matters.

Here we suggest that the contact angle adopted by the droplet is closely related to the local angle of the interfacial profile, which describes the competition between long-range surface and capillary forces.

A simple calculation is useful to compare the latter competition. Accounting for a disjoining pressure only due to VdW forces of the form: $\Pi(h) = -A_H/(6\pi h^3)$ one might estimate the contribution of long-range surface and capillary forces on the interfacial profile.[5] Neglecting the gravity term, the droplet profile obeys to equation 1.14:[33] $\Sigma + \Pi(h)/\gamma = P_0/\gamma = C_0$. To find the constant C_0 it is convenient to look at the drop maximum, where the first derivative of the profile is zero. When the drop maximum height is larger than 0.1 μm, the disjoining pressure decays almost to zero, $\Pi(h_{MAX}) = 0.2$ J/m$^3 \approx 0$, and $A_H/(6\pi\gamma h_{MAX}^3) \approx 1/(0.3$ m), and $C_0 = P_0/\gamma \approx 1/R_0$ is the curvature of the drop at the maximum height, i.e. assuming a spherical cap shape and $\alpha_L = 0.1$ rad, $1/R_0 = 1/(20\ \mu\text{m}) > A_H/(6\pi\gamma h_{MAX}^3)$ (see Fig. 1.5).

For small droplets the disjoining pressure does not decay close to zero anymore and:

$$C_0 = P_0/\gamma = 1/R_0 + A_H/(6\pi\gamma h_{MAX}^3). \quad (1.18)$$

When $h = 1$ nm, $A_H/(6\pi\gamma h_{MAX}^3) \approx 1/(30$ nm) showing that the contribution of the long-range surface force becomes as important as the capillary one for nanodrops and nanobubbles, i.e. assuming a spherical cap shape and $\alpha_L = 0.1$ rad, $1/R_0 = 1/(200$ nm) $< A_H/(6\pi\gamma h_{MAX}^3)$ (see Fig. 1.5).

1.4 Results and discussion

Here, we propose a simple criterion which states that a droplet, whose dimensions are in the colloidal domain, will adopt a spherical cap profile to minimize its area with a contact angle dictated by the local contact angle which accounts for both long-range surface forces and capillarity.

Hence according to this criterion, the contact angle of a nano-sized droplet of height h_{MAX} is equal to the local contact angle of the interfacial profile at the same height (Fig. 1.5(A)). The nano-sized droplet and the interfacial profile share the same contact in x, and the droplet contact radius is (see Fig. 1.5(B)): $R_d = h_{MAX} \sin\alpha_L/(1-\cos\alpha_L)$.

In Fig. 1.5(A), two droplets of different heights are shown. Using this criterion, significant differences in contact angles can be observed for droplet radii R_d smaller than 100 nm. Increasing the droplet height, the slope of the interfacial profile varies slowly and approaches the far-field value $\tan\alpha_E$.

Using the same criterion represented in Fig. 1.5, in Fig. 1.6(A) and 1.6(C) we plot the local contact angle α_L as a function of $R_d = h_{MAX} \sin\alpha_L/(1-\cos\alpha_L)$ for the calculated profiles shown in Fig. 1.4. Note that for droplet radius of 50 nm the local contact angle approaches the equilibrium contact angle, while local contact angles dramatically change around droplet radii of about 10 nm.

At this point we would like to compare our calculated data shown in Fig. 1.6(A) and 1.6(C) with the modified Young equation (equation 1.13), and the linear relation of the cosine of the contact angle with the inverse of the droplet radius.

Note that our calculations accounted only for repulsive and attractive VdW forces in the interfacial profile of drops in the mean field. The shapes of the interfacial profiles were calculated using equation 1.15 and 1.16. Equation 1.13 instead assumes that the interfacial profile could be described simply by a constant value line tension defined for macroscopic systems. Hence the underlying physics of our result and the line tension approach are completely different, and we argue, that interpreting the size-dependence of the contact angle in terms of a constant value line tension is not correct.

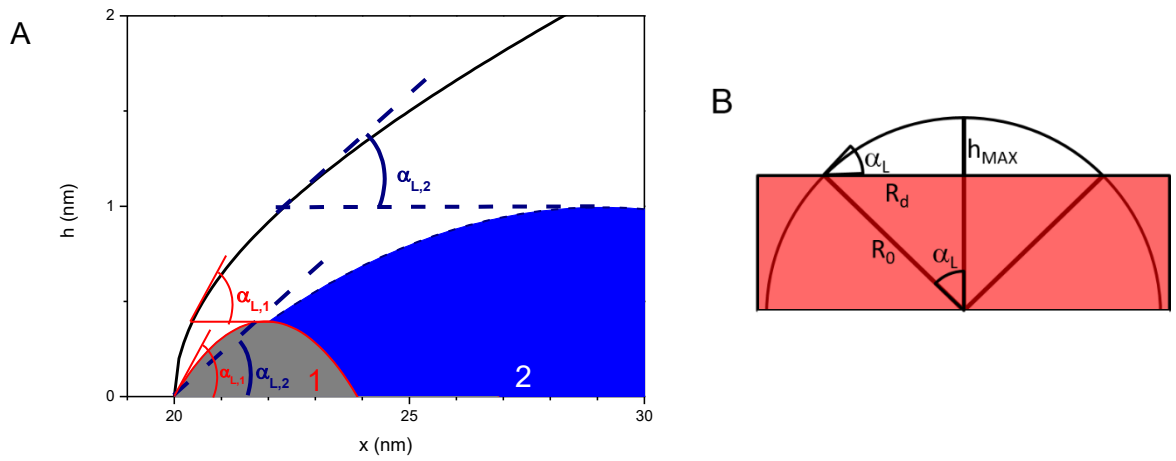

Figure 1.5 (A) Criterion for the definition of the contact angle for two nanometric droplets. The height of the droplet defines the contact angle in the interfacial profile calculated accounting for VdW forces. The droplet and the interfacial profile share the same contact at $h = 0$ (here at x=20 nm). (B) Sketch of the contact radius R_d, radius of curvature R_0 and maximum height of a spherical cap shape drop or bubble.

Just for the sake of comparison, in Fig. 1.6(B) and 1.6(D) we replotted the data shown in Fig. 1.6(A) and 1.6(C) as for line tension measurements (equation 1.13). For attractive VdW forces, a linear trend of $\cos\alpha_L$ with the drop curvature can be observed. From these slopes one would find positive line tensions $k = 6.5 \times 10^{-12}$ N ($a = 0.1$ nm), 1.2×10^{-11} N ($a = 0.2$ nm), 1.7×10^{-11} N ($a = 0.3$ nm) assuming an interfacial tension $\gamma = 72$ mN/m. For repulsive VdW forces, the trend of $\cos\alpha_L$ with the drop curvature is not linear. Actually, these curves recall the shape of experimental curves reported by Berg *et al* and Checco *et al.*.[7,8] The apparent slopes found fitting the data for repulsive VdW forces correspond to negative line tensions $k \approx -6 \times 10^{-12}$ N ($\delta_0/b = 0.1$ nm), -9×10^{-12} N ($\delta_0/b = 0.2$ nm), -1.4×10^{-11} N ($\delta_0/b = 0.3$ nm), assuming an interfacial tension $\gamma = 72$ mN/m.

Those line tension values would agree with reported theoretical and experimental values.[26] Here, negative line tensions correspond to the case of repulsive VdW forces, whereas positive line tensions correspond to attractive VdW forces. In the next section, we show a comparison of our model with nanobubble and nanodroplet experiments.

As shown in Fig. 1.6(D) and in some experiments, the cosine of the droplet contact angle is not linear with the inverse of the droplet radius if the droplet size is nanometric.[7,8] The linear relation could be found only for the modified Young equation if drops exist in the far-field. In this case the line tension k can be also calculated theoretically. k is a constant of the system, which represents the energy not accounted for in the bulk and surface terms, when far-field asymptotes can be defined.

For nanometric droplets we can relate the contact angle to the local interfacial profile, which represents the competition of forces acting at the colloidal length scale. Thus, the relation between the droplet contact angle and the droplet size is dictated by the shape of the interfacial profile in the colloidal region. Hence in general, the cosine of the contact angle is not expected to be linear with the droplet curvature, since the form of the disjoining pressure may show local minima and maxima with the distance, and both positive and negative curvatures could be observed (see Figure 1.7).[27]

Here we suggest an interpretation of experiments performed on droplets and bubbles of decreasing sizes (down to the nanometer scale) as an effect of local contact angle due to long-range surface forces such as long range VdW forces.

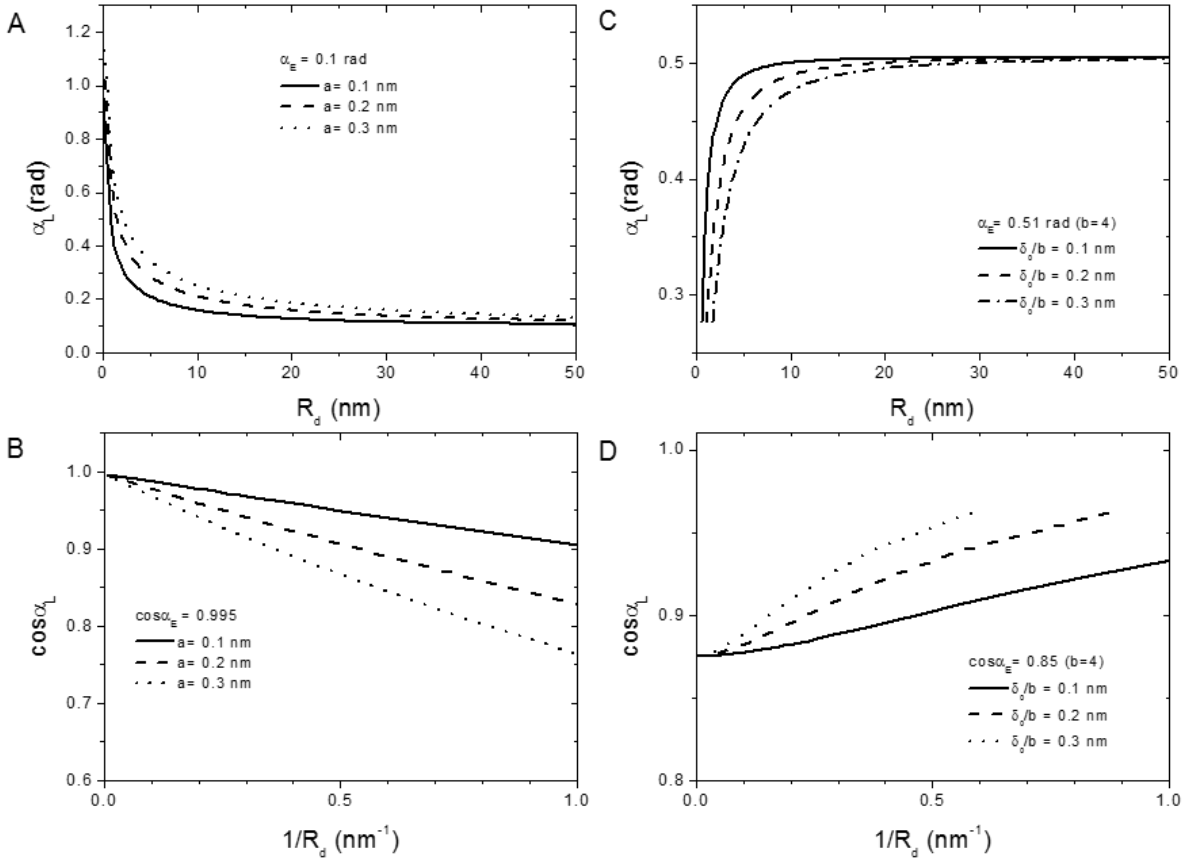

Figure 1.6 Local contact angles calculated for attractive (A) and repulsive (C) VdW forces as a function of a droplet contact radius defined as $R_d = h_{MAX} \sin\alpha_L / (1-\cos\alpha_L)$. Cosine of local contact angles calculated for attractive (B) and repulsive (D) VdW forces as a function of the inverse of R_d.

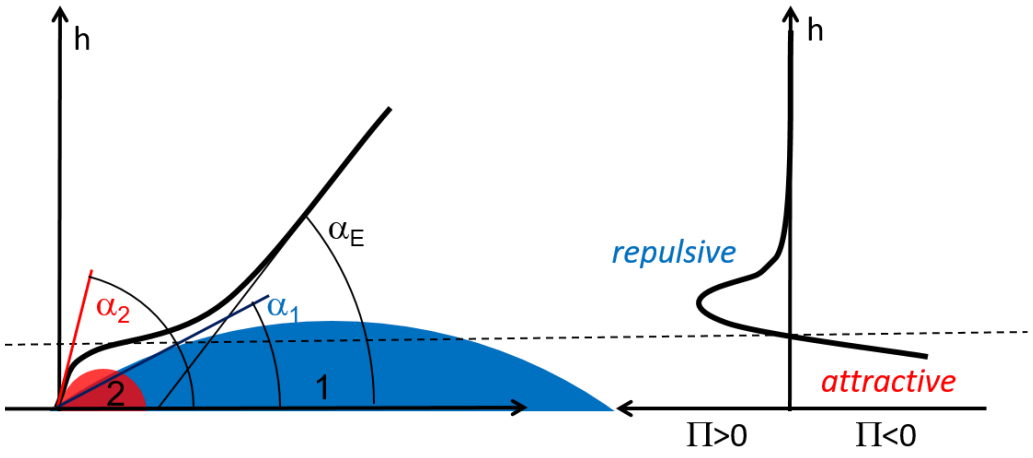

Figure 1.7 Sketch of an interfacial profile defying the contact angle of two nanodroplets or nanobubbles: 1 (in blue) and 2 (in red), according to the criterion shown in Fig. 1.4 and the connection with the profile of the disjoining pressure $\Pi(h)$.

1.5 Comparison between the model and experiments

Here, we compare the results of our model with experimental results obtained for nanobubbles and nanodroplets. Note that our model is based only on VdW forces; and attractive hydrophobic, repulsive electrostatic and repulsive hydration interactions are not yet included in the expression of the disjoining pressure. For this reason, the following comparison should be not considered a fit of the experimental results.

In Fig. 1.8 we compare our results for attractive VdW forces with experimental data obtained by Kameda et al. for nanobubbles.[18]

Note that at short distances (large values of $1/R_d$), experimental data follow the same trend of our model for attractive VdW forces. Note that the Hamaker constant are attractive in this system since a gas phase is sandwiched in between a solid and a liquid.[34] At large distances (small values of $1/R_d$), experimental data are consistent with repulsive interactions, which can be due to electrostatics.[35]

In Fig. 1.9 we compare our calculated results with the experimental results obtained by Berg et al.[7] for fullerene drops on silica substrates. Experimental data follow the same trend of our model for repulsive interactions. Compared with our model for repulsive VdW forces, an Hamaker constant corresponding to δ_0/b=1.5 nm would agree with the experimental data. However for δ_0/b=1.5 nm, $A_H = -3\times10^{-18}$ J is much larger than typical A_H values for these interfaces.[5,36] As in the previous comparison, we recall that including other long-range surface interactions (as electrostatic interactions) in the analysis may lead to an agreement between the model and the experiments. Other effects that may affect the experimental results reported in literature are connected to the contact line pinning over surface defects.

1.6 Conclusion

Finally, for large droplets (or bubbles) whose sizes are larger than a micron, the contact angle adopted in static conditions is the equilibrium contact angle α_E defined by the Young equations 1.10 and 1.13. Even for those drops, in the contact line region (at nanometric length scales) local contact angles deviate from α_E, but this is a local effect that can be considered negligible. If the droplet height is in the nanoscale the droplet profile will be strongly affected by long-range surface forces. Hence, measurements of contact angle as a function of the droplet height reveal the interaction between the solid-liquid and liquid-gas interface described in the disjoining pressure. In this context, we propose a simple criterion based on the height of the droplet to describe the change of contact angle.

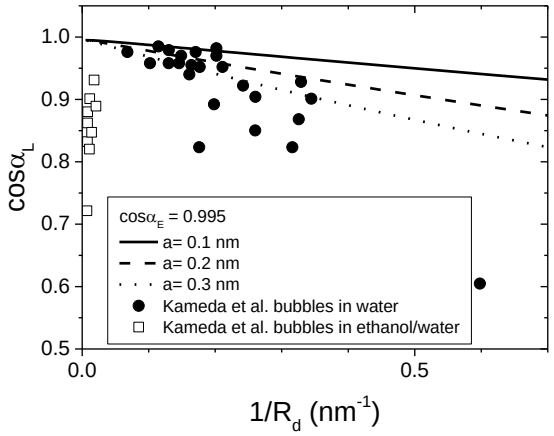

Figure 1.8 Cosine of local contact angles calculated for attractive VdW forces with three characteristic lengths a = 0.1, 0.2, 0.3 nm as a function of the inverse of R_d and experimental data on nanobubble contact angle by Kameda et al..[18]

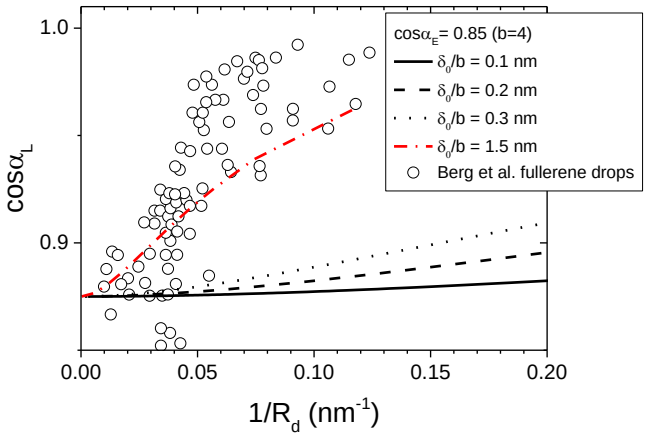

Figure 1.9 Cosine of local contact angles calculated for repulsive VdW forces with four characteristic lengths δ = 0.1, 0.2, 0.3 and 1.5 nm as a function of the inverse of R_d and experimental data on nanodrop contact angle by Berg et al..[7]

We believe that the work presented here can stimulate some new discussion in the field of nanodrops and nanobubbles. Theoretical work aiming at describing exact interfacial profiles of nanofluids accounting for different terms of disjoining pressure will surely improve the understanding of contact angle and stability results of nanobubbles and nanodrops.

To conclude, we point out two major results presented here that could be used in future studies. Eq. 1.18 shows that for nanofluids the capillary pressure depends strongly on the distance and on the Hamaker constant of the system. The latter could possess both signs, which would lead to a strong decrease or increase of the capillary pressure for nanobubbles and nanodrops. This result may help improving theoretical modeling on the gas diffusion of nanobubbles. We also suggest the stability of nanobubbles may result from the onset of a repulsive surface force, which manifest because of the negative potential of the gas-water and solid-water interfaces.[27] This repulsive force prevents the shrinking of the fluid and thus enhances the stability. A clear perspective of this work is to include the contributions of electrostatic, hydrophobic and hydration interactions (together with VdW forces) into the disjoining pressure in order to reinterpret experimental results obtained for nanodrops and nanobubbles.[14]

1.7 References

1 J. G. Gibbs and Y.-P. P. Zhao, *Appl. Phys. Lett.*, 2009, **94**, 163104.
2 V. S. J. Craig, *Soft Matter*, 2011, **7**, 40.
3 A. Méndez-Vilas, A. B. Jódar-Reyes and M. L. González-Martín, *Small*, 2009, **5**, 1366–1390.
4 E. E. Meyer, K. J. Rosenberg and J. Israelachvili, *Proc. Natl. Acad. Sci. U. S. A.*, 2006, **103**, 15739–46.
5 J. N. Israelachvili, *Intermol. Surf. Forces*, 2011, 205–222.
6 I. V. Kuchin, O. K. Matar, R. V. Craster and V. M. Starov, *Colloids Interface Sci. Commun.*, 2014, **1**, 18–22.
7 J. K. Berg, C. M. Weber and H. Riegler, *Phys. Rev. Lett.*, 2010, **105**, 76103.
8 A. Checco, P. Guenoun and J. Daillant, *Phys. Rev. Lett.*, 2003, **91**, 186101.
9 B. Zhao, Y. Song, S. Wang, B. Dai, L. Zhang, Y. Dong, J. Lü and J. Hu, *Soft Matter*, 2013, **9**, 8837.
10 B. M. Borkent, S. De Beer, F. Mugele and D. Lohse, *Langmuir*, 2010, **26**, 260–268.
11 P. G. De Gennes, *Rev. Mod. Phys.*, 1985, **57**, 827–863.
12 S. Karpitschka, E. Dietrich, J. Seddon, H. Zandvliet, D. Lohse and H. Riegler, *Phys. Rev. Lett.*,

2012, **109**, 66102.
13 X. H. Zhang, N. Maeda and V. S. J. Craig, *Langmuir*, 2006, **22**, 5025–35.
14 D. Lohse and X. Zhang, *Rev. Mod. Phys.*, 2015, **87**, 981–1035.
15 D. Lohse and X. Zhang, *Phys. Rev. E*, 2015, **91**, 31003.
16 H. Peng, G. R. Birkett and A. V. Nguyen, *Adv. Colloid Interface Sci.*, 2014, 3–10.
17 J. H. Weijs and D. Lohse, *Phys. Rev. Lett.*, 2013, **110**, 54501.
18 N. Kameda and S. Nakabayashi, *Chem. Phys. Lett.*, 2008, **461**, 122–126.
19 J. Drelich and J. Miller, *Part. Sci. Technol.*, 1982, **10**, 1–20.
20 P.-G. De Gennes, F. Brochard-Wyart and D. Quéré, *Capillarity and Wetting Phenomena*, 2004.
21 K. Ragil, J. Meunier, D. Broseta, J. Indekeu and D. Bonn, *Phys. Rev. Lett.*, 1996, **77**, 1532–1535.
22 J. H. Snoeijer and B. Andreotti, *Phys. Fluids*, 2008, **20**, 57101.
23 J. H. Snoeijer and B. Andreotti, *Annu. Rev. Fluid Mech.*, 2013, **45**, 269–292.
24 L. Schimmele, M. Naplórkowski and S. Dietrich, *J. Chem. Phys.*, 2007, **127**, 164715.
25 J. Drelich, *Colloids Surfaces A Physicochem. Eng. Asp.*, 1996, **116**, 43–54.
26 T. Pompe and S. Herminghaus, *Phys. Rev. Lett.*, 2000, **85**, 1930–1933.
27 N. Churaev, V. Starov and B. Derjaguin, *J. Colloid Interface Sci.*, 1982, **89**, 16–24.
28 I. V. Kuchin, O. K. Matar, R. V. Craster and V. M. Starov, *Colloids Interface Sci. Commun.*, 2014, **1**, 18–22.
29 P. G. De Gennes, X. Hua and P. Levinson, *J. Fluid Mech.*, 1990, **212**, 55–63.
30 P. Wayner, *J. Colloid Interface Sci.*, 1980, **77**, 495–500.
31 P. Wayner, *J. Colloid Interface Sci.*, 1982, **88**, 6–7.
32 L. Bergström, *Adv. Colloid Interface Sci.*, 1997, **70**, 125–169.
33 A. Sharma, *Langmuir*, 1993, 3580–3586.
34 J. Visser, *Adv. Colloid Interface Sci.*, 1972, **3**, 331–363.
35 M. Chaplin, *Water*, 2009, **1**, 1–28.
36 X. Ma, B. Wigington and D. Bouchard, *Langmuir*, 2010, **26**, 11886–11893.

Chapter 2

A Comparison between Liquid Drops and Solid Particles in Partial Wetting

2.1 Introduction

In the following, we compare two geometries in partial wetting: a liquid drop on a planar substrate and a spherical particle at a planar liquid interface. We show that this comparison is far from being trivial even if the same physical interactions are at play in both geometries. Similarities and differences in terms of free energies and frictions will be discussed. Contact angle hysteresis, the impact of surface roughness and line pinning on wetting will be described and compared to selected experimental findings.

Here we aim at bridging the wetting knowledge obtained for liquid drops at planar solid surface and the wetting of spherical particles at the liquid interface. We would also like also to highlight how rich the wetting of micro- and nano- particles is, and the potentials of these particles as probes in partial wetting. In fact, different length scales and interactions can be investigated and explored by tuning the size and the surface properties of particles.

2.2 Free energy landscape, force and line tension effects

2.2.1 Free energy, force and equilibrium contact angle for planar and spherical surfaces

We start by a description in an ideal world where the surfaces are perfectly smooth and defect free, see Figure 2.1. We focus on drop or particle sizes smaller than the capillary length $l_c = \sqrt{\gamma/(\rho g)} \approx$ 2 mm (where γ is the surface tension of the liquid ρ is the liquid density and g is the gravitational acceleration) but comparable or larger than a characteristic length scale of long range surface forces $l_s = \alpha_E^{-2}\sqrt{A_H/6\pi\gamma} \approx 1\ldots10$ nm (where α_E is the equilibrium contact angle, A_H is the Hamaker constant).[1] We also assume that the liquid and the solid are not volatile. In the following we will compare the behaviour of spherical solid particle of radius R and a liquid drop having the same radius, initially, when it touches the solid substrate, $R_0(\alpha=180°) = R$. Hence, the volume of the drop is kept constant for any contact angles, see Fig. 2.1. Moreover, here we neglect deformations of the planar solid and liquid interface. Under these assumptions, a spherical liquid drop touching an infinite solid substrate will search for an equilibrium contact angle, keeping the same volume but changing its shape and area. In the size range considered here, the liquid drop adopts a spherical cap profile according to the Laplace equation. A solid particle touching an infinite liquid interface will also search an equilibrium contact angle but it will keep both its volume and area constant, see Figure 2.1.

Equilibrium position of the liquid drop can be found calculating the free energy of the system as a function of the contact angle α. At the point of contact the drop radius is R_0 and the free energy is $E(\alpha=180°) = \sigma_{SG}\, A + \gamma 4\pi R_0^2$, where A is the planar surface area and σ_{SG} is the solid-gas interfacial tension (Figure 2.1).

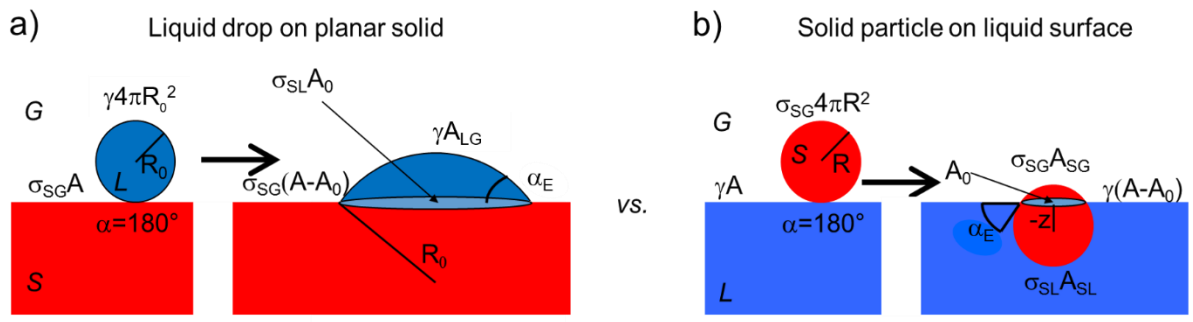

Figure 2.1 Sketch of a liquid drop on a solid substrate (a) and a solid spherical particle on a liquid interface (b) reaching an equilibrium contact angle in partial wetting from a dry state, $\alpha = 180°$. *G* = gas, *S* = solid, *L* = liquid.

At an arbitrary contact angle α, the free energy of the system is:

$$E(\alpha) = \sigma_{SG} A - \sigma_{SG} A_0 + \sigma_{SL} A_0 + \gamma A_{LG}. \quad (2.1)$$

Where σ_{SL} is the solid-liquid interfacial tension. A_0 is the area covered by the drop, $A_0 = \pi R_0(\alpha)^2 \sin^2\alpha$. A_{LG} is the liquid-gas interfacial area $A_{LG} = 2\pi R_0(\alpha)^2 (1-\cos\alpha)$ and $R_0(\alpha) = V^{\frac{1}{3}}\left[\frac{\pi}{3}(2 - 3\cos\alpha + \cos^3\alpha)\right]^{-\frac{1}{3}}$. The drop base radius is $R_d = R_0(\alpha)\sin\alpha$, see Figure 2.1(a).

The thermodynamic equilibrium contact angle can be defined at the position where $E(\alpha)$ is minimum, see Fig. 2.2. This minimum is described by the Young equation:

$$\cos\alpha_E = (\sigma_{SG} - \sigma_{SL}) / \gamma. \quad (2.2)$$

In the limit of zero contact angle, the free energy $E(\alpha)$ tends to infinity (equation 2.1). In this limit, a finite value of the energy will be set by the long-range surface force at play. The liquid may adopt the form of a film (molecular or nanometric) or liquid pancake [2].

For a spherical particle at a fluid interface the same approach can be used, see Figure 2.1(b). The calculation starts considering a colloid completely dry, which touches a free planar liquid interface. The free energy of the system (colloid plus free interface) is simply given by the product of the areas and the corresponding interfacial tensions: $E(\alpha=180°) = \gamma A + \sigma_{SG} 4\pi R^2$, where R is the radius of the spherical particle and A is the area of the free interface. When the solid particle crosses the interface, a solid-liquid interface is created, the energy of the solid-gas interface is reducing and the liquid-gas interface is missing an area A_0 due to the particle adsorption. The free energy of the system as a function of the particle position expressed as $\cos\alpha = -z/R$ is (z is the vertical distance between the center of the particle and the interface: $z > 0$ in gas).[3]

$$E(\alpha) = \gamma A + 2\pi R^2 \left[\sigma_{SG}(1-\cos\alpha) + \sigma_{SL}(1+\cos\alpha) - \frac{1}{2}\gamma\sin^2\alpha\right]. \quad (2.3)$$

Note that besides wetting no additional interactions are accounted in equation Eq. 2.3.

The thermodynamic equilibrium contact angle can be defined at the position where the $E(\alpha)$ is minimum, see Figure 2.2:

$$(\sigma_{SG} - \sigma_{SL})/\gamma = -z_0/R = \cos\alpha_E. \quad (2.4)$$

Equation 2.4 is equivalent to Equation 2.2. Equilibrium of forces acting on the contact line of a partially wetted colloid at a fluid interface or a liquid drop partially wetting a solid substrate leads always to: $\sigma_{SG} = \sigma_{SL} + \gamma\cos\alpha_E$.

If the drop or the particle is at a position α different from α_E, the system is out of equilibrium.

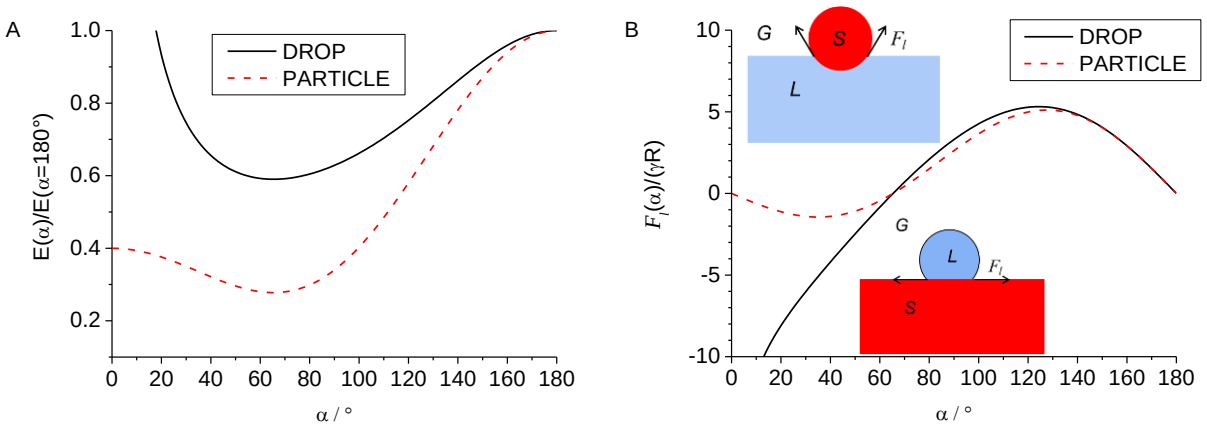

Figure 2.2 A) Free energy ratio $E(\alpha)/E(\alpha=180°)$ ($\alpha_E = 65°$ and $\gamma = 72$ mN/m, γA and $\sigma_{SG}A$ are constants of the systems and their contributions was subtracted to E) as a function of α for drop and particle geometries. B) Force F_l normalized by the constant term γR ($\alpha_E = 65°$, $\gamma = 72$ mN/m and $R = R_0(\alpha=180°)$) as a function of α for drop and particle geometries.

The imbalance due to $\alpha \neq \alpha_E$ produces a force $F_l = -\frac{dE}{ds}$, where s represents the displacement of the contact line on the solid, acting on the triple line which is proportional to the contact line length.

For a liquid drop, the displacement of the contact line is radial and parallel to the solid plane (see inset in Figure 2.2(B)). Using the convention $F_l > 0$ for $\alpha > \alpha_E$, the force acting on the line F_l is:

$$F_l(\alpha) = 2\pi R_d \gamma(\cos\alpha_E - \cos\alpha) = 2\pi R_0(\alpha)\sin\alpha\, \gamma(\cos\alpha_E - \cos\alpha). \quad (2.5)$$

For a spherical particle, the displacement of the contact line is the longitudinal coordinate $s = R\theta$ (θ is the polar angle in spherical coordinates (see inset in Figure 2.2(B)). Using the convention $F_l > 0$ for $\alpha > \alpha_E$, the force F_l acting tangential to the solid surface is:

$$F_l(\alpha) = 2\pi R \sin\alpha\, \gamma(\cos\alpha_E - \cos\alpha). \quad (2.6)$$

Given that R_0 is a function of α, for liquid drops the force F_l (equation 2.5) tends to diverge for very low contact angles, see Figure 2.2. Instead for spherical particles, the force must be zero when the length of the contact line is null: α=0 and 180°, see Figure 2.2. If we consider a drop and a process leading to the equilibrium from a very low contact angle, the force will be high at low angles ($\alpha \rightarrow 0$) and smoothly decreases when approaching α_E. Whereas for a particle, the force acting during a path from low α to $\alpha = \alpha_E$ shows a non-monotonic behavior, which is qualitatively the same behavior experienced during the path from α =180° to $\alpha = \alpha_E$ for both drop and particle. The force F_l reflects the changes of the wetted perimeter and the imbalance of the liquid-gas interfacial tension. F_l shows a maximum corresponding to the large increase of the wetted perimeter at high angles, which is then counterbalanced by the decreasing liquid-gas interfacial tension component. Finally, one could calculate the vertical force acting on a spherical particle as $F_p = -F_l(\alpha)\sin\alpha$, which shows the same qualitative behaviour as the one discussed previously (equation 2.6).

2.2.2 Line tension and length scale dependent contact angle

For a liquid drop, as we have seen before in Chapter 1 (section 1.2.5), the addition of a line tension k term in the free energy of the system leads to a modified Young equation: $\cos\mathcal{A}_{eq} = \cos\alpha_E - k/(\gamma R_d)$, where $\mathcal{A}_{eq}$ is the equilibrium contact angle accounting for line tension and $R_d = R_0\sin\mathcal{A}_{eq}$ and:

$$\cos\mathcal{A}_{eq} = \cos\alpha_E - \frac{k}{\gamma R_0}\frac{1}{\sin\mathcal{A}_{eq}}\,. \tag{2.7}$$

The previous equation can be also obtained by the derivation of the free energy of the system as we have shown in the previous section:

$$E(\alpha) = \sigma_{SG}A - \sigma_{SG}A_0 + \sigma_{SL}A_0 + \gamma A_{LG} + k2\pi R_0(\alpha)\sin\alpha\,. \tag{2.8}$$

For solid spherical particles, when the line tension k is accounted, the free energy becomes:[4]

$$E(\alpha) = \gamma A + 2\pi R^2\left[\sigma_{SG}(1-\cos\alpha) + \sigma_{SL}(1+\cos\alpha) - \frac{1}{2}\gamma\sin^2\alpha + \frac{k}{R}\sin\alpha\right]. \tag{2.9}$$

For both drops and particles, positive (negative) k means that an increase of the length of the contact line represents an energy cost (gain). For negative values of k the minimum $E(\alpha)$ becomes deeper, whereas for positive values of k the energy minimum could even disappear, see Figure 2.3. By deriving Equation 2.9 along the longitudinal coordinate, one calculates the force acting on the contact line:

$$F_l(\alpha) = 2\pi R\,\gamma\left[(\cos\alpha_E - \cos\alpha)\sin\alpha + \frac{k}{\gamma R}\cos\alpha\right]. \tag{2.10}$$

For $F_l = 0$, the equilibrium angle can be found:

$$\cos\mathcal{A}_{eq} = cos\alpha_E + \frac{k}{\gamma R}\frac{\cos\mathcal{A}_{eq}}{\sin\mathcal{A}_{eq}}\quad. \tag{2.11}$$

It is important to remark the difference between Equation 2.7 and 2.11. For the droplet geometry and positive line tension, the contact angle will always increase in order to reduce the length of the contact line and the energy cost associated (keeping the volume of the droplet constant). For a spherical particle the decrease of the length of the contact line will depend on the immersion of the particle. A particle that is mostly located in the gas phase, in order to reduce the length of the contact line, will increase its contact angle; whilst a particle that is mostly immersed in the liquid will decrease its contact angle.

In Figure 2.3 we plot the free energies for drop and particle geometries for different values of line tension with $\alpha_E = 65°$ as in Figure 2.3(a). In both geometries, negative line tensions lead to a deeper energy minimum. If the line tension value increases, one observes opposite shifts of the equilibrium contact angle $\mathcal{A}_{eq}$. Since positive line tensions represent an energy cost, energy minima could vanish and an energy maximum could appear. For the particle geometry, stable, metastable and unstable regions as a function of the strength of $k/(\gamma R)$ were described by Aveyard and Clint[4] and corrected by Drelich.[5] Note that by scrutinising equation 2.8, one would find stable, metastable and unstable regimes for droplets showing positive line tension as well. The existence of an energetic barrier against partial wetting may have serious consequences. Drop or particle with relative high line tensions may remain in a complete wetting or dry states simply due to the high energetic cost associated to the creation of the contact line.

Note that, the line tension, as it was introduced here, is not a source of contact angle hysteresis. Here we keep the line tension as a purely thermodynamic quantity. In analogy with the interfacial tension for low energy system, which is of the order of magnitude of $k_BT/l_m^2 \approx 40$ mN/m ($l_m = 0.3$ nm is a molecular length),[6] the order of magnitude of line tension can be estimated as $k_BT/\,l_m \approx 10^{-11}$ N. It is worth noting that line tension $k \approx 10^{-11}$ N…10^{-12} have been usually measured in biphasic lipid monolayers.[7,8] It is important to recall that line tension could be also tuned by molecular or polymeric species present in the contact line region, which act as line active species.[9,10]

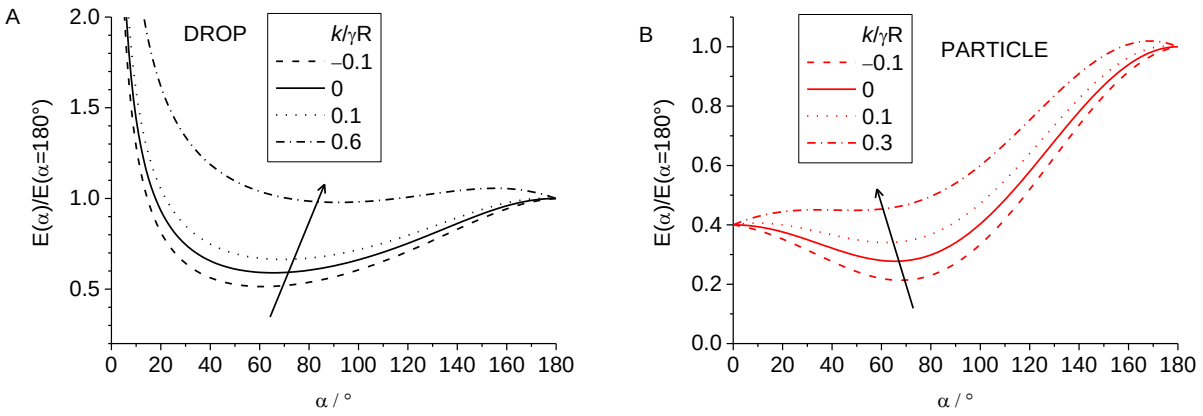

Figure 2.3 A) Free energy ratio $E(\alpha)/E(\alpha=180°)$ ($\alpha_E = 65°$ and $\gamma = 72$ mN/m, $\sigma_{SG}A$ is a constant of the system and it was subtracted to E) as a function of α for the drop geometry and different line tension values. B) Free energy ratios $E(\alpha)/E(\alpha=180°)$ ($\alpha_E = 65°$ and $\gamma = 72$ mN/m, γA is a constant of the system and it was subtracted to E) as a function of α for the particle geometry and different line tension values.

It is quite clear that the magnitude of $k/(\gamma R)$ deserves a further discussion in order to illustrate the impact of positive line tensions. Only for very small particle of 10 nm radius (and for typical values of contact angles and interfacial tensions), a line energy $k \geq 10^{-10}$ N leads to the vanishing of the energy minimum across the interface.[11]Latter values of the line tension can be regarded as the upper bound limit value of physically meaningful line tension.[12,13] Hence, the line tension effect is expected to play a dramatic role only for spherical particle radii smaller than 10 nm or for particles with high aspect ratios.[11] This result may be of great importance for the mass transfer of nanoparticles across a fluid interface in liquid-liquid extraction. As for droplets or bubbles in the submicron scale,[14] also for particles some experimental results show indeed that the equilibrium contact angle changes with the size. Experiments on silica particles of radii between 70 and 500 nm showed systematic change of the contact angle at the liquid polystyrene-air interface.[15] Line tension $k \approx 10^{-9}$ N has been reported, which is somewhat higher than the theoretical expectation. High line tensions are usually suspected to account for dissipations rather than for energetic contributions. Note also that if line tension is introduced as a thermodynamic quantity, it does not imply any distribution of stable contact angles, *i.e.* $\mathcal{A}_{eq}$ is a single value. Isa et al. have measured the contact angle of different nanoparticles of radii between 10 nm and 1.4 µm at the oil-water interface. They show a distribution of stable particle contact angles for each particle size. The width of the contact angle distribution becomes large if the particle size decreases. These important experimental findings have been discussed accounting for line tension ($k \approx 10^{-10}\ldots10^{-9}$ N) and Brownian motion. One might wonder if the distribution of $\mathcal{A}_{eq}$ could result from stable and metastable contact angles; but in this case the contact angle distribution would be bimodal or ill-defined and rather high (see Figure 2.3(B)). Brownian motion could explain a distribution of stable contact angle for small nanoparticles but not for large particles. Hence, observation of particle contact angle distributions may deserve further analysis and discussion in terms of contact line pinning.[16] Finally, for large drops or particles R, $R_0 > 0.1$ µm, line tension effects are in general negligible and the equilibrium contact angle remains the same if the size of the system is increased. For small drops or particles R, $R_0 < 0.1$ µm, equilibrium contact angle may become length scale dependent [17] and stable, metastable and unstable states could manifest.

2.3 Roughness and inhomogeneity effects on partial wetting

In order to describe partial wetting systems closer to the ones encountered in experiments, we should start describing the effects of surface defects. We start by considering the case of an homogeneous solid with roughness.

2.3.1 Roughness effects on partial wetting

Here, we assume that roughness is due to random topographical defects and could be modelled by geometrical functions. The main assumption here is that the liquid wets the solid such that no air trapping occurs, see Figure 2.4. Moreover the roughness is randomly distributed on the solid surface in a length scale much smaller than the system size. This approach is well-known in partial wetting of planar surface and named after "Wenzel".[18]

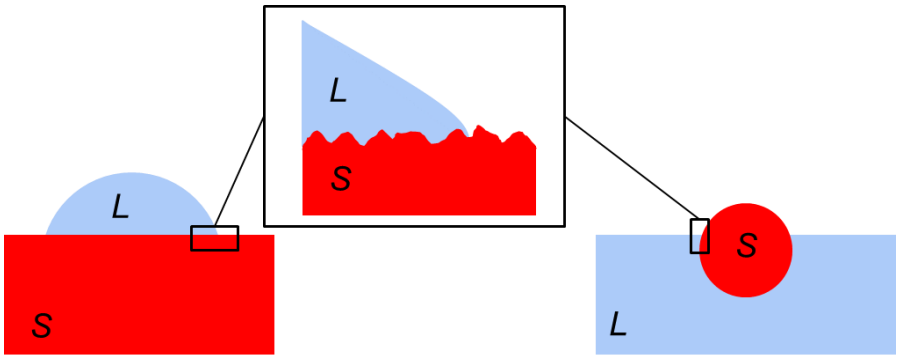

Figure 2.4 Wenzel model for drop and particle geometries.

For a liquid drop, in presence of surface roughness, the surface A_s of the solid-liquid and solid-gas interfaces becomes larger than the flat area A_0, $A_s = r\,A_0$, where r is the ratio between the real area and the projected flat area. Thus the free energy becomes:

$$E(\alpha) = \sigma_{SG}A - \sigma_{SG}A_s + \sigma_{SL}A_s + \gamma A_{LG}. \tag{2.12}$$

For a solid particle at a liquid-gas interface, decorated by defects as described before, the free energy reads:

$$E(\alpha) = \gamma A + 2\pi R^2\left[r\,\gamma_{SL}(1+\cos\alpha) + r\,\gamma_{SG}(1-\cos\alpha) - \frac{1}{2}\gamma\sin^2\alpha\right]. \tag{2.13}$$

In order to illustrate the effect of roughness on wetting, we model the roughness as composed by cylindrical defects of radius R_s and height h_s, which are homogenously present on the substrate with a surface fraction ϕ_s.

$$A_s = A_0(1 + 2\phi_s\frac{h_s}{R_s}), \tag{2.14}$$

Where $\phi_s = n_s\pi R_s^2$/(area of the solid surface) is the defect concentration (n_s is the number of defects) and the roughness is simply $r = (1 + 2\phi_s\frac{h_s}{R_s})$. In Figure 2.5 we plot the free energies for drop and particle geometries for different defect concentrations. Both for drop and particle geometries the energy minimum defines an equilibrium contact angle that follows the Wenzel equation:[18]

$$\cos\alpha_W = r\cos\alpha, \text{ where } r = A_s/A_0\ . \tag{2.15}$$

Plotting the energy profiles for different defect concentrations at $h_s/R_s = 1$, we note that for the drop geometry, an increase of r leads to a deeper energetic minimum. On the contrary, for the solid particle the energy minimum becomes shallower and could even vanish if r increases as for a particle decorated with surface defects covering 40% of the whole surface in Figure 2.5.[19] This result is rarely accounted in the literature and has a clear impact on the location [20] and irreversibility of particle adsorption onto the surface. It is important to recall that the Wenzel equation is not valid at all length scales. For solid surface showing large structures ($l > l_s$), the liquid drop may "feel" an effective flat solid interface composed by the solid and the infiltrated liquid.

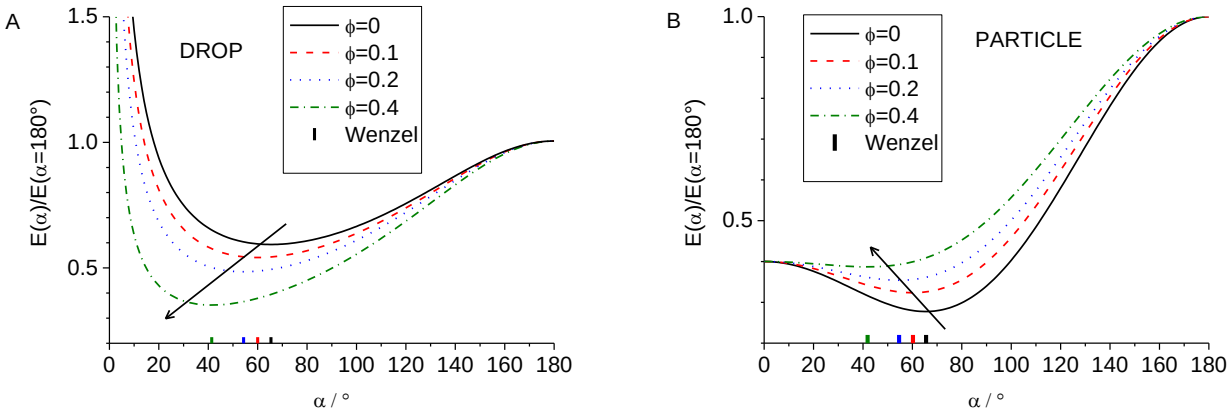

Figure 2.5 A) Free energy ratio $E(\alpha)/E(\alpha=180°)$ ($\alpha_E = 65°$ and $\gamma = 72$ mN/m, $h_s/R_s = 1$, $\sigma_{SG}A$ is a constant of the system and its contribution was subtracted to E) as a function of α for the drop geometry and different defect concentrations ϕ_s. B) Free energy ratio $E(\alpha)/E(\alpha=180°)$ ($\alpha_E = 65°$ and $\gamma = 72$ mN/m, $h_s/R_s = 1$, γA is a constant of the system and its contribution was subtracted to E) as a function of α for the particle geometry and different defect concentrations ϕ_s. In the x-axis, data points show the equilibrium contact angles calculated using the Wenzel equation.

The latter case corresponds to a Cassie-Baxter state. For larger surface structures and equilibrium contact angle $\alpha_E > \alpha_c = \arccos\frac{1-\phi_S}{r-\phi_S}$, the Wenzel equation is valid. For $\alpha_E < \alpha_c$ the Cassie-Baxter model introduced in the next section should be used.[6]

2.3.2 Inhomogeneity effects on partial wetting

Beside roughness, a second scenario accounting for flat but heterogeneous solid surface can be discussed. If the solid surface is composed by two materials showing different surface energies randomly distributed on the whole surface, one refers to the "Cassie-Baxter" wetting state [6]. For planar solids with area fractions ϕ of materials 1 and 2, $\phi_1 + \phi_2 = 1$:

$$E(\alpha) = \phi_1(\sigma_{S1G}A - \sigma_{S1G}A_0 + \sigma_{S1L}A_0) + \phi_2(\sigma_{S2G}A - \sigma_{S2G}A_0 + \sigma_{S2G}A_0) + \gamma A_{LG} . \quad (2.16)$$

At the energy minimum, the "Cassie-Baxter" contact angle is defined as:[6]

$$\cos\alpha_{CB} = \phi_1\cos\alpha_{E,1} + \phi_2\cos\alpha_{E,2} . \quad (2.17)$$

Note that the previous equations are equivalent to the equations for homogenous solid surfaces if written in terms of effective surface energies, $\sigma_{SMG} = \sigma_{S1G}\phi_1 + \sigma_{S2G}\phi_2$ and $\sigma_{SML} = \sigma_{S1L}\phi_1 + \sigma_{S2L}\phi_2$:

$$E(\alpha) = \sigma_{SMG}A - \sigma_{SMG}A_0 + \sigma_{SML}A_0 + \gamma A_{LG} . \quad (2.18)$$

The same analysis applies to the spherical particle geometry. Two remarks can be now made. First, assuming that inhomogeneity is randomly distributed in a small scale compared to the system size we are always assuming that on average the contact line touches the two regions 1 and 2 with the same fraction as the area fraction. Note that if inhomogeneity is either on a scale comparable to the system size or structured in defined patterns, equations 2.17 does not hold anymore.[21,22] An exemplar case is represented by a drop sitting on a substrate with a single circular domain made of a different material.[23] If the drop sits inside the domain the equilibrium contact angle is the one of the material's domain. If the drop is larger than the domain and the domain is included in the drop, the equilibrium contact angle is the one of the substrate even if there is a large area fraction of the domain. For these particular cases where the heterogeneity length scale is large, it becomes clear that the relevant fractions ϕ in Equation

2.17 are not the area but the line fractions.[23] A long debate exists in the literature about this topic and the validity of Wenzel and Cassie-Baxter models.[23,24, 34–37,29]

To further discuss the wetting of heterogeneous surfaces, and illustrate whether line or area fractions should be used in equation 2.17, we consider the cases of the partial wetting of Janus and patchy particles. A very rich behavior can be discussed when considering a Janus particle composed by two hemispherical faces with different contact angles at a liquid-gas interface [30,31]. If one Janus face possesses an equilibrium contact angle larger than 90° and the other face lower than 90°, the free energy shows a minimum and a singular point at 90°, corresponding to a four-phase contact line where the two solid faces, the liquid and the gas meet.[31] If both faces show equilibrium contact angles lower (or higher) than 90°, stable, unstable and metastable wetting states can be described depending on the orientation of the particle, see Figure 2.6. When the Janus boundary is not crossing the liquid-gas, the contact line touches only one face of the Janus particle. When the contact line touches the face with the highest contact angle $\alpha_{E,1}$, the Janus particle finds a stable contact angle at $\alpha_{E,1}$.[32] If, instead, the contact line touches the face with the lowest contact angle $\alpha_{E,2}$, the Janus particle may remain at metastable contact angle equal to $\alpha_{E,2}$.[19] Note that in this geometry the heterogeneity has the same size of the particle and Cassie-Baxter model does not apply. If the Janus particle is oriented with the Janus boundary crossing the liquid-gas interface, no equilibrium can be found if the liquid-gas interface keeps flat.[19,33] A different scenario can be discussed for patchy particles. If a patchy particle possesses randomly distributed regions of two materials of sizes much smaller than the particle size, the contact line will intimately touch both regions. In this case a Cassie-Baxter regime can be expected and the stable particle contact angle will be defined by Equation 2.17.

2.4 Contact line pinning and contact angle hysteresis

Roughness and inhomogeneity of the surface have major impacts not only on the static but also on the dynamic of partial wetting. Contact line pinning occurs whenever a defect is present on the solid surface. Hence the liquid interface deforms around the physical or chemical defect dissipating energy and leading to contact angle hysteresis.

2.4.1 Deformation of the liquid interface

Even in absence of surface defects the contact line may show some weak distortions, e.g. due to thermal motion. As described by Joanny and de Gennes,[34] we consider a distortion of the contact line on the solid along the x-axis, whose displacement is $u(x)$ (at y=0) and its wave vector q, see Fig. 2.7(a) and (b). As the line is displaced on the solid, also the liquid surface will be perturbed. The distortion along the x-axis and the Laplace's equation lead to a liquid surface displacement:

$$z(x,y) = \alpha y + \frac{1}{2\pi}\int_{-\infty}^{+\infty} u_q \mathrm{e}^{iqx}\mathrm{e}^{-|q|y} dq. \tag{2.19}$$

Significant distortion of the liquid surface happens over a distance q^{-1} close to the solid comparable to the periodicity of the distortion of the contact line on the solid. The amplitude of the distortion u_q is also fixed by the displacement $u(x)$.

Now we summarize the calculation of the displacement of the contact line assuming an heterogeneous surface, showing weak defect forces that act as random fluctuating forces $f(x)$. In Figure 2.7(b), fluctuations of the contact line are sketched, they follow:[34]

$$< [u(x)- u(0)]^2 >=2D|x| . \tag{2.20}$$

Where $D = \frac{1}{\gamma^2\alpha^4}\int_0^{+\infty} < f(0)f(x) > dx$. These contact line fluctuations can be significant. The amplitude of the distortion scales as $u^2 \sim L\xi$, where ξ is the correlation length of the defect and L is the system size.[34] Considering both a planar surface and a solid particle geometries, if ξ = 1 nm and L = 1 µm, the amplitude of the contact line displacement is about 30 nm.

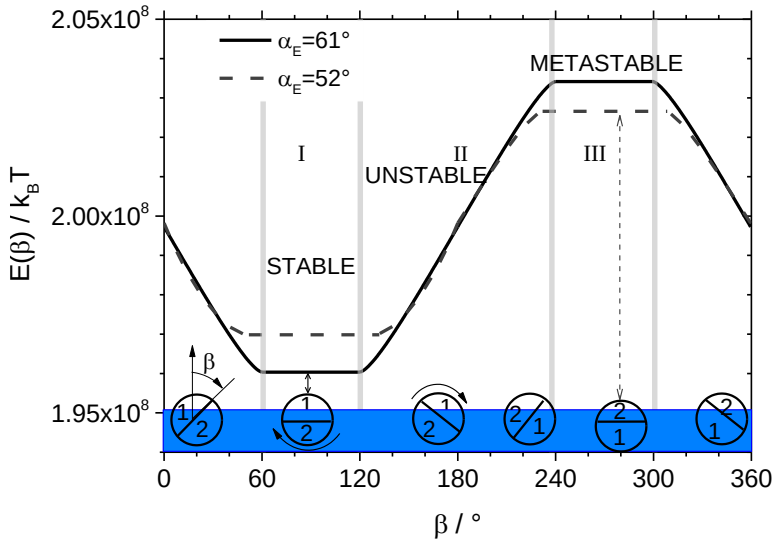

Figure 2.6 Free energy (γ = 72 mN/m, R = 1 µm, γA is a constant of the system and its contribution was subtracted to E) of a Janus particle as a function of the orientation β (defined in the left bottom corner) for two different position corresponding to the equilibrium contact angles of each face of the Janus particle [35].

Note that the latter value is much greater than the amplitude of thermal capillary waves[36] (≈0.2 nm) or the characteristic displacement in the Molecular-kinetic model for friction of partial wetting (0.1-1 nm).[37]

In presence of an isolated defect of size d and force $f_d = \gamma d\,[\cos(\alpha_d) - \cos\alpha]$, (where α_d is the contact angle on the defect, see Figure 2.7) the contact line on the solid takes the form, see Figure 2.7(c):[34]

$$u(x) = \frac{f_d}{\pi\gamma \sin^2\alpha} \ln\left(\frac{L}{|x|}\right), \tag{2.21}$$

where L is a macroscopic distance, which could be either the system size or the distance between two adjacent pinning points.

2.4.2 Weak or strong pinning

Weak or strong pinning of the contact line on a single defect may occur depending on the amplitude f_0 of the defect force $F_D = f_0(y_m - y_d)$ with respect to the restoring force $F_R = K(y_m - y_L)$ of the liquid tail, see Figure 2.7(c). y_m is the actual position of the line, y_d is the defect position, $K = \pi\gamma\sin^2\alpha/\ln(L/d)$ (see equation 2.21) is the spring constant of the restoring force and y_L is the position of the contact line in absence of the defect, see Figure 2.7(c).[34,38]

For weak defects, f_0/K is small and no hysteresis of the contact angle is expected. For strong defects, f_0/K is large and contact angle hysteresis occurs. The contact line is pinned on the defects and only if enough energy is injected into the system, a line displacement will occur towards a new position. The limiting values of stable macroscopic contact angles are the advancing α_A and receding α_R contact angles. For a spherical colloid, α_A is the stable angle reached after a displacement of the contact line resulting in an increase of the colloid wetted area; whereas α_R is the angle reached after a displacement of the contact line resulting in a decrease of the wetted area of the colloid,[19] see Figure 2.7(d) and (e).

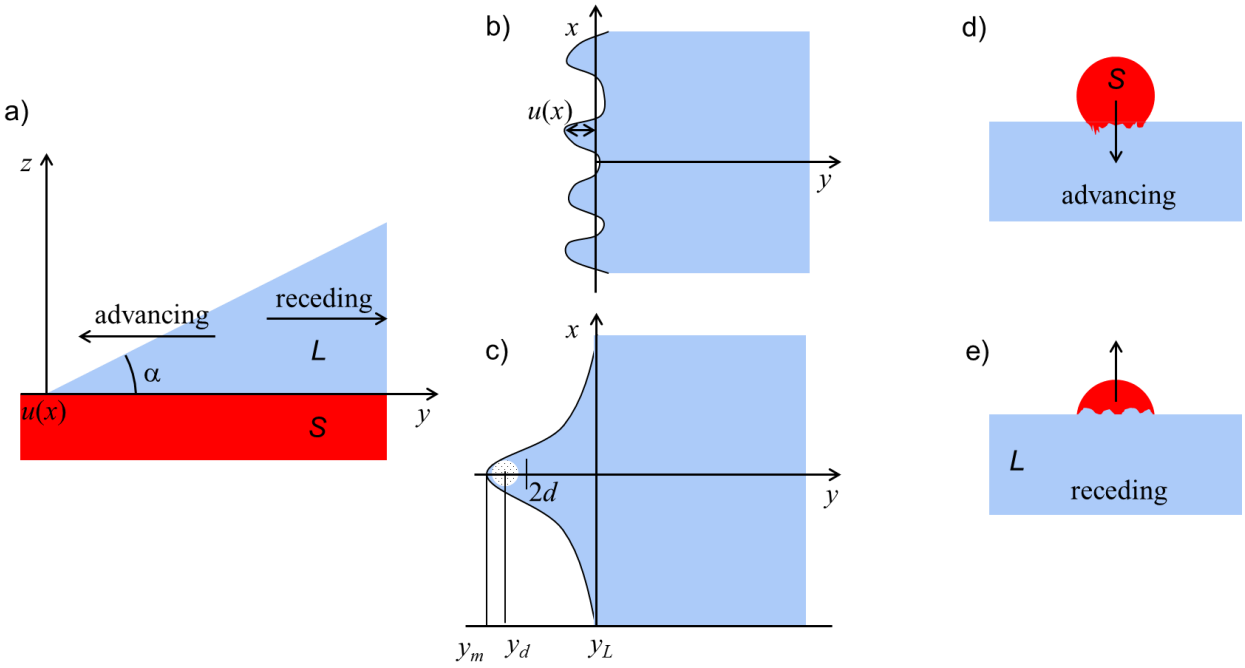

Figure 2.7 a) Side view of a drop wedge at a given contact angle α and directions of advancing and receding contact lines. b) Top view of the contact line region in absence of strong defects. c) Top view of the contact line region in presence of a strong defect inducing line pinning. d) Side view of a solid particle immerging in a liquid with an advancing contact line. e) Side view of a solid particle emerging from a liquid with a receding contact line.

2.4.3 Contact angle hysteresis

In the case of strong defects, stable contact angles can be defined by balancing the work $F_l\Delta y$ done by the force F_l (equation 2.5 and 2.6), which tends to move the line towards α_E after a displacement Δy, and the energy dissipated by the defects. For isolated non-interacting defects:[6]

$$F_l\Delta y = \phi\Delta y R_i \sin\alpha\, W, \tag{2.22}$$

where ϕ is the number of defects per unit area, $\Delta y R_i \sin\alpha$ is the area defined by the displacement Δy, where $R_i = R_0(\alpha)$ for the drop, and $R_i = R$ for the particle geometry respectively. W is the specific energy of a defect, which can be calculated at the maximum elongation $u_m = K^{-1}f_m$ (see equation 2.22) before the line snaps from the defect. Considering the case of isolated defects of size d, see Figure 2.7(c):[34]

$$W = \frac{1}{2}Ku_m^2 = \frac{f_m^2 \ln(L/d)}{\gamma\pi\sin^2\alpha}. \tag{2.23}$$

In the case of surface roughness, instead, the specific energy W of a topographical defect of size d and height h can be written as:[39]

$$W = \frac{\gamma d^2 \sin^2\left(\frac{dh}{dy}\right)\ln(L/d)}{2\pi}. \tag{2.24}$$

Where $\frac{dh}{dy}$ is the derivative of the profile height along the y-axis. Assuming that energies dissipated during a contact line advancing and receding steps are the same, one writes the contact angle hysteresis as:

$$\cos\alpha_R - \cos\alpha_A = \phi\, 2W, \tag{2.25}$$

which increases linearly with the defect concentration ϕ. For concentrated interacting defects the linear dependency does not hold anymore.[40]

Many theoretical and experimental investigations have been carried out for drop contact angle hysteresis on solid substrates in presence of defects of different sizes and structures [34,41–43]. For spherical solid particles at the liquid interface very rarely contact angle hysteresis has been investigated or discussed.[44,19,45] Many experimental investigations report on particle contact angle[46] but very few experiments have described distributions of particle contact angles, which we believe are very important to describe line pinning.[47,16]

2.5 Contact line dynamics and frictions

For the planar surface geometry and as well for a particle at a liquid interface, two main sources of dissipations in partial wetting dynamics have been discussed in the literature.[48,37,49,50] We are now concerned with the dynamics of drops or particles occurring during the path from a non-wetting state (α =0 or 180°) to an equilibrium position (α_E). We assume that the velocity v_y and the capillary number Ca = $\eta\, v_y /\gamma$ are very small <<1, where η is the dynamic viscosity of the liquid. Two main length scales define the sources of dissipations, which are due to the viscous stresses and molecular frictions. For length scales larger than the molecular size (or l_s), viscous flows and stresses are generated upon the relative motion between a liquid and a solid with a velocity v_y.

The power dissipated as a function of the contact angle can be written as [51]:

$$\Omega = 4g(\alpha)\eta {v_y}^2 \ln\left(\frac{R_i}{a}\right) 2\pi R_i \sin\alpha. \tag{2.26}$$

Where $R_i = R_0(\alpha)$ is the drop radius for the planar surface geometry and $R_i = R$ is the particle radius for the particle geometry; a is a molecular size and $g(\alpha)$ is a function of the contact angle: $g(\alpha)\approx 0.756/\alpha - 0.084\alpha$.[51] For small contact angles $\alpha << 45°$, $g(\alpha) = 3/(4\alpha)$ and $\Omega = \frac{3\eta v_y^2}{\alpha} \ln\left(\frac{R_i}{a}\right) 2\pi R_i \sin\alpha$.[6] If one writes Ω as a force F_{visc} times a velocity, a viscous friction coefficient, $\zeta_{visc} = F_{visc} / v_y = \Omega/v_y^2$, can be written as:

$$\zeta_{visc} = 4g(\alpha)\eta \ln\left(\frac{R_i}{a}\right) 2\pi R_i \sin\alpha. \tag{2.27}$$

Note that this friction does not depend neither on the interfacial tension nor the equilibrium contact angle but it depends only on the viscosity and the geometric contact angle (or dynamic contact angle) experienced during the path from a non-wetting state (α =0 or 180°) to an equilibrium position (α_E). It is important to mention that an additional source of viscous dissipation occurs in the presence of a precursor film, which is particularly relevant in complete wetting.[52,39] To the best of our knowledge, the existence of such a precursor film has been never discussed in the complete wetting of solid particles. The existence of such film may occur when hydrophilic particles are deposited on top of a liquid surface in a dry state or using a spreading solvent.

The second source of dissipation is due to molecular frictions. When dealing with length scale comparable to the thermal length $l_T = \left[\frac{k_B T}{\gamma}\right]^{1/2}$, a molecular kinetic theory should be applied to evaluate the dissipation. Thermal agitation energy $k_B T$ leads to contact line jumps over distances λ occurring at a characteristic time τ_L. This molecular line friction reads:[37,53,54]

$$\zeta_{line} = \frac{k_B T}{\lambda^3}\tau_L\, 2\pi R_i \sin\alpha, \text{ and:} \tag{2.28}$$
$$\tau_L \cong \frac{\eta v_m}{k_B T} \exp\frac{E_a}{k_B T}\ .$$

Where v_m is the molecular volume of the liquid and E_a is the activation energy needed for the line jump. Usually E_a is written in the form of an adhesion energy $E_a = \lambda^2\gamma(1+\cos\alpha_E)$.[37] However, it is important to remark that the line jump occurs at the molecular level whereas the equilibrium contact angle in the adhesion energy is defined in the macroscopic level. Thus, one may wonder if instead of α_E one should consider the local contact angle which account for long range surface forces selected at a length scale set by λ, see Figure 1.4.

In Figure 2.8 we plot the viscous and line frictions for drop and particle as a function of α. Viscous friction is extremely high for the drop geometry at low contact angles given that the drop radius is very high. If α increases, the friction decreases significantly and it becomes comparable to the Stokes friction ($6\pi\eta R$) of a rigid sphere immersed in a liquid. For a particle, the viscous friction is also high at low contact angles but it does not decrease so sharply as for the drop geometry given that the length of the contact line is 0 at $\alpha = 0$ and maximum at $\alpha = 90°$. Line friction coefficients depend strongly on λ and the activation energy, which depends on γ and α_E. For a typical values $\lambda = 0.6$ nm and $\alpha_E = 90°$,[37] line frictions can be smaller than the viscous frictions at low contact angles but they become higher than the viscous frictions for $\alpha > 20°$. For the particle geometry it is important to remark that the highest line friction is reached at $\alpha = 90°$, where the line length is at maximum.

Now we can briefly discuss the equation of motion of the contact line for a drop or a particle considering the particular case of driving force plotted in Fig. 2.2 for $\alpha_E = 65°$. For a drop starting at $\alpha = 180°$ the viscous and line friction are low and the force increases if α decreases, hence the line will move towards the equilibrium contact angle. It may approach but never reach the equilibrium in a reasonable experimental time, given that the force decreases and the frictions increases when α gets close to α_E. For a particle starting at $\alpha_E = 180°$ the motion may slow down well before α_E because line friction is maximum at $\alpha = 90°$. Also for a particle starting at $\alpha = 0°$ it is important to remark that the driving force is low and the viscous friction is very high at low contact angles.

Partial wetting dynamics for drops have been largely explored theoretically and experimentally and combined viscous and line friction models have been also used.[55,56,6,39] On the contrary, very few experiments have been carried out for the dynamics of particle at the liquid interface. The slow dynamics of a particle breaching an oil-water interface have been recently investigated by Kaz et al..[50] They indeed observed that particles either are not able to breach the interface or they move very slowly at the interface. These results agree with our discussion before, see Fig. 2.8. Dynamics of dewetting is also largely reported in the literature for liquids on solid substrates.[57,58] Nucleation of dry region on the solid surface may occur due to surface defects or by the amplification of capillary waves.[59] Also in this case, we are not aware of experimental studies on details of dewetting mechanisms for particles at the liquid interface.

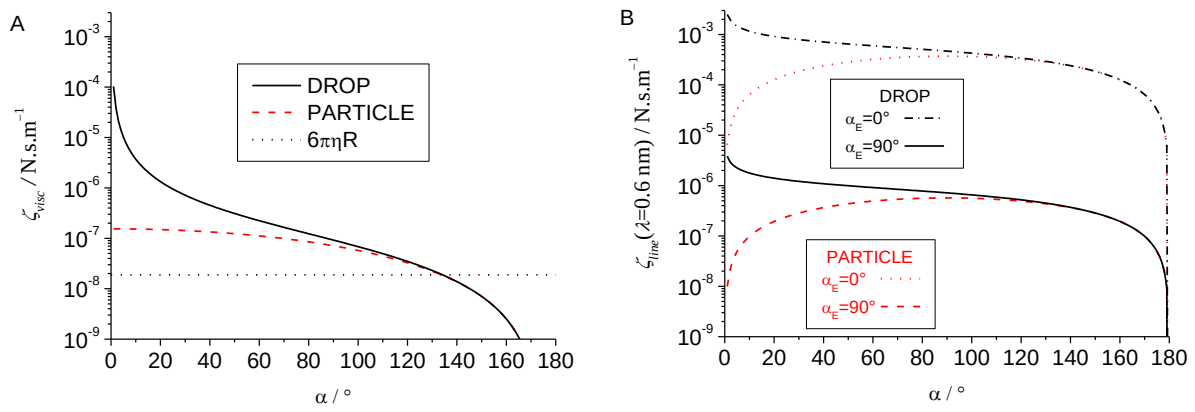

Figure 2.8 A) Viscous friction coefficient as a function of the dynamic angle α for the drop and particle geometries ($\eta = 10^{-3}$ Pa.s, $R = R_0(\alpha=180°) = 1$ µm). B) Line friction coefficients for drop and particle geometries for two different values of α_E ($\gamma = 72$ mN/m, $R = R_0(\alpha=180°) = 1$ µm).

Finally, viscous and line frictions do not affect only the contact line motion during a partial wetting dynamic towards equilibrium. For particles straddling an interface at a constant contact angle, even if the contact angle does not vary, the contact line may fluctuate and a line friction could manifest. Recent experiments on particle lateral and the rotational motions show the strong influence of the viscous and line frictions due to contact line fluctuations, which decrease the particle diffusion coefficients.[60,61,19]

2.6 Conclusion

Here, we describe fundamental aspects of the partial wetting for drops and particles. Even if theoretical and experimental works have been extensively done, many new investigations deserve consideration. For smooth surfaces, line tension could affect the wetting of drop or particles of small sizes in a very different way. New experiments for nanodrops and for particles of different aspect ratios (ellipsoids or disks) and contact angles could be designed in order to address line tension effects. It would be also interesting to gain some control on the sign and value of the line tension by using line-active molecules able to tune line tension in the partial wetting of drops and particles. For particles, the impact of surface roughness could be severe. Note that not only the contact angle may shift, but also that the adsorption energy minima $\Delta E_W = E(\alpha) - E(\alpha = 0 \text{ or } 180°)$ could reduce or even vanish. Patchy and Janus particles could be used for experimental investigations in order to elucidate on the applications of the Cassie-Baxter model. Finally, new experiments on contact angle distributions and dynamics of particles at the water surface may provide new insights into the physics of contact line pinning and line frictions, that can be compared to the results obtained for drops.

2.7 References

1 P. G. De Gennes, X. Hua and P. Levinson, *J. Fluid Mech.*, 1990, **212**, 55–63.
2 A. Sharma, *Langmuir*, 1993, 3580–3586.
3 P. Pieranski, *Phys. Rev. Lett.*, 1980, **45**, 569.
4 R. Aveyard and J. H. Clint, *J. Chem. Soc. Faraday Trans.*, 1996, **92**, 85.
5 J. Drelich, *Colloids Surfaces A Physicochem. Eng. Asp.*, 1996, **116**, 43–54.
6 P.-G. De Gennes, F. Brochard-Wyart and D. Quéré, *Capillarity and Wetting Phenomena*, 2004.
7 A. R. Honerkamp-Smith, P. Cicuta, M. D. Collins, S. L. Veatch, M. den Nijs, M. Schick and S. L. Keller, *Biophys. J.*, 2008, **95**, 236–246.
8 A. J. García-Sáez, S. Chiantia and P. Schwille, *J. Biol. Chem.*, 2007, **282**, 33537–33544.
9 U. Delabre and A. M. Cazabat, *Phys. Rev. Lett.*, 2010, **104**, 2–5.
10 A. Dehghan, K. A. Pastor and A. C. Shi, *Phys. Rev. E - Stat. Nonlinear, Soft Matter Phys.*, 2015, **91**, 1–8.
11 L. Dong and D. T. Johnson, *Langmuir*, 2005, **21**, 3838–3849.
12 T. Getta and S. Dietrich, *Phys. Rev. E*, 1998, **57**, 655–671.
13 A. Amirfazli and A. W. Neumann, *Adv. Colloid Interface Sci.*, 2004, **110**, 121–141.
14 D. Lohse and X. Zhang, *Rev. Mod. Phys.*, 2015, **87**, 981–1035.
15 S. P. McBride and B. M. Law, *Phys. Rev. Lett.*, 2012, **109**, 1–5.
16 L. Isa, F. Lucas, R. Wepf and E. Reimhult, *Nat. Commun.*, 2011, **2**, 438.
17 A. Stocco and H. Möhwald, *Langmuir*, 2015, **31**, 11835–11841.
18 R. N. Wenzel, *J. Ind. Eng. Chem. (Washington, D. C.)*, 1936, **28**, 988–994.
19 X. Wang, M. In, C. Blanc, P. Malgaretti, M. Nobili and A. Stocco, *Faraday Discuss.*, 2016, **191**, 305–324.
20 A. San-Miguel and S. H. Behrens, *Langmuir*, 2012, **28**, 12038–12043.
21 P. Lenz and R. Lipowsky, *Phys. Rev. Lett.*, 1998, **80**, 1920–1923.
22 P. Blecua, R. Lipowsky and J. Kierfeld, 2006, 11041–11059.
23 C. W. Extrand, *Langmuir*, 2003, **19**, 3793–3796.
24 A. Milne and A. Amirfazli, *Adv. Colloid Interface Sci.*, 2012, **170**, 48–55.

25 T. L. Liu, Z. Chen and C.-J. Kim, *Soft Matter*, 2015, **11**, 1589–1596.
26 Y. Kwon, S. Choi, N. Anantharaju, J. Lee, M. V. Panchagnula and N. A. Patankar, *Langmuir*, 2010, **26**, 17528–17531.
27 S. T. Larsen and R. Taboryski, *Langmuir*, 2009, **25**, 1282–1284.
28 L. Gao and T. J. McCarthy, *Langmuir*, 2007, **23**, 3762–3765.
29 A. Marmur and E. Bittoun, *Langmuir*, 2009, **25**, 1277–81.
30 C. Casagrande, P. Fabre, E. Raphaël and M. Veyssié, *Europhys. Lett.*, 2007, **9**, 251–255.
31 T. Ondarçuhu, P. Fabre, E. Raphaël and M. Veyssié, *J. Phys.*, 1990, **51**, 1527–1536.
32 R. Aveyard, *Soft Matter*, 2012, **8**, 5233.
33 H. Rezvantalab and S. Shojaei-Zadeh, *Soft Matter*, 2013, **9**, 3640.
34 J. F. Joanny and P. G. De Gennes, *J. Chem. Phys.*, 1984, **81**, 552.
35 X. Wang, M. In, C. Blanc, P. Malgaretti and M. Nobili, .
36 D. Bonn and G. Wegdam, *J. Phys.*, 1992, **2**, 1755.
37 T. D. Blake, *J. Colloid Interface Sci.*, 2006, **299**, 1–13.
38 S. Ramos and a Tanguy, *Eur. Phys. J. E. Soft Matter*, 2006, **19**, 433–40.
39 P. G. De Gennes, *Rev. Mod. Phys.*, 1985, **57**, 827–863.
40 M. Ramiasa, J. Ralston, R. Fetzer and R. Sedev, *Adv. Colloid Interface Sci.*, 2014, **206**, 275–293.
41 A. Giacomello, L. Schimmele and S. Dietrich, *Proc. Natl. Acad. Sci.*, 2015, 201513942.
42 M. Reyssat and D. Quéré, *J. Phys. Chem. B*, 2009, **113**, 3906–3909.
43 J.-M. Di Meglio and D. Quéré, *Europhys. Lett.*, 2007, **11**, 163–168.
44 M. Preuss and H. Butt, *J. Colloid Interface Sci.*, 1998, **208**, 468–477.
45 A. Stocco, G. Su, M. Nobili, M. In and D. Wang, *Soft Matter*, 2014, 6999–7007.
46 A. Maestro, E. Guzmán, F. Ortega and R. G. Rubio, *Curr. Opin. Colloid Interface Sci.*, 2014, **19**, 355–367.
47 C. Snoeyink, S. Barman and G. F. Christopher, *Langmuir*, 2015, **31**, 891–897.
48 F. Brochard-Wyart and P. G. De Gennes, *Adv. Colloid Interface Sci.*, 1992, **39**, 1.
49 J. H. Snoeijer and B. Andreotti, *Annu. Rev. Fluid Mech.*, 2013, **45**, 269–292.
50 D. M. Kaz, R. Mcgorty, M. Mani, M. P. Brenner and V. N. Manoharan, *Nat. Mater.*, 2012, **11**, 138–42.
51 H.-Y. Kim, H. J. Lee and B. H. Kang, *J. Colloid Interface Sci.*, 2002, **247**, 372–380.
52 M. N. Popescu, G. Oshanin, S. Dietrich and A. M. Cazabat, *J. Phys. Condens. Matter*, 2012, **24**, 243102.
53 T. D. Blake and Y. D. Shikhmurzaev, *J. Colloid Interface Sci.*, 2002, **253**, 196–202.
54 D. Duvivier, D. Seveno, R. Rioboo, T. D. Blake and J. De Coninck, *Langmuir*, 2011, **27**, 13015–21.
55 P. Petrov and I. Petrov, *Langmuir*, 1992, **8**, 1762–1767.
56 M. J. De Ruijter, J. De Coninck and G. Oshanin, *Langmuir*, 1999, **15**, 2209–2216.
57 C. Redon, F. Brochard-Wyart and F. Rondelez, *Phys. Rev. Lett.*, 1991, **66**, 715–718.
58 E. Bertrand, T. D. Blake and J. De Coninck, *Colloids Surfaces A Physicochem. Eng. Asp.*, 2010, **369**, 141–147.
59 R. Seemann, S. Herminghaus and K. Jacobs, *Phys. Rev. Lett.*, 2001, **86**, 5534–5537.
60 G. Boniello, C. Blanc, D. Fedorenko, M. Medfai, N. Ben Mbarek, M. In, M. Gross, A. Stocco and M. Nobili, *Nat. Mater.*, 2015, **14**, 908–11.
61 G. Boniello, A. Stocco, M. Gross, M. In, C. Blanc and M. Nobili, *Phys. Rev. E*, 2016, **94**, 12602.

Chapter 3

Nanoparticle Contact Angles at Fluid Interfaces by Ellipsometry

3.1 Introduction

In this chapter, we show experimental results on in-situ contact angles of nanoparticles at the fluid interfaces. These experimental results are compared with the contact angles of sessile drops on planar surfaces. As pointed out in Chapter 1 and 2, we can connect the in-situ contact angle to the local contact angle α_L which reflect the contributions of long-range surface forces and capillarity. These contributions depend strongly on the size of the nanoparticle and its immersion.

The measurement of the equilibrium contact angle of solid particles at the fluid interface is crucial to understand and predict dispersion, stabilization, phase transfer, and phase inversion in dispersed multiphase systems such as Pickering emulsions and particle stabilised foams.[1] When particles possess sizes in the colloidal scale, equilibrium contact angle is determined not only by capillarity but also by various colloidal interactions.[2] Hence, the equilibrium contact angle of a colloidal particle can differ significantly from the macroscopic equilibrium contact angle measured by the far field view of a drop deposited on a support made of the same material.

Gehring and Fischer reported that the immersion of nanoparticles (NPs) at the water-air interface depend strongly on the ionic strength and the surface potential of water and the NPs.[3,4] The contact angles of negatively charged NPs decrease with the ionic strength increasing, whereas positively charged NPs behave oppositely.[5] In Pickering emulsions, it has been also reported that interfacial electrostatics strongly affects the interfacial curvature of the emulsion droplets, which is related to the partitioning of particles at the oil/water interface.[6] For core-shell NPs, recent simulation studies suggest that the hydrophobicity of polymer shells strongly affects the position of the NPs relative to the interface.[7,8]

Up to date, however, it remains an experimental challenge to in situ measure the location of colloidal particles at the fluid interface, particularly when the particle size is in the nanometric range and the liquid-liquid interface is considered. To overcome the experimental challenge, several indirect contact angle measurements were developed.[9,10,11] New methods based on X-Ray or Neutron Reflectivity measurements have recently been proposed.[12,13] Nonetheless, the most popular method to evaluate the contact angle of colloidal particles at the fluid interface is to measure macroscopic contact angles (advancing and receding) of sessile drops. It is also widely accepted that the equilibrium contact angle of an isolated colloid at the fluid interface is equivalent to the macroscopic equilibrium contact angle of model planar substrates.[14,15] These two contact angles, however, differ in terms of probed length scales, interactions, and phenomena.[2]

Herein the contact angle and surface coverage of responsive gold NPs at water-oil and water-air interfaces have been measured directly by ellipsometry. Multiple angle of incidence ellipsometry was already used to measure the contact angle and surface concentration of NPs at the liquid-gas interface.[16,17] Here, we implemented a cylindrical sample holder into the experimental setup to investigate also liquid-liquid interfaces without the need of using optical waveguides.[18] Multiple angle of incidence ellipsometry has been used to study NPs at water-toluene and water-air interfaces. This investigation aims at shedding light on the mechanism of responsive gold NP adsorption to and especially desorption to the oil phase across the water-oil interfaces reported in recent publications.[19,20] NP adsorption at water-air interfaces was also investigated as reference, in which no NP transfer to the

air across the water-air interfaces could take place. The present work focused on the study of the effect of two different salts, NaCl and NaOH, occurring at room temperature. NaCl is expected to increase the responsive gold NP surface hydrophobicity and thus lower the interfacial potential barrier, which drives to NP transfer from water to toluene across the water-toluene interface. NaOH is expected to promote the surface hydration and affinity with the aqueous medium, which drives to NP transfer from toluene to water.[20] As suggested in literature, it is worth noting that (i) no phase transfer was observed at room temperature in the absence of salt, and (ii) responsive gold NPs transfer from water to toluene in presence of NaCl but do not transfer back to water when salty water is replaced by pure de-ionized water.

3.2 Materials and methods

3.2.1 Responsive Gold nanoparticles

Citrate-stabilized gold NPs were coated with the chains of random copolymers of 2-(2-methoxyethoxy)ethyl methacrylate (MEO_2MA) and oligo(ethylene glycol) methyl methacrylate (OEGMA) via ligand exchange, as described in our previous reports.[18] The polymers were synthesized *via* atom transfer radical polymerization using disulfide initiators and the polymer used in this work had a MEO_2MA-to-OEGMA molar ratio of 90:10. The number averaged hydrodynamic radius of naked gold NP cores (R_1) is 9.2 nm and the core-shell NP radius (R_2) is 13.8 nm, measured by dynamic light scattering (see Fig. 3.1(A) and (B)). The refractive index of gold nanoparticle at the wavelength λ_0 = 533 nm is n_{NP} = 0.63–2.30i, and density 19.3 g cm^{-3}.[21,22,23]

The water used is Milli-Q water. Toluene (Sigma-Aldrich), NaCl (Sigma-Aldrich) and NaOH (Sigma-Aldrich) were used as received.

3.2.2 Sample preparation for ellipsometry measurements

The sample holders used for ellipsometry were cylindrical glass cells (7 cm diameter, 8.5 cm length, interface area A = 59.5 cm^2 and total Volume 208 cm^3). The cells were half filled with water and half with either oil or air. The cells were precisely aligned in the center of the ellipsometer (Optrel, Germany) to ensure the normal incidence of the laser beam on the glass and thus to avoid refraction and reflection of the incident and secondary reflected beams on the cell walls (see Fig. 3.1(C)).[18] The interface level was adjusted to be in the correct vertical position, namely, at the center of the goniometer.

1 mL of the relatively concentrated aqueous dispersion of responsive gold NPs was added to the cells to reach a NP concentration of c_{NP} =1 gL^{-1} in the water phase in the cells, corresponding to a volume fraction of $5 \cdot 10^{-5}$. Afterwards, the cells were shacked in order to quickly form homogenous NP dispersions. The filled cells were closed during experiments to avoid contamination of the interfaces. Measurements were carried out at room temperature T = 22 °C.

3.2.3 Ellipsometry and modelling of NPs at interfaces

Ellipsometry measures Ψ and Δ which lead to the ratio of reflection field coefficient r_P (*P*-polarization, parallel to the reflection plane) and r_S (*S*-polarisation, perpendicular to reflection plane):[24]

$$\frac{r_P}{r_S} = \tan\Psi \exp(i\Delta), \tag{3.1}$$

where r_P/r_S depends on the profile of the refractive index $n(z)$ or dielectric constant $\varepsilon(z) = n(z)^2$ across the interface, the bulk refractive indices (n_i), the laser wavelength (λ_0) and the angle of incidence (φ).

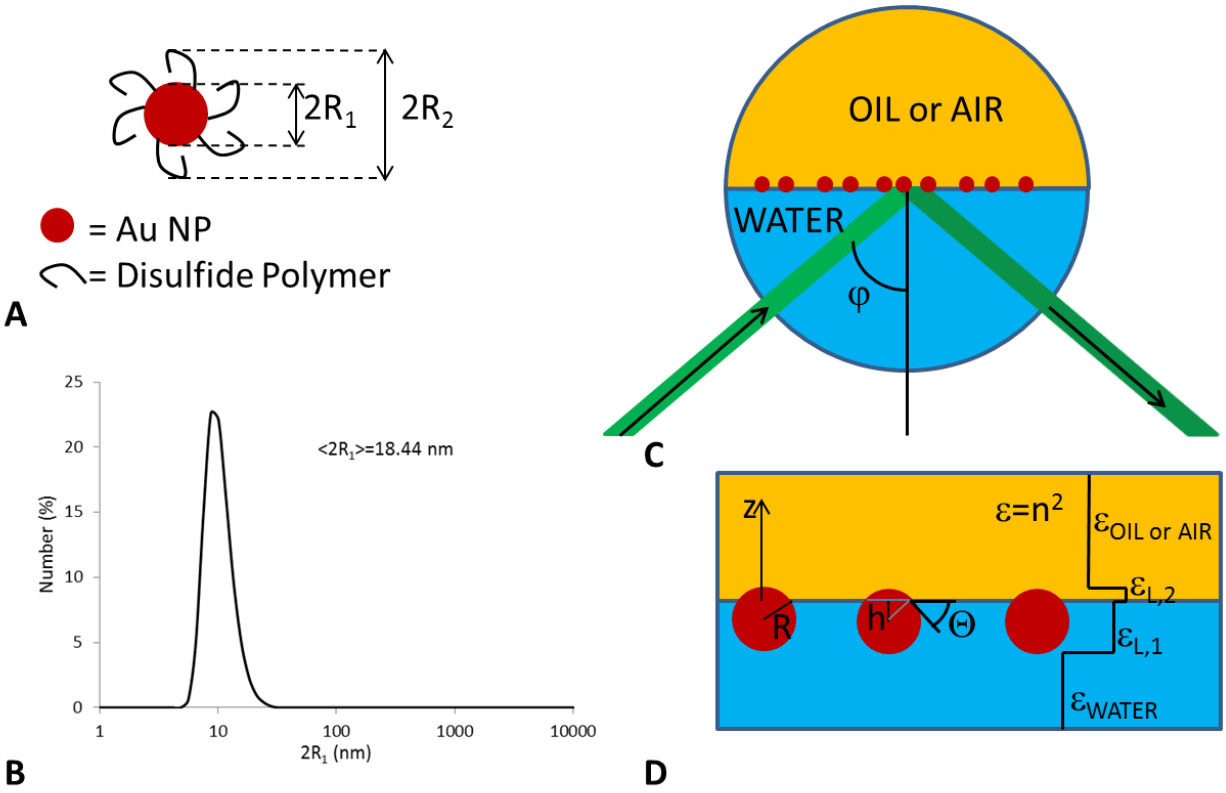

Figure 3.1 (A) Sketch of the core-shell NP and corresponding radii. (B) Number distribution of necked gold NPs obtained by dynamic light scattering. (C) Sketch of the ellipsometric measurement scheme with the laser incident from the bottom of a water-fluid interface contained in a cylindrical cell sample. (D) Sketch of the nanoparticle ellipsometric model: R is the NP radius, h is the distance between the NP's center and the interface (h<0 in the sketch), see the text for details.

For optically thin interfacial layers (whose thickness << λ_0), the perturbation theory[25] describes r_P/r_S as the sum of $r_{P,0}/r_{S,0}$ for the ideal step-like profile between the two bulk media and an additional term accounting for the first order deviation parameter J_1,:

$$\frac{r_P}{r_S} = \frac{r_{P,0}}{r_{S,0}} - \frac{2iQ_1}{r_{S,0}(Q_1+Q_2)^2}\frac{K_1}{n_1^2 n_2^2} J_1, \tag{3.2}$$

where $Q_1 = 2\pi/(n_1\lambda_0)\cos\varphi$, $Q_2 = 2\pi/(n_2\lambda_0)\cos\varphi_2$ (φ_2=arcsin ($n_1 \sin\varphi/ n_2$)), and $K_1 = 2\pi n_1/\lambda_0 \sin\varphi$. For locally isotropic interfacial refractive index, J_1 is described as:

$$J_1 = \int_{-\infty}^{+\infty} \frac{(\varepsilon(z)-\varepsilon_1)(\varepsilon_2-\varepsilon(z))}{\varepsilon(z)} dz, \tag{3.3}$$

where $\varepsilon_i = n_i^2$ and z is the axis normal to the interface (see Fig. 3.1(D)). In the limit of thin optical layers, ellipsometry data can be fitted with a single parameter (J_1). Note that when the perturbation theory holds, tanΨ is always minimum and Δ = 90° or 270° at the Brewster angle φ_B = arctan (n_2/n_1).

For optically thick layers, the perturbation theory is no longer valid and Eq. 3.2 cannot describe multiple angle of incidence ellipsometric data. Recently, Hunter et al.[16] and Zang et al.[17] introduced a model able to fit data obtained for optically thick interfacial layers bearing NPs at the liquid-gas interface. Using the Maxwell-Garnett effective medium approximation, the interfacial profile of the dielectric constant $\varepsilon(z)$ is described as composed by a first layer accounting for the portion of NPs immersed in the first medium (e.g. water) and a second layer accounting for the portion of the NPs

immersed in the second medium (e.g. oil or air). The model is schematically depicted in Fig. 3.1(D). Knowing media dielectric constant ε_i and the particle radius R (which can be measured independently), the free parameters of the model are (i) h, the distance between the center of particles and the interface and (ii) ϕ, the surface coverage (i.e. area fraction) described as:

$$\phi = \mathrm{N}\ \pi R^2 / A, \tag{3.4}$$

where N is the number of particles in the interfacial region. Hence, the particle contact angle can be calculated as $\Theta = \arccos(-h/R)$. In the model, the thickness of the first layer is $R-h$ and the one of the second layer is $R+h$. The dielectric constants of these two layers are calculated as below:

$$\varepsilon_{L,1} = \varepsilon_1 \frac{\varepsilon_1(2-2f_{NP,1})+\varepsilon_{NP}(1+2f_{NP,1})}{\varepsilon_1(2+f_{NP,1})+\varepsilon_{NP}(1-f_{NP,1})}, \tag{3.5}$$

$$\varepsilon_{L,2} = \varepsilon_2 \frac{(2-2f_{NP,2})+\varepsilon_{NP}(1+2f_{NP,2})}{\varepsilon_2(2+f_{NP,2})+\varepsilon_{NP}(1-f_{NP,2})}, \tag{3.6}$$

where ε_1 and ε_2 are the dielectric constants of the first medium (i.e. water) and the second medium (i.e. oil or air), respectively, $\varepsilon_{NP} = n_{NP}^2$ is the dielectric constant of NPs, $f_{NP,1}$ and $f_{NP,1}$ are the volume fractions of the portion of the NPs immersed in the layers 1 and 2, respectively:

$$f_{NP,1} = \phi \frac{2/3R^3-(R^2h-h^3/3)}{R^2(R-h)},\ f_{NP,2} = \phi \frac{\frac{2}{3R^3}+(R^2h-h^3/3)}{R^2(R+h)}. \tag{3.7}$$

3.2.4 Macroscopic contact angle measurement

Gold substrates were immersed overnight in 1 mg/ml MEO_2MA_{90}-co-$OEGMA_{10}$ polymer solution, and then washed with water and dried under nitrogen gas stream. The contact angle was measured using the sessile method and captive bubble technique. Analysis was performed with an in-house software program. For sessile drop method, 2 µL liquid was perpendicularly dropped onto polymer coated gold substrate. The contact angles, measured through the liquid phase, were captured and recorded by a progressive scan CCD camera (Dataphysics OCAH200). Static, advancing and receding contact angles (α_S, α_A and α_R, respectively) were measured by the captive bubble method, in a quartz cell filled with water or electrolyte solution (0.1 M NaCl or 0.1 M NaOH). A clean stainless steel needle was used to produce an air bubble or a drop of toluene of approximately 2 mm in diameter on the surface. The silhouette of the bubble/drop was captured. Advancing and receding contact angles, measured through air or toluene phase, were determined by setting a tangent to the contact line. Five measurements at different locations on each sample were made. All measurements were performed at least three times.

From advancing and receding angles, equilibrium contact angles have been calculated in the framework of a model that incorporates the contact line dissipation energy into the Young equation:[26]

$$\alpha_E = \arccos\left(\frac{\Gamma_A\cos\alpha_A+\Gamma_R\cos\alpha_R}{\Gamma_A+\Gamma_R}\right) \tag{3.8}$$

where $\Gamma_A = \left(\frac{\sin^3\alpha_A}{2-3\cos\alpha_A+\cos^3\alpha_A}\right)^{1/3}$, $\Gamma_R = \left(\frac{\sin^3\alpha_R}{2-3\cos\alpha_R+\cos^3\alpha_R}\right)^{1/3}$.

3.3 Results: contact angles and surface coverage

We started investigating the adsorption of responsive gold nanoparticles at interfaces in the absence of salt in the water phase. Figure 3.2 shows the ellipsometry measurements of water-toluene and water-air interfaces in the absence and presence of NPs in the water phase. Before the NPs are introduced into the water, both water-toluene and water-air interfaces show the expected step-like

change of Δ as a function of the incident angle φ around the Brewster angle, which can be fitted well by the perturbation theory. J_1= 0 ±0.1 nm (see Eq. 3.2 and 3.3) describes well the tiny deviation between the real dielectric constant profile across the interfaces and the abrupt step change between the dielectric constants of bulk phases. Surface roughness due to capillary waves and intrinsic density profile models have been used to explain the ellispometric parameter J_1.[27,28]

When the responsive gold NPs are introduced into the water phase, they are expected to induce a high optical contrast and large change of the interfacial profile of the dielectric constant $\varepsilon(z)$ at water-toluene or water-air interfaces provided the NPs populate the interfaces. Note that the concentration of NPs used was c_{NP} = 1 gL^{-1} corresponding to a volume fraction of 5·10^{-5}, which was sufficiently low for the change of bulk refractive index to be negligible $n_1 = \varepsilon_1^{1/2}$, while sufficiently high to allow full coverage of the interfaces provided the NPs adsorbed to the interfaces. As shown in Figure 3.2, however, the changes of tanΨ and Δ around the Brewster angle is negligible upon addition of responsive gold NPs into water, which remain approximately the same as the interfaces before the NP addition. Water-toluene and water-air interfaces show the same results, indicating negligible adsorption of responsive gold NPs from deionized water onto its surface.

The adsorption scenario completely changed when responsive gold NPs were introduced in salty water phase. Figure 3.3(A) shows different ellipsometric scans measured for water-toluene interfaces and at different time *t* elapsed after addition of responsive gold NPs into water in the presence of NaCl (0.1 M). Comparing to the data shown in Fig. 3.2, not only the slopes of tanΨ and Δ change but, more importantly, the pseudo Brewster angle, defined as the angle where tanΨ is minimum and Δ = 90° or 270°, noticeably shifts with times.

The shift of the pseudo Brewster angle is the sign of the NP adsorption onto the interface. The ellipsometric data hardly change after use of 0.1 M NaOH instead of NaCl in the water phase (Fig. 3.3(B)). Similar changes are also observed for responsive gold NP adsorption onto water-air interfaces in presence of NaCl and NaOH (Fig. 3.4). Note that for both water-toluene and water-air interfaces in the presence of NaCl or NaOH in water (Figs 3.3 and 3.4), tanΨ and Δ change slowly with time upon addition of responsive gold NPs; the kinetics time is of the order of days.

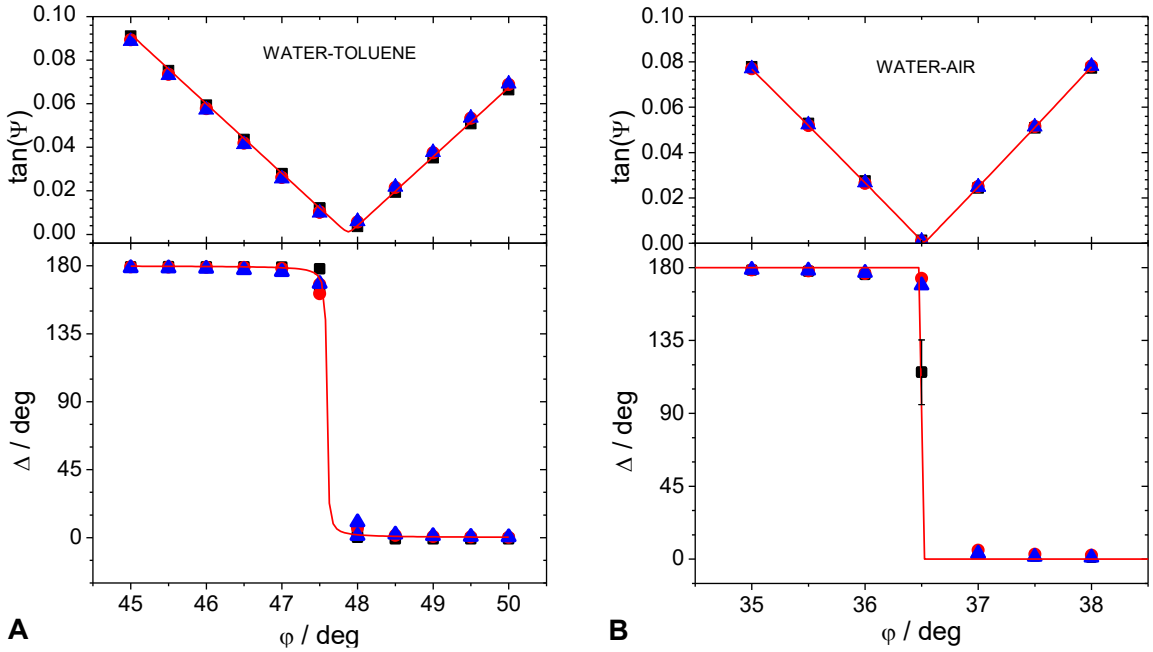

Figure 3.2 Measurements of tanΨ and Δ as a function of the incident angle for water-toluene (A) and water-air (B) interfaces: bare interfaces (■) and aqueous dispersion of responsive gold NPs *c* = 1 gL^{-1} measured at adsorption times *t* = 7200 s (●) and 86400 s (▲). Solid lines represent fits according to the perturbation theory.

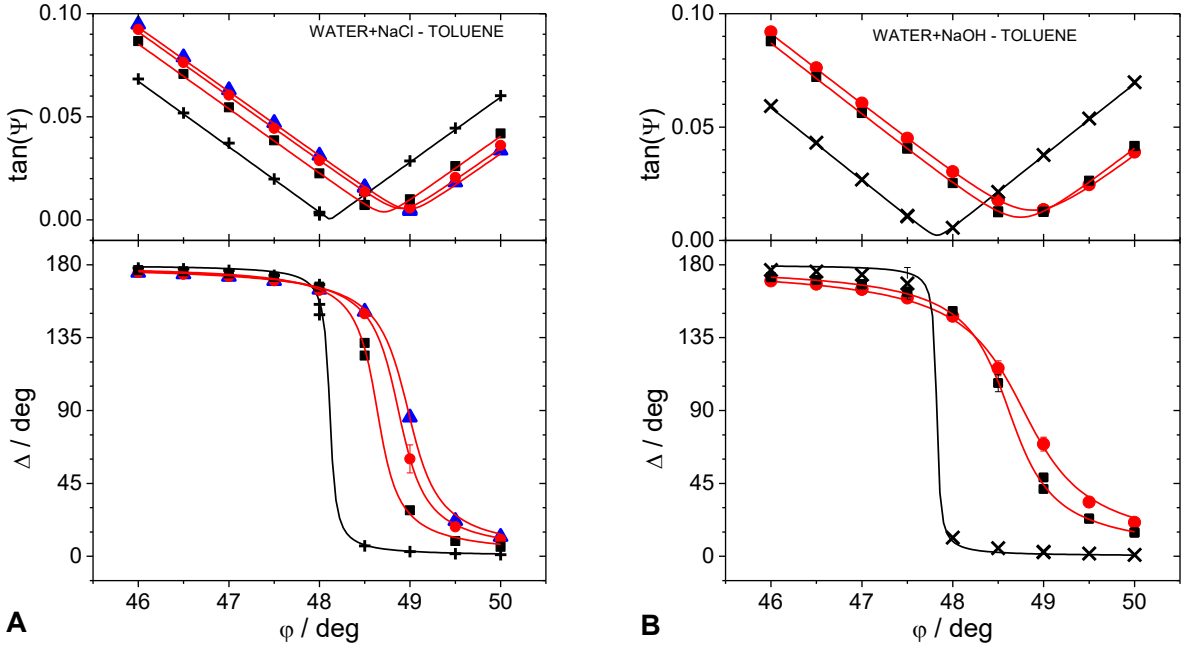

Figure 3.3 Aqueous solution-toluene interface:(A) Ellipsometric scans for 0.1 M NaCl aqueous solution-toluene interfaces before (+) and after the adsorption of responsive gold NPs measured at $t = 10^5$ s (■), 1.8×10^5 s (●) and 4.3×10^5 s (▲). (B) Measurements of tanΨ and Δ as a function of the incident angle for 0.1 M NaOH aqueous solution-toluene interfaces before (X) and after the adsorption of responsive gold NPs measured at $t = 10^5$ s (■) and 6.1×10^5 s (●). Black lines represent fits according to the perturbation theory to the data. Red lines represent fits according to the nanoparticle layer model.

The perturbation theory, valid for optically thin layers, cannot describe the data showing changes of the pseudo Brewster angle (see Eq. 3.2). Here we fitted all data using the model described in the previous section (Eqs. 3.5-3.7). In the present model, we used the dielectric constants of gold nanoparticle, air, toluene from the literature and ε_i of the salty aqueous solutions from the bare interfaces data fitted using the perturbation theory. The polymer shell is not accounted in the model since it matches the dielectric constant of the oil phase; and the optical contrast of the polymer shell in water is negligible with respect to the optical contrast given by gold. Hence, the radii of gold NP cores can be used to represent the radii of whole core-shell NPs, $R = R_1$. Thus, the only two fitting parameters are the surface coverage ϕ and the height h (see Fig. 3.1).

Figure 3.5 shows the evolution of the contact angle $\Theta = \arccos(-h/R)$ and ϕ with the NP adsorption time at water-toluene and water-air interfaces. For NP adsorption at water-toluene interfaces, $\Theta = 91°\pm0.5°$ and ϕ changes between 0.020 and 0.025 when NaCl is present in water. When NaOH in water is used, Θ becomes slightly smaller (90°±0.5°), while ϕ is significantly increased: $\phi = 0.04$ at $t = 6\times10^5$s.

For NP adsorption at water-air interfaces, as shown in Figure 3.5, $\Theta = 67°\pm4°$ when NaCl is water and $\Theta = 21°\pm12°$ when NaOH is in water at $t = 6\times10^5$ s. The surface coverage in both cases increases systematically from 0.024 to 0.055 with the NP adsorption time (t).

For comparison, the macroscopic contact angles (α_S, α_A and α_R) were measured on planar gold substrates, coated with the brushes of random co-polymers of MEO2MA and OEGMA, which was implemented in the same way as the polymers were coated on gold NPs. Table 1 lists the macroscopic angles and equilibrium contact angles α_E calculated form advancing and receding angles (see Eq. 3.8).[26] At the water-toluene interfaces $\alpha_E = 93°$ and it decreases slightly in presence of 0.1 M of NaCl ($\alpha_E = 92°$) or NaOH ($\alpha_E = 87°$). For aqueous-air interfaces, no significant changes were observed when water is replaced by 0.1 M NaCl or NaOH solutions and $\alpha_E = 53°$.

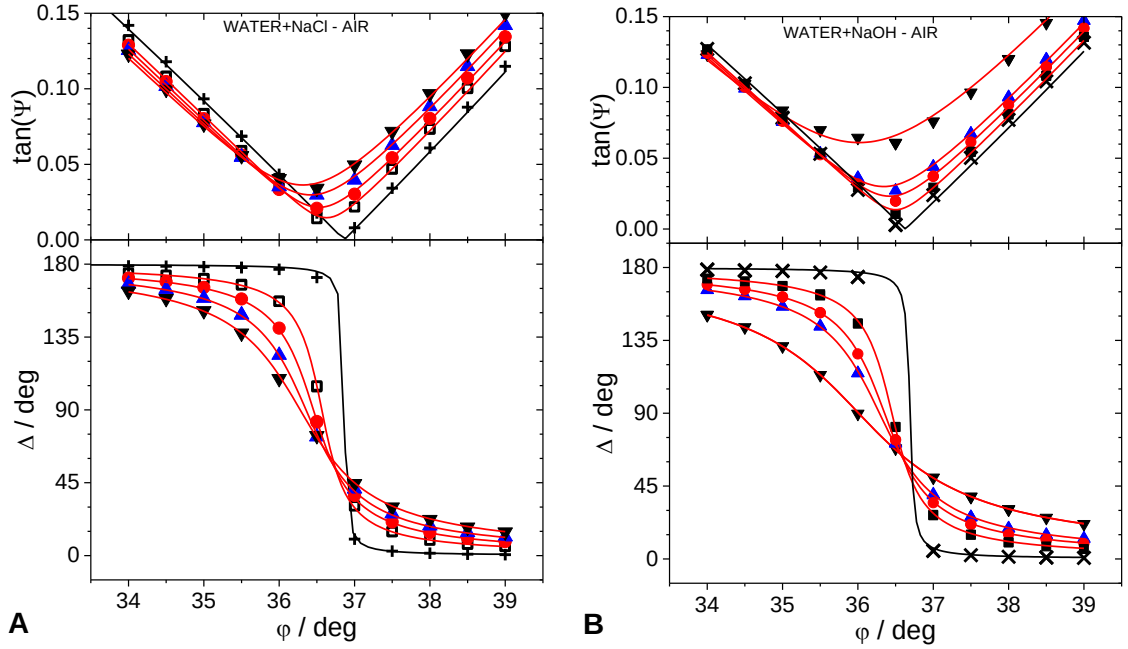

Figure 3.4 Aqueous solution-air interface:(A) Measurements of tanΨ and Δ as a function of the incident angle for 0.1 M NaCl aqueous solution-toluene interfaces before (+) and after the adsorption of responsive gold NPs measured at $t = 0.9\times10^5$ s (■), 1.8×10^5 s (●), 2.6×10^5 s (▲) and 6×10^5 s (▼). (B) Measurements of tanΨ and Δ as a function of the incident angle for 0.1 M NaOH aqueous solution-toluene interfaces before (X) and after the adsorption of responsive gold NPs measured at $t = 0.9\times10^5$ s (■), 1.8×10^5 s (●), 2.6×10^5 s (▲) and 6×10^5 s (▼).Black lines represent fits of the perturbation theory to the data. Red lines represent fits of the nanoparticle ellipsometric model to the data.

3.4 Discussion

3.4.1 Adsorption kinetics

One of the main results of this experimental work is the effect of NaCl and NaOH on NP adsorption. Here, we clearly show that responsive gold NPs do not accumulate and attach onto the pure water interfaces, being the ellipsometric measurements shown in Fig. 3.2 almost identical before and after the addition of NPs into water.

A potential adsorption barrier as the double layer electrostatic repulsion exists close to interface on the water side, which hinder the NP adsorption.[29] The screening of this repulsion is achieved by adding ionic species close to the interface. From this viewpoint, NaCl, NaOH or other salts[30] might lead to the same screening and consequently to NP adsorption. Moreover equilibrium or pseudo-equilibrium contact angles and surface coverages can be measured only at $t > 1$ day, and the kinetic of adsorption is very slow when compared to the predicted adsorption under diffusion control:[31]

$$\phi = 2\pi R^2 c_n \sqrt{D_t t/\pi}\,, \tag{3.9}$$

(where c_n is the number of particles per unit volume and D_t is the particle translational diffusion coefficient) i.e. a surface coverage $\phi = 0.1$ should be reached at t^*=10 s.[31] Note that for the surface coverage measured at the water-air and water-toluene interfaces, a diffusion model with an adjusted diffusion $D_t^* = 3\ 10^{-6}\ D_{t,b}$ (where $D_{t,b}$ is the bulk diffusion coefficient) compares well with the experimental results (see Fig. 3.5).

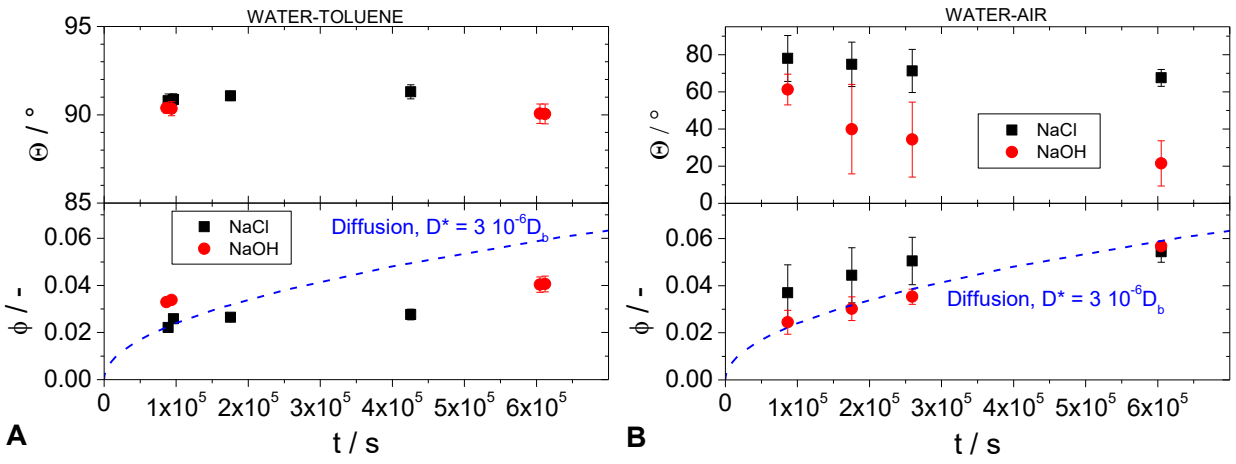

Figure 3.5 Contact angle Θ and surface coverage ϕ as a function of adsorption time for aqueous-toluene (A) and aqueous-air (B) interfaces in presence of 0.1 M NaCl (■) and NaOH (●) obtained from the fits of the nanoparticle ellipsometric model to the data.

Table 3.1 Macroscopic static (α_S) advancing (α_A) receding (α_R) and equilibrium (α_E)[26] contact angle measurements on Au@MEOMA90-co-OEGMA10 model wafer (captive bubble/drop method). For comparison, contact angle Θ measurements by ellipsometry in the long time limit are also shown.

	water in air	0.1 M NaCl in air	0.1 M NaOH in air	water in toluene	0.1 M NaCl in toluene	0.1 M NaOH in toluene
α_S	61.8±0.8	62.6±0.7	59.3±1.2	105.3±0.3	104.4±0.3	107.2±2.5
α_A	66.6±1.3	64.4±0.8	66.6±0.7	108.9±0.7	108.3±0.9	109.0±0.5
α_R	40.7±0.6	40.6±0.7	40.3±1.8	81.0±1.4	78.8±1.8	72.0±1.5
α_E	53.3±0.9	**52.2±0.7**	**53.1±1.2**	93.0±1.1	**91.5±1.4**	**87.4±1.0**
Θ		**67.5±4.6**	**21.5±12.2**		**91.3±0.4**	**90.0±0.6**

Hence, the severe slowing down of the diffusion may be linked to an adsorption barrier E_a in an Arrhenius type equation for diffusion:[32]

$$D_t^* = D_{t,b}\exp(-E_a/k_BT), \tag{3.10}$$

which leads to an adsorption barrier E_a = 12.7 k_BT. This energy barrier agrees with typical values calculated for NPs at the fluid interface accounting for electrostatic double layer repulsion interactions.[19,33]

3.4.2 Free energy

Now we can turn our attention to the free energy of NPs at the fluid interface. For all interfaces, ϕ are much lower than the fully packed value of $\phi = \pi R_1^2 / (4\times R_1^2\sin(60°))$ = 0.907, calculated for hexagonally packed nanoparticles in contact by the inner cores; or the value of $\phi = \pi R_1^2 / (4\times R_2^2\sin(60°)) = 0.404$, calculated for hexagonally packed nanoparticles in contact by the outer polymer shells (see Fig. 3.6(A)). Assuming a hexagonal lattice NP conformation at the interface, an average distance between particles at the interface can be estimated as $l = \sqrt{\pi R_1^2/(\phi\sin(60°))}$, which is 124 nm ($l - 2R_2$ = 96 nm) for ϕ = 0.020 and 75 nm ($l - 2R_2$ = 47 nm) for ϕ = 0.055. One might discuss such l values as due to long range repulsive interactions acting between adsorbed NPs.[34] However,

ellipsometry does not distinguish between different NP arrangements in the interfacial plane. Thus, we cannot discuss further what kind of structures NPs form in the interfacial plane.

In any case, the reported ϕ (Fig. 3.5) could seem very small since one knows that particles are usually irreversibly adsorbed at the interface since desorption wetting energies ΔE_w are very high:[35]

$$-\Delta E_w = \pi R^2 \gamma (1 \pm \cos\Theta)^2, \quad (3.11)$$

where γ is the interfacial tension, i.e. $\gamma = 35$ mN m^{-1} and 72 mN m^{-1} for water-toluene and water-air respectively. Plugging the experimental contact angle Θ values (Table 3.1) in the latter formula, for NaOH solution-air interface $\Delta E_w = -21\ k_BT$, for NaCl solution-air is $\Delta E_w = -1776\ k_BT$; and for aqueous solution-toluene is about $\Delta E_w = -2326\ k_BT$. Given that $|\Delta E_w| >> k_BT$, particles should populate the interface at high ϕ values.

Here, it is worth noting that in the calculations of ΔE_w only the macroscopic wetting cost to remove a single particle from the interface to the bulk is evaluated and would be relevant for particles adsorbing from ideal suspensions onto ideal interfacial layers. In real systems, the adsorption equilibrium also depends on interparticle interactions, and the low surface coverage experimentally observed suggests strong repulsions between particles at interface.

Taking a different perspective, we could be tempted to discuss whether the surface coverages in the long time limit (plotted in Fig. 3.5) correspond to equilibrium concentration c_S of an interphase, defined in a volume of thickness equal to the particle's diameter $2R_1$, $c_s = N\frac{4}{3}\pi R_1^3/(A\ 2R_1) = 2/3\phi$. In this *microscopic* description, the interfacial concentration is determined by the chemical potential equilibrium between bulk and the interfacial region, regarded as a real (inter)phase.[36]

Hence, we could write a partition coefficient between the interphase and bulk as $K_c = c_S/c_{NP} = \exp[-\Delta E/k_BT]$, where ΔE is the difference in free energy between the interphase and the bulk. For aqueous-air interfaces, $\Delta E = -6.6\ k_BT$; for NaOH aqueous-toluene interfaces $\Delta E = -6.3\ k_BT$ and for NaCl aqueous-toluene interfaces $\Delta E = -5.8\ k_BT$ can be calculated. Note that within this approach, a limiting $\Delta E = -9.4\ k_BT$ is estimated for the fully packed value of $\phi = 0.9$.

Now, the deepest energy minima at the interface are calculated for aqueous-air interfaces, on which only adsorption and not transfer (to air) can take place. NPs can cross the interface for NaCl aqueous solution-toluene interfaces, and in these cases the difference in free energy is also the smallest one, which confirms that the energetic states of bulk phases and the interphase are very close and a small thermodynamic change in one of the phase could lead to NP transfer.

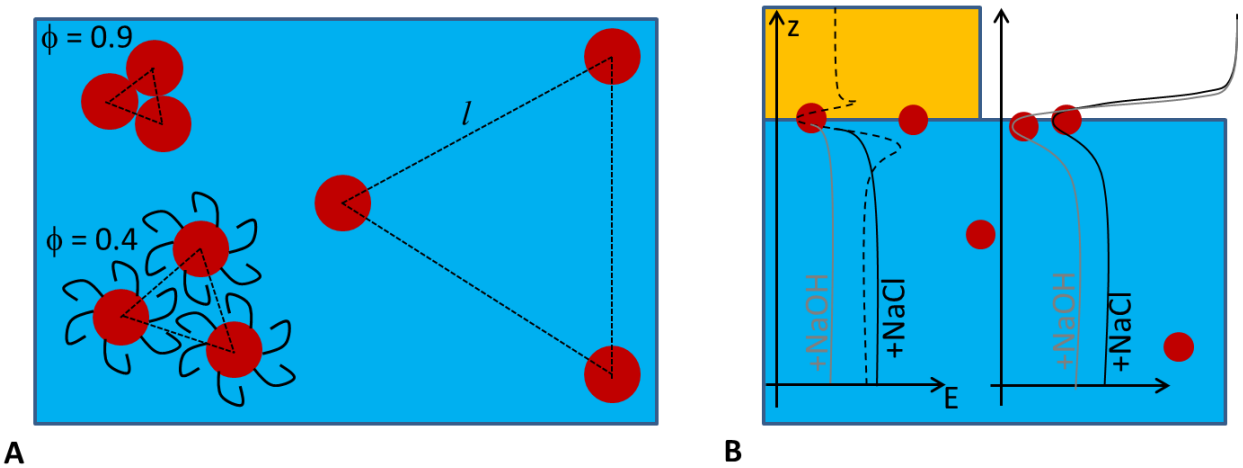

Figure 3.6 (A) NP packing at the water surface for ϕ = 0.9, 0.4 and the general case where the distance between particle's centers is *l*. (B) Interfacial free energy profiles at the aqueous-toluene and aqueous-air interfaces. The dashed profile corresponds to pure water, the grey profiles to NaOH aqueous solution and the solid black profiles to NaCl aqueous solutions.

Recent computer simulations have also shown that the NP energy profile across the interface cannot be described only accounting for wetting energies as in equation 3.11.[35] As a matter of fact, the free energy of core-shell nanoparticles depends strongly on the grafting density and the hydrophobicity of the chemical species composing the particle's shell.[37]

3.4.3 Contact angle

Finally, contact angle measurements (Fig. 3.5 and Table 3.1) can be discussed accounting for wetting and particle-interface interactions. In wetting, the Young equation defines an equilibrium contact angle α_E from the far field equilibrium of the surface forces acting on the triple line, where the solid and the two fluids are in contact.[2] In the vicinity of the triple line, as we go down in length scales, the far field equilibrium does not hold anymore and the local contact angle α_L deviates from the far field angle α_E. At length scales smaller than *ca.* 100 nm, detailed physicochemical properties of the solid and fluids affect the microscopic structure of the contact line; and van der Waals and electrostatic interactions modify the profile of the fluid line and the local contact angle.[2]

Hence in our system, at least two equilibrium contact angles can be defined: a *macroscopic* contact angle that obeys to the Young equation and a *microscopic or local* contact angle that depends strongly on long range surface interactions.

The discussion so far is independent on the geometry of the wetting. Therefore, it applies to the case of a liquid drop on a solid substrate or to the wetting of a solid particle at the fluid interface. In the latter case, however, depending on its size, a solid particle may attain different equilibrium contact angles. The size of the particle is in fact a probing length scale of the wetting phenomenon. For micron-sized particles, the equilibrium contact angle attained by the particle is clearly the *macroscopic* one.[38] Whereas, when the size of the particle is smaller than *ca.* 100 nm, as in our case, one could expect to be in the *microscopic* regime.

In table 1, we compare macroscopic equilibrium contact angles with the ones obtained by ellipsometry in the long time limit. The latter measurements present the advantages of being non-invasive and to probe in situ the interfacial NP optical profile, which accounts for a large number of nanoparticles, and in turn evaluate an averaged *microscopic* or *local* contact angles. The main drawback of the method is that it relies on a model, which describes a monolayer of particles monodisperse both in size and in contact angle.

We start discussing ellipsometric results obtained for aqueous-air interfaces, which show $\Theta = 67° \pm 4°$ for NaCl aqueous solution and $\Theta = 21° \pm 12°$ for NaOH aqueous solution at $t = 6 \times 10^5$ s. Note that for bare interfaces NPs do not adsorb onto the interface and Θ cannot be defined. Whereas for the planar interface, $\alpha_E = 53° \pm 1°$. The remarkable difference between the two contact angles supports the opposite effects of NaCl and NaOH in tuning the interaction of NPs and the aqueous medium. Θ (0.1 M NaCl) > α_E > Θ (0.1 M NaOH) corresponds to a lower affinity of NP for NaCl solution than for NaOH solution. Hence, NaCl promotes a long range attraction between the NP and the interface, which leads to an increase of the *microscopic* or *local* contact angle with respect to the far field equilibrium contact angle α_E. On the contrary NaOH promotes a long range repulsion between the NP and the interface, which leads to a decrease of the *microscopic* or *local* contact angle with respect to the far field equilibrium contact angle α_E.

Those results also agree with our previous investigations showing that NaCl promotes an hydrophobic character of the polymer shell, strongly shifting the lower critical solution temperature of the polymer in water.[19]

NaOH on the contrary not only promotes surface hydration of NPs but also increases the negative charge density at NP surface by deprotonation of the NP surface groups. The latter charge coupled with the expected negative charge of the water-air interface in turn might lead to a repulsion force, which push down to lower angles the NPs adsorbed onto the interface.[3,5]

For aqueous-air interfaces macroscopic equilibrium contact angles α_E (table 3.1) do not show significant difference between NaCl and NaOH solutions, which is in agreement with the fact that in the

far field colloidal interactions are not relevant. The only effect of the nature of the salt is to slightly change the interfacial tensions of the aqueous interfaces.

A fairly good agreement between macroscopic equilibrium contact angles and in-situ contact angles by ellipsometry was found for water-oil interfaces.

For aqueous-toluene interfaces, NP contact angle is almost identical for 0.1 M NaCl and NaOH solutions, even though in the first case NPs cross the interface and transfer to toluene, whereas in the second case stay in the aqueous phase. Comparing to water-gas interfaces, charge effects are expected on both sides of the water-oil interface. Electrostatic and short-range interactions might lead to a steeper energetic landscape on both sides of the interface when compared to liquid-air interfaces and in the simple wetting case. This steep profile could be the reason why the contact angle remains close to 90° for both NaCl and NaOH aqueous-toluene interfaces. A sketch of the energy landscapes for NPs at the fluid interfaces is shown in Fig. 3.6(B).

3.5 Conclusion

We used ellipsometry to measure in-situ the contact angles and surface coverages of nanoparticles at the liquid-liquid and liquid-gas interfaces. Gold nanoparticles adsorb onto the fluid interface only when salt is present in the system, pointing to the existence of a potential barrier close to the interface. In the long time limit, we discussed equilibrium or pseudo equilibrium surface coverages and contact angles under the hypothesis of equilibrium between the bulk phases and the inter(phase). For aqueous-air interfaces, nanoparticle contact angles depends strongly on the nature of the salt, whereas at aqueous-toluene interfaces the in-situ contact angles are almost identical for both NaCl or NaOH solutions. The energy landscape of NPs at the interface is rather complex: wetting, electrostatic and physicochemical properties of water interfaces affect the NP contact angles, which could become different from the macroscopic contact angles measured in a wetting experiment.

These results are particularly relevant for NP phase transfer, and for emulsions and foams stabilized by NPs. Measuring in-situ both the contact angle and the surface coverage is in fact crucial in order to understand and model NP transfer and emulsion/foam stability.

The present method is of particular interest to contribute bridging the long lasting gap between the different scales that are relevant in wetting phenomena. Its advantages rely on measurement over large ensembles of particles, the probing scale of which being defined by the size of the nanoparticles used. In the future, we plan systematic investigations as a function of salt and nanoparticle concentrations in order to elucidate on interfacial interactions and adsorption isotherm of nanoparticle at the fluid interface.

3.6 References

1 B. P. Binks and R. Murakami, *Nat. Mater.*, 2006, **5**, 865–9.
2 P. G. De Gennes, *Rev. Mod. Phys.*, 1985, **57**, 827–863.
3 T. Gehring and T. M. Fischer, *J. Phys. Chem. C*, 2011, **115**, 23677–23681.
4 T. M. Fischer, P. Dhar and P. Heinig, *J. Fluid Mech.*, 2006, **558**, 451.
5 A. Shrestha, K. Bohinc and S. May, *Langmuir*, 2012, **28**, 14301–7.
6 S. Sacanna, W. Kegel and A. Philipse, *Phys. Rev. Lett.*, 2007, **98**, 13–16.
7 A. S. Almusallam and D. S. Sholl, *J. Colloid Interface Sci.*, 2007, **313**, 345–52.
8 A. S. Almusallam, *Phys. Chem. Chem. Phys.*, 2008, **10**, 3099–107.
9 A. Maestro, L. J. Bonales, H. Ritacco, R. G. Rubio and F. Ortega, *Phys. Chem. Chem. Phys.*, 2010, **12**, 14115–20.
10 L. Isa, F. Lucas, R. Wepf and E. Reimhult, *Nat. Commun.*, 2011, **2**, 438.
11 M. Preuss and H. Butt, *J. Colloid Interface Sci.*, 1998, **208**, 468–477.
12 L. Isa, D. C. E. Calzolari, D. Pontoni, T. Gillich, A. Nelson, R. Zirbs, A. Sánchez-Ferrer, R. Mezzenga and E. Reimhult, *Soft Matter*, 2013, **9**, 3789.
13 D. C. E. Calzolari, D. Pontoni, M. Deutsch, H. Reichert and J. Daillant, *Soft Matter*, 2012, **8**,

11478.
14 G. Kaptay, *Colloids Surfaces A Physicochem. Eng. Asp.*, 2003, **230**, 67–80.
15 J. C. H. Wong, E. Tervoort, S. Busato, U. T. Gonzenbach, A. R. Studart, P. Ermanni, J. Ludwig and L. J. Gauckler, *J. Mater. Chem.*, 2009, **19**, 5129.
16 T. N. Hunter, G. J. Jameson and E. J. Wanless, *Aust. J. Chem.*, 2007, **60**, 651.
17 D. Zang, A. Stocco, D. Langevin, B. Wei and B. P. Binks, *Phys. Chem. Chem. Phys.*, 2009, **11**, 9522–9.
18 A. Stocco, T. Mokhtari, G. Haseloff, A. Erbe and R. Sigel, *Phys. Rev. E*, 2011, **83**, 1–11.
19 A. Stocco, M. Chanana, G. Su, P. Cernoch, B. P. Binks and D. Wang, *Angew. Chemie Int. Ed.*, 2012, **51**, 9647–51.
20 E. W. Edwards, M. Chanana, D. Wang and H. Möhwald, *Angew. Chemie*, 2008, **120**, 326–329.
21 R. L. Olmon, B. Slovick, T. W. Johnson, D. Shelton, S.-H. Oh, G. D. Boreman and M. B. Raschke, *Phys. Rev. B*, 2012, **86**, 235147.
22 P. Stoller, V. Jacobsen and V. Sandoghdar, *Opt. Lett.*, 2006, **31**, 2474–2476.
23 W. Haiss, N. T. K. Thanh, J. Aveyard and D. G. Fernig, *Anal. Chem.*, 2007, **79**, 4215–21.
24 R. M. Azzam and N. M. Bashara, *Ellipsometry and polarized light*, North-Holland. sole distributors for the USA and Canada, Elsevier Science Publishing Co., Inc., 1987.
25 J. Lekner, *Theory of Reflection*, 1987.
26 R. Tadmor, *Langmuir*, 2004, **20**, 7659–64.
27 J. Day and C. Bain, *Phys. Rev. E*, 2007, **76**, 41601.
28 A. Stocco and K. Tauer, *Eur. Phys. J. E. Soft Matter*, 2009, **30**, 431–8.
29 M. Oettel and S. Dietrich, *Langmuir*, 2008, **24**, 1425–41.
30 E. W. Edwards, M. Chanana and D. Wang, *J. Phys. Chem. C*, 2008, **112**, 15207–15219.
31 N. Hassan, A. Stocco and A. Abou-Hassan, *J. Phys. Chem. C*, 2015, **119**, 150505105105007.
32 L. Liggieri, F. Ravera and A. Passerone, *Colloids Surfaces A Physicochem. Eng. Asp.*, 1996, **114**, 351–359.
33 L. Xu, G. Han, J. Hu, Y. He, J. Pan, Y. Li and J. Xiang, *Phys. Chem. Chem. Phys.*, 2009, **11**, 6490–7.
34 R. Aveyard, J. H. Clint, D. Nees and V. N. Paunov, *Langmuir*, 2000, 1969–1979.
35 P. Pieranski, *Phys. Rev. Lett.*, 1980, **45**, 569.
36 H. Brenner and L.G. Leal, *J. Colloid Interface Sci.*, 1978, **65**, 191–209.
37 R. J. K. Udayana Ranatunga, R. J. B. Kalescky, C. Chiu and S. O. Nielsen, *J. Phys. Chem. C*, 2010, **114**, 12151–12157.
38 C. Blanc, D. Fedorenko, M. Gross, M. In, M. Abkarian, M. A. Gharbi, J.-B. Fournier, P. Galatola and M. Nobili, *Phys. Rev. Lett.*, 2013, **111**, 58302.

Part 2: Diffusion and Active Motion of Partially Wetted Colloids at the Fluid Interface

The second part of this Habilitation dissertation describes diffusion dynamics of colloidal particles partially wetted and confined at the gas-liquid interface. First, contrary to hydrodynamic predictions, slowing downs of the translational D_t and rotational D_r diffusions of passive colloids at the gas-liquid interface have been observed in dedicated experiments. D_t as a function of the particle contact angle was measured and it decreases if the particle immersion in the liquid decreases. We find that D_t may become even lower than the bulk liquid diffusion for particles mostly exposed to the gas. Janus colloids with two distinguishable faces have been investigated to measure in-plane and out-of-plane rotational diffusions D_r at the fluid interface. To explain the slowing downs of D_t and D_r, a new form of friction due to contact line fluctuations is introduced in Chapter 4.

Keeping the same gas-liquid interface confinement, the following chapter deals with the active motion of self-propelled Janus colloids. Self-propelled particles are active (out of equilibrium) systems able to move autonomously overcoming the length scale of thermal (equilibrium) Brownian motion. If the particle size is in the colloidal domain, persistent active motion and random Brownian motion act together, and Brownian rotational diffusion, D_r, plays a pivotal role in the active motion realization. Indeed, D_r sets the persistence time of the ballistic self-propelled motion, which appear as a long range random walk if a long enough observation time is allowed. Accounting for the slowing down of the diffusions described in the previous chapter, chapter 5 describes the impact of partial wetting dynamics and gas-liquid confinement effects on the dynamics of self-propelled Janus colloids. Enhanced active motion persistence and a coupling between active velocities and Brownian diffusions were experimentally evidenced and discussed.

Chapter 4 is based on the selected publication: “Brownian diffusion of a partially wetted colloid”, G Boniello, C Blanc, D Fedorenko, M Medfai, NB Mbarek, M In, M Gross, A Stocco, M. Nobili, Nature Materials 14 (9), 908-911 (2015)

Chapter 5 is based on the selected publications: “Enhanced active motion of Janus colloids at the water surface”, X Wang, M In, C Blanc, M Nobili, A Stocco*, Soft Matter 11 (37), 7376-7384 (2015) and “Janus colloids actively rotating on the surface of water”, X Wang, M In, C Blanc, A Würger, M Nobili, A Stocco*, Langmuir, 33 (48), 13766–13773 (2017)

Chapter 4

Brownian Diffusion of Bare and Janus Colloids at the Gas-Liquid Interface

4.1 Introduction

Dynamics of colloidal particles at interfaces between two fluids plays a central role in surface microrheology, encapsulation, emulsification, biofilm formation, water remediation and the interface-driven assembly of materials. In absence of any external field or perturbation, microparticles and nanoparticles partially wetted at the fluid interface cannot generally diffuse across the interface. These particles are irreversibly adsorbed onto the interface if the free energy landscapes across the interface shows minima much deeper than the thermal agitation energy k_BT. Hence, fluid interfaces act as a soft confinement for the particle dynamics allowing translational motion in the interfacial plane and rotational dynamics.

So far, hydrodynamic models,[1,2,3] accounting for the particle immersion, predict that translational and rotational dynamics are governed by the viscosities of the fluids. For the translational motion of a particle at a fluid interface, the viscous friction felt by the particle at the interface is predicted to be lower than that observed in the more viscous fluid. These predictions[1,2] however fail to describe a number of experimental observations, showing an unexpected high drag and consequently a slowing down of the translational diffusion at the fluid interface.[4,5,6,7]

In this chapter, we show experimentally that a particle straddling the air-water interface feels large translational and rotational frictions that are unexpectedly greater than that measured in the bulk. We suggest that such a result arises from thermally activated fluctuations of the interface at the solid-air-liquid triple contact line and their coupling to the particle drag via the fluctuation-dissipation theorem. Our findings should inform approaches for surface microrheology, self-assembly of particles at the interface, and help to understand the motion of micron- and nano- artificial or living systems in fluid confinement.

4.2 Hydrodynamic frictions of a solid sphere at the gas-liquid interface

In the following two sections, we review hydrodynamic models describing viscous dissipations for an isolated spherical particle at the fluid interface. The liquid-gas interface is considered and the gas viscosity is consider negligible with respect to the liquid one. In the following two sections, the fluid interface is assumed to remain flat in the presence of the adsorbed particle with an immobile (not moving or fluctuating) three phase contact line. Inertia, advection and non-equilibrium effects are not accounted in these models, which describe particle motion in low Reynolds number hydrodynamics.

4.2.1 Translational hydrodynamic friction of a solid sphere at the gas-liquid interface

Few models on the translational friction felt by a spherical particle at the fluid interface can be found in the literature.[1,2,3] Fischer et al. numerically calculated the hydrodynamic friction on a spherical particle close to and at the interface between two fluid phases in presence or in absence of a monolayer or membrane. They reported the effect of the particle immersion or contact angle α and the effect of the monolayer surface viscosity η_s on translational and rotational hydrodynamic frictions. Colloidal

particles exert forces on both the bulk fluids and the interface. These forces lead to mechanical responses of both the fluids and the interface in the form of three- and two-dimensional flow and pressure fields acting back onto the particle. In their analysis, Fischer et al. considered the interface as a viscous incompressible monolayer. This assumption was made to account for both the viscous responses of the interface and Marangoni stresses, which are generated by gradients in surfactant surface density in the monolayer. This assumption also holds in the limit of very dilute surface density and can be used to interpret experiments on bare fluid interface. Bare interfaces correspond in fact to the zero limit of Boussinesq numbers B_0:

$$B_0 = \frac{\eta_s}{(\eta_1+\eta_2)R}, \tag{4.1}$$

where η_1 and η_2 are the fluid bulk viscosities and R is the sphere radius. For liquid-gas interfaces, the effect of gas viscosity η_2 can be neglected since $\eta_2 << \eta_1$.Translational friction coefficient for the motion of a sphere parallel to the interface $\zeta_{t,H}$ was calculated as:

$$\zeta_{t,H} = k_t \eta_1 R, \text{ where } k_t = k_t^{(0)} + B_0 k_t^{(1)} + \mathcal{O}(B_0^2). \tag{4.2}$$

Hence, considering a partially wetted spherical particle possessing a contact angle α at the bare gas-liquid interface ($B_0 = 0$), the translational friction is simply $\zeta_{t,H} = k_t^{(0)} \eta_1 R$, with:[2]

$$k_t^{(0)} \approx 6\pi\sqrt{\tanh[32(1+\cos\alpha)/(9\pi^2)]}\,. \tag{4.3}$$

Note that $\zeta_{t,H}$ is always lower than the bulk Stokes friction $\zeta_{t,b} = 6\pi\eta_1 R$. It starts at $\zeta_{t,H}$ =0.786 $\zeta_{t,b}$ if $\alpha = 0$ and decreases monotonically towards zero if α approaches 180°. In Fischer et al., as a consequence of the no-slip condition and the incompressibility of the interface, the rotational friction coefficient $\zeta_{r,\perp}$ connected to sphere rolling is infinite when the particle is adsorbed at the interface. Hence in this analysis, the sphere cannot roll at the interface and no coupling exists between translational and rotational motion for $0 < \alpha < 180°$.

4.2.2 Rotational hydrodynamic frictions of a solid sphere at the gas-liquid interface

For spherical particle straddling a fluid interface, one can distinguish two rotational friction coefficients: $\zeta_{r,||}$ describing the rotation about an axis parallel to the interface normal (related to the particle spinning, see later Fig. 4.4(B)), and $\zeta_{r,\perp}$ describing the rotation about an axis perpendicular to the interface normal (related to the particle rolling, see later Fig. 4.4(A)). The latter coefficient $\zeta_{r,\perp}$ is related to the hydrodynamic dissipation described in the partial wetting of sessile drops on solid substrates. In fact, both for particle and drop dynamics the contact line has to move, which corresponds to a relative movement between a liquid and a solid. Note that upon a rotation, a dry region of the solid particle will be wetted and another region (at the opposite side) will undergo dewetting. Both for drops and particles, a no-slip condition at the solid-liquid interface would lead to an infinite dissipation.[8] Hence, as in Fischer et al., a solid particle at the interface cannot rotate about an axis in the interfacial plane in truly no-slip conditions! However, as in the partial wetting dynamics of drops on solid surface, a slip length or a molecular cut-off can be introduced to account for a large but finite dissipation.

Even for bare spherical particles, very few models on the rotational motion at the interface can be found in the literature. O'Neill and coworkers calculated the rotational and translational frictions for the special geometry of a bare spherical particle half-immersed in a liquid, i.e. contact angle $\alpha = 90°$.[9] The rotational friction coefficient $\zeta_{r,\perp}$ depends on a non-dimensional sliding friction coefficient $B = R/b$, where b is the slip length.[9] The case $B = \infty$ corresponds to the no-slip condition, whereas $B = 0$ corresponds to the perfect slip condition. $\zeta_{r,\perp}$ is given by:[9]

$$\zeta_{r,\perp} = k_\perp^r \eta R^3, \tag{4.4}$$

where η is the liquid viscosity. The expression of the friction factor $k_{\perp}^{r}$ is rather complex. It changes from zero in the perfect slip condition to infinity in the no-slip condition. The following empirical formula describes the asymptotic behavior for $B > 1$:

$$k_{\perp}^{r} = 4.5\ln B + 2.5 \, . \tag{4.5}$$

Note that in the bulk, the rotational friction coefficient is $\zeta_{r,b} = 8\pi\eta R^3$, and $k_b^r = 8\pi$. For a typical value of the slip length b = 1 nm (0.1 nm),[10,11] R = 1 μm, B = 1000 (10000) and $k_{\perp}^{r}$ = 33.6 (43.9), which is 34% (75%) higher than the bulk value. Hence, for a spherical particle R = 1 μm half-immersed in water ($\eta \approx 10^{-3}$ Pa.s), a rotational diffusion time $\tau_{r,\perp} = \zeta_{r,\perp}/k_BT$ = 8.4 s (11.0 s) is predicted. Note that $\tau_{r,\perp}$ is only slightly higher than the bulk value $\tau_{r,b}$ = 6.3 s.

The calculation of the rotational friction coefficient $\zeta_{r,||}$ is simpler than $\zeta_{r,\perp}$ given that no contact line motion is involved. For an half immersed (α =90°) spherical particle, $\zeta_{r,||}$ is always the half of the bulk value. As before, $\zeta_{r,||} = k_{||}^{r}\eta R^3$, where the friction factor $k_{\parallel}^{r}$ is:

$$k_{\parallel}^{r} = 4\pi[1/(1 + 3b/R)]. \tag{4.6}$$

In perfect no-slip condition, $\zeta_{r,||} = 4\pi\eta R^3$; and $\zeta_{r,||} = 0$ in slip condition.

4.3 Materials and methods

4.3.1 Colloidal particles

Three particle systems have been used: (i) bare colloidal particles, (ii) fluorescent platinum-melamine resin (Pt-MF) Janus colloids, and (iii) platinum-silica (Pt-SiO_2) Janus colloids (which are non fluorescent).

(i) Silica particles with R = 1 μm and 2 μm were purchased from Bangs Laboratories, Inc.. They are washed in a sulfochromic mixture and thoroughly cleaned with 5 centrifugation/cleaning cycles: after a centrifugation (4000 rpm for 5 minutes) the supernatant is replaced by deionized water and the particles redispersed in ultrasonic bath. In order to change their wettability a solution of DMOAP (N,N-Dimethyl-N-octadecyl-3-aminopropyltrimethoxysilyl chloride), 0.1-5% wt. in demineralized water and methyl alcohol (10%-90%) is used. The particles are added into the silane solution (approximately 0.5 mL of particles in water per 1 mL of silane solution). The solution is then mixed with a vortex mixer during a variable time: particles left for 1 minute in silane solution give a contact angle α = 68°; particles left from 30 to 120 minutes give α = 95°-120°. Solvents and exceeding silane molecules are removed by 10 centrifugation/cleaning cycles. The resulting contact angle ranges from α = 30° (pure silica particle washed with sulfochromic mixture) to α = 120°. Higher contact angles (up to α = 140°) are achieved by using a different deposition process. The particles are first treated following the same procedure as for obtaining α = 120° contact angles and then dried in oven at 120 °C for 2 hours. They are then deposited on the air/water interface directly dried. Polystyrene particles (PS) R = 1 μm are amidine and sulfate functionalized latex spheres, purchased from Invitrogen. Poly (methyl methacrylate) particles (PMMA) R = 3.5 μm are purchased from Fluka Sigma-Aldrich. Before use, they are washed by 3-5 centrifugation/ cleaning cycles (4000 rpm for 10-15 min).

(ii) Janus Pt-MF colloids were fabricated starting from melamine resin MF particles R = 1 μm (Microparticles GmbH, Germany).

(iii) Pt-SiO_2 were fabricated starting from silica particles R = 1 μm (Microparticles GmbH, Germany). Both Pt-MF and Pt-SiO_2 Janus colloids were obtained following the procedure by Love et al..[12] Additional details about the fabrication protocols will be given in Chapter 5, section 5.4.1. Briefly, platinum was sputtered on a particle monolayer. First 10 nm of titanium and then 20 nm platinum were deposited. By 30 minutes' sonication, Pt coated particles were freed into Millipore water. These Pt-MF and Pt-SiO_2 Janus colloids were then cleaned and collected by centrifugation/dilution cycles using Millipore water.

4.3.2 Sample preparation

We use a small cylindrical container of 10 mm in diameter, glued on a microscope glass slide. During particle tracking experiments, the container is covered by a thin flat piece of borosilicate glass, in order to avoid contamination of the interface and water evaporation. Such a cover is not used during interferometric measurements, when a direct optical contact between the light beam and the sample is needed. Deionized water partially fills up to 0.8 mm in height the container. Smaller quantities do not allow to fill homogeneously the container and to obtain a flat interface. Larger quantities of water cannot be used in order to minimize convective flow in the sample.

All glass containers are carefully washed with a sulfochromic mixture and then thoroughly rinsed with water before use. The particles, dispersed in water, are sprayed on the interface by an airbrush, to avoid any possible surface contaminations. Very dilute surface concentrations (about 0.01% area fraction) are used to rule out any possible interaction between colloids. The air-water surface tension is measured by Wilhelmy plate method at a free interface, with and without particles in larger containers. Both the measurements are in agreement with the literature value of the air-water surface tension. All measurements are performed at room temperature (T = 22 °C)

4.3.1 Particle tracking, image analysis and particle contact angle

Bright field and fluorescence optical microscopy were used for particle tracking and imaging. Tracking of isolated particles was achieved by using a Basler Scout CCD camera equipped Leica inverted microscope mounted on a Melles Griot optical table and a Leica objective of magnification ×32.We used also an up-right optical microscope mounted on an anti-vibration table and equipped with a Nikon Mirau X25 objective allowing both bright field and interferometry microscopy. Usually, images were recorded at a rate of 30 frames per second. The tracking was performed under Labview (National Instruments) using an image correlation-based approach (‘‘Stat Tracker St. Andrews’’) to obtain the particle position over time [time t (s), x (μm), y (μm)]. Using IDL software, we treated raw image sequences and by inputting a threshold on the grayscale level we detected the Pt-cap of Janus particles. Counting the number of elements in pixel, the area of Pt-cap detected could be evaluated.

Contact angles of individual particles were measured in situ by Vertical Scanning Interferometry (VSI) using an objective nanopositioner (Nano-F, MCL).[13] The measurements allow to access directly to the protrusion height h of the particles in air. For spheres of known radius R the contact angle is obtained from $\cos\alpha = 1 - h/R$. Corresponding errors comes from both the vertical resolution of the measurement Δh = 20 nm and from the uncertainty on the particles radius $\Delta R \approx 0.1R$. The latter gives the main contribution to the total error. The error ranges from $\Delta\alpha = \pm 2.7°$ at $\alpha = 30°$ to $\Delta\alpha = \pm 19.3°$ for $\alpha = 145°$.

In the case of silica particles the contact angle variation is also checked by the Gel trapping technique.[14] A Phytagel (Sigma-Aldrich) solution at 2% wt. in Millipore water is prepared by heating at 90°C and mixing by magnetic stirrer. The solution is cooled to room temperature to allow the gel to set. Silica spherical particles are spread on the gel surface and then the system is heated again at 90°C in order to trap the particles at the interface. A filtered solution of PDMS, 10% wt. in Millipore water, was poured over the gelled water with the particles trapped at the interface and left at room temperature for 48 h. After cooling, Norland Optical Adhesive 81 (NOA81) is poured over the gelled water with the particles trapped at the interface and photopolymerized by ultraviolet light in 2 minutes. The polymerized NOA81 is peeled off the gel surface. The particles at a complementary position with respect to the air-water interface are then observed by Scanning Electron Microscopy (SEM).

4.4 Results: Colloid diffusions at the interface

4.4.1 Translation diffusion of bare and Janus colloids at the gas-liquid interface

Particles made with different materials (silica, polystyrene, PMMA, Janus Pt-MF and Janus Pt-SiO_2) dispersed in water are sprayed on the interface of a water film with an airbrush to avoid any possible surface contaminants. Spherical particles sit at a position that satisfies the local equilibrium of

the triple (gas-liquid-particle) contact line, corresponding to a contact angle α between the particle tangent and the horizontal plane. For silica particles, in order to change the immersion in water we control α from hydrophilic (α=30°) to hydrophobic (α=145°) tuning the grafting density of hydrophobic silane agents and the deposition process.

Fig 4.1(a) and (b) show SEM pictures corresponding to (gel-trapped) bare colloidal particles with contact angles at the air-water interface of $\alpha \approx 30°$ and 90°. In Fig. 4.1(c) and (d), SEM images of Pt-MF Janus colloids showing $\alpha = 65° \pm 6°$ and Pt-SiO_2 Janus colloids possessing $\alpha = 64 \pm 2°$ at the air-water interface are also shown. It is important to note that, given the size of the silane agents and the protocol used, bare particles have smooth surfaces with negligible roughness. Janus colloids instead show surface roughness of about 10 nm, which is comparable with the coated layer thickness. For Janus particles, we also noted that the morphology of the coated layer is more homogenous for silica than MF, probably due a better metal adhesion on silica than MF.

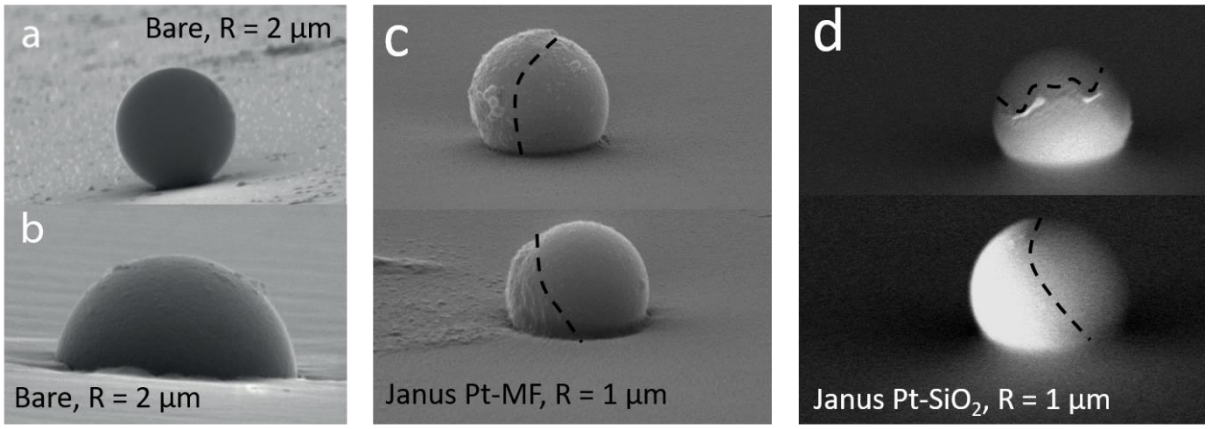

Figure 4.1 Particles trapped in a polymer layer at the complementary contact angle position with respect to the air-water interface (a) SEM images of bare silica particles, with a contact angle at the air-water interface of $\alpha \approx$ 30° and (b) $\alpha \approx$ 90°. (c) SEM images of Pt-MF Janus particles, with contact angle at the air-water interface of $\alpha \approx$ 65°. (d) SEM images of gel trapped Pt-SiO_2 Janus particles, with contact angle at the air-water interface of $\alpha \approx$ 64°. Dashed lines indicate the Janus boundaries.

Motion of individual particles at the liquid-gas interface and in the bulk is followed by optical microscopy. From tracking methods, we obtain data sets consisting of a particle's center-of-mass position and calculate the mean square displacement (*MSD*). *MSD* for particles of R = 2 µm with different immersion depths at the air-water interface are shown in Fig. 4.2(A). Surprisingly, the more hydrophobic particle, having its larger part in the low viscosity medium (air), shows a diffusion coefficient lower than that of the hydrophilic particle and even lower than the one measured in bulk water. $D_t(\alpha$=138°) = 0.0743 ± 0.0026 µm^2.s^{-1}, which is nearly half of the one measured for hydrophilic particle $D_t(\alpha$=30°) = 0.1358 ± 0.0033 µm^2.s^{-1}, more immersed in the high viscosity medium (water). Note that the diffusion of the hydrophobic particle is even slower than the one measured in the bulk (water) ($D_{t,b}$ = 0.1095 ± 0.0065 µm^2.s^{-1}). These unexpected results motivate a complete study of the diffusion at the interface in the full range of accessible contact angles.

Translational diffusion coefficients measured at the interface and in bulk, respectively, are related to the friction coefficients by: $D_t = k_BT/\zeta_t$ and $D_{t,b} = k_BT/\zeta_{t,b}$. The ratio between the measured translational diffusion at the interface and in the bulk is plotted versus the bare colloid static contact angle α in Fig. 4.2(B). The ratio $D_t/D_{t,b}$ decreases if α increases, i.e. when the particle is less immersed in water. Note that the hydrodynamic prediction can describe only the experiments at α = 30°. If α increases, $D_t/D_{t,b}$ is expected to increase while our experiments show a clear decrease, see Fig. 4.2(B).

Contamination by silane dissolution from the hydrophobic particle surface onto the interface as a possible cause of the measured increased viscosity is ruled out: the ratio $D_t/ D_{t,b}$ of the two sets of particles respectively at α = 28° and 90° sharing the same interface shows identical behavior, see Fig. 4.2(B).

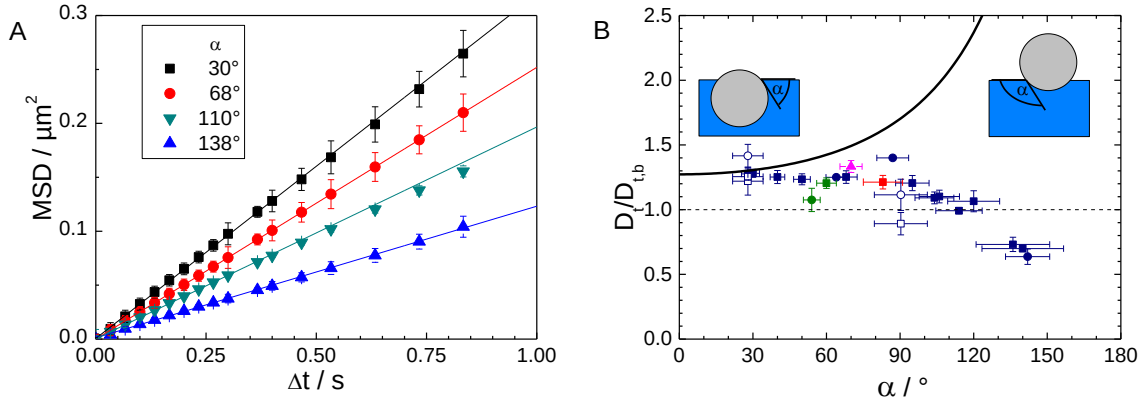

Figure 4.2 (A) Mean squared displacement (*MSD*) as a function of the delay time of $R = 2$ µm bare colloids at the air-water interface for different contact angle. Solid lines represent best fits of $MSD = 4\ D_t\Delta t$. (B) Ratio of the interfacial translation diffusion and the bulk value $D_{t,b}$ as a function of the colloid contact angle. Different radii are examined: 1 µm (circle), 2 µm (square) and 3.5 µm (triangle). At the air-water interface, we consider silica (blue points), polystyrene (green points) and PMMA colloids (magenta point). Open points correspond to couples of silica beads sharing the same interface; the red point corresponds to silica beads at an air-hexanol interface. All points reported represent average values on a set of 5–10 particles. The solid line is the hydrodynamic prediction by Fischer et al. Insets show the contact angle defined by the particle immersion.

Moreover, the surface tension measured with and without particles, $\gamma = 71 \pm 1$ mN/m, agrees with the expected value for an uncontaminated air-water interface. In order to test the robustness of such results and to devise a possible model, we measure under the same conditions different couples of particles and liquids and different particle size of $R = 1$, 2 and 3.5 µm. All such samples follow the same trend observed for silica particles treated with silane at an air-water interface, see Fig. 4.2(B).

We also measured D_t for fluorescent Pt-MF Janus colloids at the air-water interface ($\alpha = 65° \pm 6°$ by gel trapping). By image analysis we could distinguish the two faces of the Janus particle, and evaluate the center of mass of the visible Pt face together with the center of the whole particle. The distance between these two centers was called lever arm L and it is gives information on the particle orientation, see Fig. 4.3(B) inset. *MSD* as a function of lag time and the ratio $D_t/D_{t,b}$ as a function of L/R are plotted in Fig. 4.3(A) and (B) respectively. No clear trend can be observed for the translational diffusion with L/R and $0.4 < D_t/D_{t,b} < 1.4$, see Fig. 4.3(B).

For Pt-SiO_2 Janus colloids at the air-water interface ($\alpha = 64 \pm 2°$ by gel trapping), $0.8 < D_t/D_{t,b} < 1.2$ was also measured (not shown).

All these experimental results are contrary to purely hydrodynamic models describing particle diffusion at fluid interface. In fact, current theories exploring particle diffusion at low capillary numbers and taking into account the Marangoni effect all fail to account for our experimental results (see solid lines in Fig. 4.2).[1,2,3] Additional hydrodynamic effects such as wedge flow[15] close to the contact line and the coupling between translational and rotational particle motion would both promote an increase of the translational diffusion coefficient versus the contact angle and therefore cannot account for its measured enhancement.

4.4.2 Rotational diffusion of Janus colloids at the gas-liquid interface

To measure the rotational diffusion of spherical particles, we used Janus particles with two distinguishable faces. If the Janus boundary crosses the fluid interface (see Fig. 4.1(c) and (d)), particle orientation angles β and φ can be evaluated and rotational diffusions can be measured, see Fig. 4.4(A) and (B).

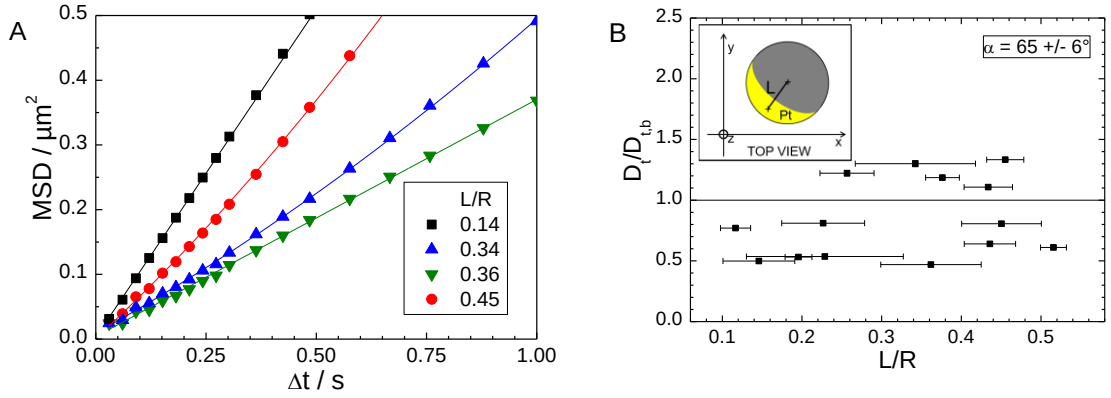

Figure 4.3 (A) Mean squared displacement (*MSD*) as a function of the lag time of fluorescent R = 1 µm Pt-MF Janus colloids at the air-water interface for different ratios of the lever arm L and the radius R. Solid lines represent best fits of $MSD = 4\,D_t\Delta t$. (B) Ratio of the interfacial translation diffusion and the bulk value $D_{t,b}$ as a function of L/R.

By analyzing the images taken during the tracking of the Brownian motion of Pt-SiO_2 Janus colloids at a planar air-water interface, we were able to evaluate the changes of the absolute area of the platinum face observed by optical microscopy. Hence, we evaluate the orientation angle β from the absolute area of the platinum face, and calculated the mean square angular displacement $MSAD(\beta)$. In Fig. 4.4 (C), we plotted $MSAD(\beta)$ as a function of the lag time for three specific dataset for which $40° < \beta < 90°$. We fitted the *MSAD* data by:

$$MSAD(\beta) = MSAD_0 + 2D_{r,\perp}\Delta t, \tag{4.7}$$

where the $MSAD_0$ accounts for the noise introduced by the image treatment. From the fits in Fig. 4.4, we find that rotational diffusion times $\tau_{r,\perp}=1/D_{r,\perp}$ = 87 s (triangle), 152 s (circle), and 547 s (square) are larger by one order of magnitude or more than the hydrodynamic prediction (eqs. 4.4 and 4.5), $\tau_{r,\perp} = \zeta_{r,\perp}/k_BT$ = 8.4 s if b = 1 nm (11 s if b = 0.1 nm), see section 4.2.2. Note that applying equations 4.4 and 4.5 to the experimental results leads to unphysical slip lengths $b << 0.1$ nm ($b<10^{-30}$ nm !).

In order to describe these results, we assume $\zeta_{r,\perp}$ for b = 1 nm, and associated an Arrhenius form to the rotational diffusion $D_{r,\perp}$:

$$D_{r,\perp} = \frac{k_BT}{\zeta_{r,\perp}}\exp\left(-\frac{|\Delta E_\beta|}{k_BT}\right), \tag{4.8}$$

where ΔE_β is the activation energy that is required for a change of orientation β. Averaging on all *MSAD* data, we found $\Delta E_\beta = 3.6 \pm 0.9\ k_BT$.

Now we turn our attention to the in-plane rotational diffusion $D_{r,\parallel}$, see Fig. 4.4(B). Tracking the motion of fluorescent Pt-MF Janus colloids we were able to calculate the angle φ between the projected Janus axis and the lab frame. φ was evaluated from the orientation of the lever arm L with respect to the laboratory x-y axis in the interfacial plane, see Fig. 4.4 (B). $MSAD(\varphi)$ was calculated for different L/R datasets. In Fig. 4.5(A), $MSAD(\varphi)$ data show several slopes in different lag time intervals. We fitted the data in the short time limit, for $\Delta t < 0.2$ s, by:

$$MSAD(\varphi) = MSAD_0 + 2D_{r,\parallel}\Delta t. \tag{4.9}$$

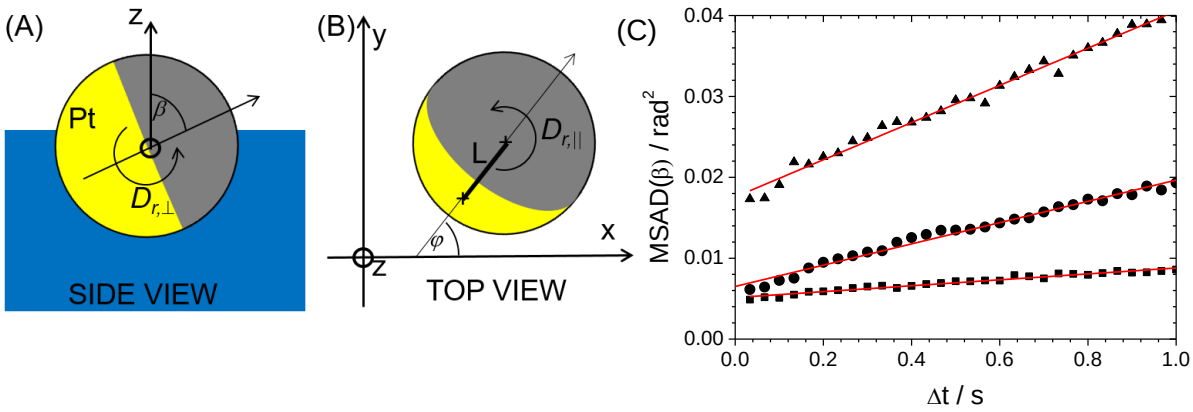

Figure 4.4 (A) Side view sketch of a Janus particle at the gas-liquid interface. (B) Top view sketch of a Janus particle at the gas-liquid interface (C) Mean squared angular displacement (*MSAD*) of the out of plane orientation angle β as a function of the lag time for Pt-SiO_2 Janus colloids at the air-water interface. Solid lines represent best fits of $MSAD(\beta) = MSAD_0 + 2D_{r,\perp}\Delta t$.

From the fits, we plotted $D_{r,\parallel}$ as a function of L/R in Fig. 4.5(B). $D_{r,\parallel}$ for Pt-MF Janus colloids is surprisingly slow. Given the particle contact $\alpha \approx 65°$, $D_{r,\parallel} = k_BT/\zeta_{r,||}$ is expected between $k_BT/(8\pi\eta R^3)$ and $k_BT/(4\pi\eta R^3)$ in no-slip condition; and it should be higher than the latter prediction for positive slip lengths, see equation 4.6. Except for one measurement, $D_{r,\parallel}$ is lower than the prediction and it is even lower than the bulk value. In the long lag time limit, most of *MSAD* data show low slopes or even plateaus, which point to confined dynamics, see inset Fig. 4.5(A). Note that from an hydrodynamic viewpoint no dissipation due contact line motion is expected for a change of orientation φ, if the fluid interface is not moving or fluctuating.

Just for the sake of comparison with $D_{r,\perp}$, $D_{r,\parallel}$ can be written in an Arrhenius form:

$$D_{r,\parallel} = \frac{k_BT}{\zeta_{r,\parallel}} \exp\left(-\frac{|\Delta E_\varphi|}{k_BT}\right), \tag{4.10}$$

where ΔE_φ is the activation energy that is required for a change of orientation φ. For a half immersed particle, $\alpha = 90°$, $\zeta_{r,||} = k_{||}^r \eta R^3 \approx 4\pi\eta R^3$ (if b = 0.1 or 1 nm as before). Given the Janus particle contact angle $\alpha \approx 65°$, we assume that $\zeta_{r,||} = 1.45\ (8\pi\eta R^3)$ in analogy with the contact angle correction in the model of Fischer et al. for the translational motion. Accounting for all *MSAD* data, we find $\Delta E_\varphi = 1.8 \pm 0.9\ k_BT$. The latter value is smaller than ΔE_β, meaning that the slowing down of $D_{r,\parallel}$ is less severe than the one of $D_{r,\perp}$.

4.5 Discussion: Line friction

Our experimental results demand a new theoretical paradigm, beyond hydrodynamics, able to capture the measured dynamics. Considering the relevance of contact line dynamics on the particle breaching of a fluid interface,[16] we focus our attention on the fluctuations at the contact line during particle diffusion.[17] We suggest that thermally activated deformations of the interface at the contact line drive the system out of mechanical equilibrium and give rise to extra random forces on the particle (see Fig. 4.6(A)). Through the fluctuation-dissipation theorem, these fluctuating forces are associated with extra viscous friction on the particle which leads to the measured diffusion slowing down.

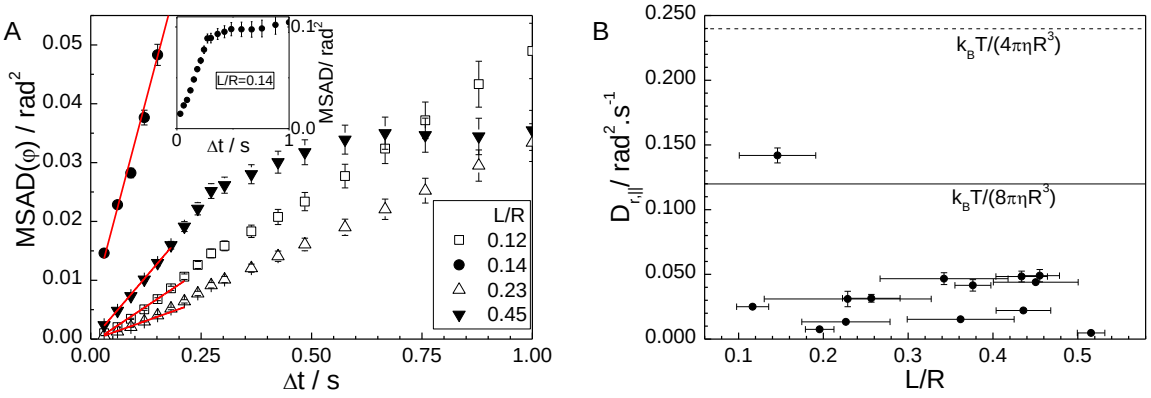

Figure 4.5 (A) Mean squared angular displacement (*MSAD*) of the in plane orientation angle φ as a function of the lag time of fluorescent Pt-MF Janus colloids at the air-water interface for different *L*/*R*. Solid lines represent best fits of $MSAD(\varphi) = MSAD_0 + 2D_{r,||}\Delta t$ for $\Delta t < 0.2$. (B) Interfacial rotational diffusion $D_{r,||}$ as a function of *L*/*R*.

In more detail, any fluid interface deformation that occurs over a contact line segment λ at an angular position Φ with respect to an arbitrary axis *w* in the interface plane (Fig. 4.6(B) and (C)) induces a force on the particle (Fig. 4.6(A)). Such force has a component along *w* given by $F_{L,i}(t) = F_L^0(t)\cos\Phi_i$, where $F_L^0(t) = \gamma\lambda(1-\cos\chi)$, and χ is the angle between the tangents to the fluid interface at the particle and the horizontal, see Fig. 4.6(A) and (B). Summing over the

$$n = 2\pi R\sin\alpha/\lambda \tag{4.11}$$

possible fluctuations along the contact line, we obtain the total random force $F_L(t) = \sum_{i=1}^{n} F_{L,i}(t)$. This random force changes with a characteristic time τ_L, related to the nature of the fluctuations. It has zero mean $< F_L(t) > = 0$ and a non-zero mean square:

$$< F_L(t)^2 >= n < F_{L,i}(t)^2 >= \frac{1}{2}\, n[\gamma\lambda(1-\cos\chi)]^2. \tag{4.12}$$

This fluctuating force $F_L(t)$ adds to the force $F_H(t)$ due to the molecular collisions of the surrounding fluids. Hence, the total random force $F = F_H(t) + F_L(t)$ is related to the friction exerted on the particle via the fluctuation-dissipation theorem $\zeta_t = \frac{1}{2k_BT}\int_{-\infty}^{+\infty} < F(0)F(t) > dt$.

Assuming the uncorrelated nature of each term:

$$< F(0)F(t) >= < F_H(0)F_H(t) > + < F_L(0)F_L(t) > \tag{4.13}$$

and $\zeta_t = \zeta_{t,H} + \zeta_{t,L}$, where $\zeta_{t,H}$ is the hydrodynamic friction and:

$$\zeta_{t,L} = \frac{1}{2k_BT}\int_{-\infty}^{+\infty} < F_L(0)F_L(t) > \, dt \approx \frac{1}{2k_BT} < F_L(0)^2 > \tau_L \tag{4.14}$$

is a line friction coefficient associated with the fluctuations of the contact line.

In Eq. 4.14 we impose that $< F_L(0)F_L(t) >$ goes to zero when $t > \tau_L$. In order to evaluate $\zeta_{t,H}$ we used the model by Fischer et al. (and verified that the other theories give similar values).[1,2,3]

The previous two equations allow us to write $\zeta_{t,L}$ as:

$$\zeta_{t,L} = \frac{1}{4k_BT}\, n[\gamma\lambda(1-\cos\chi)]^2\tau_L = \frac{\pi R\sin\alpha}{2k_BT}\, \lambda[\gamma(1-\cos\chi)]^2\tau_L \tag{4.15}$$

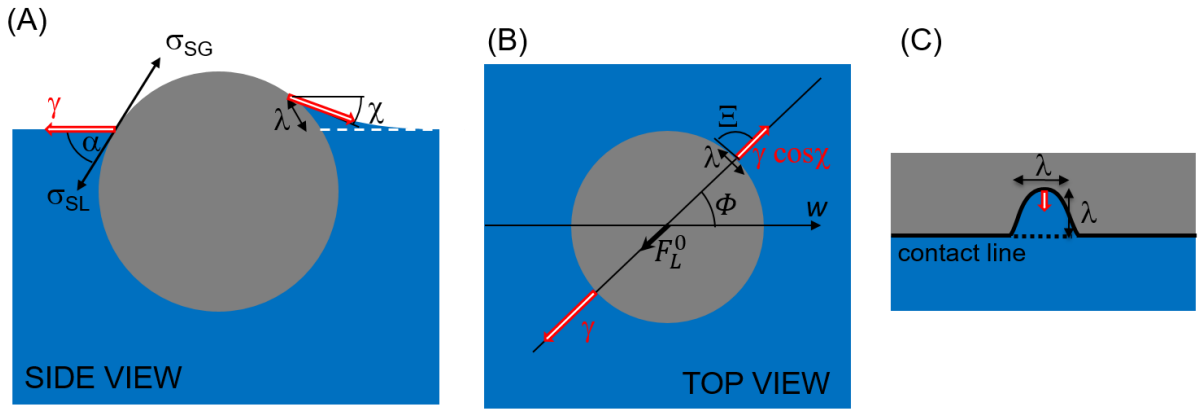

Figure 4.6 (A) Side view sketch of an interface fluctuation at the contact line. On the left side of the particle, interfacial tensions are in equilibrium and α is the equilibrium contact angle defined in Young's equation. On the right side, an interface fluctuation displaces the contact line on the particle over a distance λ and drives the interfacial tensions out of equilibrium. χ is the angle between the tangent to the fluid interface at the particle and the horizontal. (B) Top view of a line deformation, over a segment λ, at the angular position Φ. The imbalance between γ and $\gamma\cos\chi$ leads to a force F_L^0 on the particle. (C) Sketch of a contact line displacement $\lambda\times\lambda$ on the particle surface.

As discussed below, the only free parameter in the model is the length λ. The physical meaning and the values of λ necessary to recover the measured extra dissipation of colloids at the gas-liquid interface can be discussed in the limit of a fluctuating contact line, according to molecular kinetic theory proposed by Blake.[18] The mechanism is reminiscent to the one observed during wetting phenomena of sessile drops on planar surfaces and described in Chapter 2, section 2.5. The contact line is considered constantly moving around its equilibrium position because of thermally activated jumps of water molecules between hydrophilic sites of the particle surface. The line segment size λ corresponds to the mean distance between the sites and thus it also coincides with the contact line displacement (see Fig. 4.6(C)). The correlation time of the fluctuations according to molecular kinetic theory is:[18]

$$\tau_L \cong \frac{\eta v_m}{k_B T}\exp\frac{E_a}{k_B T} = \frac{\eta v_m}{k_B T}\exp\frac{\lambda^2\gamma(1+\cos\alpha)}{k_B T}. \tag{4.16}$$

And the line friction coefficient becomes:

$$\zeta_{t,L} = \frac{\sin\alpha}{2}\,\frac{v_m\lambda[\gamma(1-\cos\chi)]^2}{(k_B T)^2}\exp\frac{\lambda^2\gamma(1+\cos\alpha)}{k_B T}\;\pi\eta R, \tag{4.17}$$

where v_m is the molecular volume of the liquid (v_m = 2.99 10^{-29} m^3 for water) and E_a is the activation energy needed for the line jump. E_a can be written in the form of an adhesion energy $E_a = \lambda^2\gamma(1+\cos\alpha)$.[18]

The deformation angle χ of the interface (Fig. 4.6(A)) can be found solving the cylindrical Laplace equation.[19]

For n >>1, we get:

$$\tan\chi \approx 4\sin\alpha/\pi\ . \tag{4.18}$$

In our range of contact angles, the following inequalities hold, 0.5 <χ/rad< 0.9.

Now we can compare our model to the experiments on translational diffusion of bare and Janus colloids. Comparing our model (eqs. 4.17 and 4.18) with data in Fig. 4.2 for bare colloids, we find $\lambda(\alpha$=60°) = 0.26 ± 0.02 nm, $\lambda(\alpha$=120°) = 0.54 ± 0.04 nm, and $\lambda(\alpha$=140°) = 0.97 ± 0.06 nm. Fitted λ values increases with the colloid contact angle α and they are in the range of physical meaningful values of the molecular kinetic theory propose by Blake.[18] These values can be also compared to the measured spacing between hydrophilic SiOH groups on silica. Note that after hydrophobic surface treatments, an increase of λ is also expected due to the increase in the number of passivated SiOH sites with silane.

Comparing our model with data shown in Fig. 4.3(B) for Pt-MF Janus colloids, we find a range of λ from 0.2 nm to 0.4 nm able to describe the experimental values $0.47 < D_t/D_{t,b} < 1.3$. While for Pt-SiO_2 Janus colloids, we find a range of λ from 0.3 nm to 0.4 nm able to describe $0.8 < D_t/D_{t,b} < 1.2$. Hence, we could rationalize the slowing down of the translational diffusion by accounting for a line friction due to contact line fluctuations described in the molecular kinetic theory of partial wetting dynamics.[18]

After having discussed particle translational diffusion, we now focus our attention on rotational dynamics. For the rotational diffusion $D_{r,\perp}$, we could associate ΔE_β to the energy needed to move the contact line on the particle surface, as one particle region undergoes wetting and an opposite region undergoes dewetting. Given that the Janus particle surface is not perfectly smooth due to the platinum coating and intrinsic nanometric roughness, this energy can be related to the contact line motion and line pinning caused by these topographical surface defects.[20,21]Indeed, $\Delta E_\beta = 3.6 \pm 0.9\ k_BT$ can be compared to the defect energy, *i.e.* the total energy dissipated by a single defect around a hysteresis cycle.[22] Hence, a slowing down of the rotational diffusion $D_{r,\perp}$ can be interpreted also in terms of thermal hopping of the contact line as for colloidal particles adsorbing at the oil-water interface.[21,16]

Finally, we can discuss the in-plane rotational diffusion $D_{r,\parallel}$ results shown in Fig. 4.5. A slowing down of $D_{r,\parallel}$ points to the existence of a line friction for the rotational diffusion. However, the model built before for the translational motion assumed that contact line fluctuations lead to forces directed to the vertical axis passing through the center of the particle (see Fig. 4.6(B) and (C)). Hence in the ideal geometry shown in Fig. 4.6(B) the force acting on the segment λ has no component tangent to the contact line perimeter, and no fluctuating torque could exist and therefore a rotational line friction is not expected.

However, a breaking of the particle spherical symmetry could occur for Janus colloids given the non-negligible thickness and the shape of the Pt coating. In this case, Janus colloids can be regarded as low aspect ratio ellipsoids for which a rotational line friction can be modelled and a slowing down of the rotational diffusion has been experimentally observed.[21] We can also consider a generic scenario for which the contact line fluctuation yields both to a radial force as sketched in Fig. 4.6(B) but also to an azimuthal force component F_Φ that could generate a fluctuating torque parallel to the interface normal.

Following the same approach as for the translational friction, the rotational line friction can be written as:[21]

$$\zeta_{r,L} \approx \frac{1}{2k_BT}\langle M_{L,\parallel}(0)^2\rangle \tau_L, \tag{4.19}$$

where $M_{L,\parallel}$ is the total torque due to contact line fluctuations and $\langle M_{L,\parallel}(t)^2\rangle = n\langle M_{L,i}(t)^2\rangle$, n is given by eq. 4.11 and:

$$M_{L,i}(0) = F_\Phi R\sin\alpha, \tag{4.20}$$

where $F_\Phi = \gamma\lambda\cos\Xi$, and Ξ is an angle which defines the azimuthal force component F_Φ generating a torque parallel to the interface normal. If $\Xi \neq \pi/2$, F_Φ is non zero, see Fig. 4.6(B). Hence, a rotational friction can be written:

$$\zeta_{r,L} = \frac{1}{2k_BT}\pi R^3\sin^3\alpha\gamma^2\lambda\cos^2\Xi\ \tau_L = \frac{\sin^3\alpha}{2}\ \frac{v_m\lambda\gamma^2\cos^2\Xi}{(k_BT)^2}\ \exp\frac{\lambda^2\gamma(1+\cos\alpha)}{k_BT}\pi\eta R^3. \tag{4.21}$$

Note that for $\Xi = \pi/2$ (in the ideal case shown in Fig. 4.6(B)) there is no rotational line friction. Since Ξ cannot be calculated or estimated without making several assumptions, in the following we prefer to discuss only qualitatively equation 4.21. As for the translational friction ($\zeta_{t,L} \sim \pi\eta R$, eq. 4.17), the line rotational friction scales as the Stokes friction, $\zeta_{r,L} \sim \pi\eta R^3$. From the hydrodynamic prediction described in 4.2.2, the prefactor in the rotational friction $\zeta_{r,||}$ is given by eq. 4.6. In eq. 4.21, the prefactor in $\zeta_{r,L}$ is $\frac{\sin^2\alpha}{2}\ \frac{v_m\lambda\gamma^2\cos^2\Xi}{(k_BT)^2}\ \exp\frac{\lambda^2\gamma(1+\cos\alpha)}{k_BT}$, which depends strongly on λ. For typical values of the other parameters in the prefactor and for Ξ very close to $\pi/2$, $\zeta_{r,L}$ could be comparable or even higher than the

hydrodynamic friction coefficient $\zeta_{r,L} > \zeta_{r,||}$. Hence, contact line fluctuations with azimuthal force components F_Φ could be the cause of the slowing down of $D_{r,||}$ shown in Fig. 4.5.

Before concluding this section, it is worth noting that particle surface heterogeneity (roughness or defects) would lead to a range of λ values in our models (eqs. 4.17 and 4.21). For Janus colloids, surface roughness and defects due to the coating fabrication were observed (see Fig. 4.1(c) and (d)). Hence, a distribution of λ values due to particle surface heterogeneity could explain the large distribution observed for the translational and rotational diffusions of Janus particles in Figs. 4.3(B), 4.4(B) and 4.5(B).

4.6 Conclusion

Here we report an experimental characterization of the translational and rotational diffusions of micrometric spherical bare and Janus colloids straddling an air-water interface. Bare silica colloids possessing different static contact angles α were obtained by changing the particle surface chemistry, tuning the density of silane molecules. This surface treatment impacts not only the static contact angle but also the translational particle dynamics. Translational diffusion experiments as a function of the particle immersion depth in water particles show that colloids diffuse more rapidly when they are more immersed in water. Such an intriguing behaviour is discussed in term of additional line friction due thermally activated fluctuations of the fluid interface. Here we discuss that line pinning and the contact line displacement λ over particle surface defects control the strength of the line friction and the slowing down of the translational diffusion.

Using Janus colloids with two distinguishable faces we could also measure rotational dynamics. These Janus colloids show a surface roughness of about 10 nm due to the metal coated layer. Rotational diffusion $D_{r,\perp}$ related to particle rolling at the interface is strongly slowed down by the dynamics of the contact line displacement. We have also observed a slowing down of $D_{r,||}$ related to particle spinning at the interface, which was not expected even accounting for contact line fluctuations for ideal symmetric and spherical particle geometry. Hence, considering a breaking of symmetry due to Janus particle surface heterogeneity, the slowing down of $D_{r,||}$ could be interpreted as a consequence of contact line fluctuations showing azimuthal force components and a resulting rotational line friction.

We believe that our findings will stimulate new theoretical efforts into this problem where viscous, solid friction and interface fluctuations combine to dictate particle dynamics in complex environments.

4.7 References

1 K. D. Danov, R. Dimova and B. Pouligny, *Phys. Fluids*, 2000, **12**, 2711.
2 T. M. Fischer, P. Dhar and P. Heinig, *J. Fluid Mech.*, 2006, **558**, 451.
3 C. Pozrikidis, *J. Fluid Mech.*, 2007, **575**, 333.
4 D. Wang, S. Yordanov, H. M. Paroor, A. Mukhopadhyay, C. Y. Li, H.-J. Butt and K. Koynov, *Small*, 2011, **7**, 3502–7.
5 K. Du, J. A. Liddle and A. J. Berglund, *Langmuir*, 2012, **28**, 9181–8.
6 Y. Lin, A. Böker, H. Skaff, D. Cookson, A. D. Dinsmore, T. Emrick and T. P. Russell, *Langmuir*, 2005, **21**, 191–4.
7 A. Stocco, T. Mokhtari, G. Haseloff, A. Erbe and R. Sigel, *Phys. Rev. E*, 2011, **83**, 1–11.
8 D. Bonn, J. Eggers, J. Indekeu, J. Meunier and E. Rolley, *Rev. Mod. Phys.*, 2009, **81**, 739–805.
9 M. E. O'Neill, K. B. Ranger and H. Brenner, *Phys. Fluids*, 1986, **29**, 913.
10 P. G. De Gennes, *Langmuir*, 2002, **18**, 3413–3414.
11 C. Sendner, D. Horinek, L. Bocquet and R. R. Netz, *Langmuir*, 2009, **25**, 10768–81.
12 J. C. Love, B. D. Gates, D. B. Wolfe, K. E. Paul and G. M. Whitesides, *Nano Lett.*, 2002, **2**, 891–894.
13 C. Blanc, D. Fedorenko, M. Gross, M. In, M. Abkarian, M. A. Gharbi, J.-B. Fournier, P. Galatola and M. Nobili, *Phys. Rev. Lett.*, 2013, **111**, 58302.
14 V. N. Paunov, *Langmuir*, 2003, **19**, 7970–7976.

15 P. G. De Gennes, *Rev. Mod. Phys.*, 1985, **57**, 827–863.
16 D. M. Kaz, R. Mcgorty, M. Mani, M. P. Brenner and V. N. Manoharan, *Nat. Mater.*, 2012, **11**, 138–42.
17 S. Guo, M. Gao, X. Xiong, Y. J. Wang, X. Wang, P. Sheng and P. Tong, *Phys. Rev. Lett.*, 2013, **111**, 26101.
18 T. D. Blake, *J. Colloid Interface Sci.*, 2006, **299**, 1–13.
19 H. Lehle, E. Noruzifar and M. Oettel, *Eur. Phys. J. E*, 2008, **26**, 151–160.
20 S. Ramos and a Tanguy, *Eur. Phys. J. E. Soft Matter*, 2006, **19**, 433–40.
21 G. Boniello, C. Blanc, D. Fedorenko, M. Medfai, N. Ben Mbarek, M. In, M. Gross, A. Stocco and M. Nobili, *Nat. Mater.*, 2015, **14**, 908–11.
22 J.-M. Di Meglio and D. Quéré, *Europhys. Lett.*, 2007, **11**, 163–168.

Chapter 5

Active Motion of Janus Colloids at the Gas-Liquid interface

5.1 Introduction

Janus colloidal particles show remarkable properties in terms of surface activity, self-assembly and wetting. Moreover they can perform autonomous motion if they chemically react with the liquid in which they are immersed or if an external energy source is provided.

Several strategies have been envisioned to bias the autonomous motion of active colloids. External magnetic[1] and electric fields[2] have been exploited to control the motion of different Janus particles. The effects of field gradients have been also investigated theoretically to control directional motion of active colloids emulating the bacteria movement, which is directed by nutrient concentration gradient.[3] Pinchasik *et al.* have also showed how active colloids can use biomimetic principles to move in the vicinity of a water interface and perform two or three dimensional movement depending on the nature of the surface forces.[4]

In all the above mentioned cases, it is worth noting that persistent active motion is coupled with the Brownian diffusion. Similar to run-and-tumble systems, active colloids show a diffusive behavior at large length and time scales, and an effective diffusion coefficient $D_{t,eff}$ can be defined as:[5,6]

$$D_{t,eff} = D_t + V^2/(4D_r), \tag{5.1}$$

where D_t and D_r are respectively the Brownian translational and rotational diffusion coefficients and V is the self-propulsion active velocity. Both the passive component D_t and the active component $V^2/(4D_r)$ of the motion contribute to an overall effective diffusion. Thus, only at relatively high speed V (of the order of some μm/s for micron sized particles in aqueous solution) or at short time an active motion can be distinguished from passive Brownian diffusion.

As far as directional and active transport is concerned, a major challenge consists in obtaining persistent directional trajectories while minimizing random Brownian motion. This target can be achieved either by attaining high V or by reducing D_r (see Equation 5.1).

The slowing down of the rotational diffusion is clearly of primary importance for enhancing directional movements. This is particularly true for active systems whose sizes are in the micron and submicron ranges since D_r scales with the inverse of the cube of the size.[7] Such slowing down could be efficiently achieved by confining the rotational diffusion, while not hindering the directional self-propulsion.

A well-studied example of self-propelled particles is Janus particles half covered by platinum where the active motion is due to catalytic reaction occurring on the platinum region of the colloid, which transforms H_2O_2 in water and oxygen.[6] The active velocity V depends on the H_2O_2 concentration (the fuel of the catalytic engine), the size of the colloid[8], the thickness of the platinum layer[9] and on the reaction and transport phenomena occurring on the particle's surface.[10] In bulk, for particles of about 2 μm diameter, $V \approx 9$ μm/s have been measured for polystyrene-Pt colloids[8] and for silica-Pt colloid V could be as high as 6 μm/s when the catalytic fuel concentration is 5 %.[11]

Roughness,[12] thickness[13,11] and shape[14] of the platinum coating are important parameters which affect strongly not only the active velocity V but can also lead to an active angular velocity ω of the colloid even if the original particle shape was spherical.[15] In a recent paper, Archer et al. succeed to control the rotational propulsion ω of spherical Janus colloids in the bulk.[15] Such Janus colloids were

fabricated by a glancing angle deposition technique.[16] Changing the glancing angle of the platinum metal evaporation leads to asymmetric shapes of the coating with different covered areas. At normal glancing angle ($\Lambda = 90°$) a certain variability $0 < \omega/\text{rad.s}^{-1} < 2$ of the angular velocity was observed in the bulk. By reducing the glancing angle to $\Lambda = 20°$, ω increases up to 18 rad.s^{-1} and the projected trajectories observed were essentially circular. Note that similar circular or spiral trajectories were observed previously for strongly asymmetric particles or for spherical light-adsorbing particles under optical fields.[17,18,19,20,21,22]

Here, we have investigated the effect of a soft but strong confinement given by the irreversible adsorption of the Janus particles at the air–water interface. We show that the slowing down of the degrees of freedom related to the rotational diffusion is an efficient way to enhance the motion persistence of self-propelled Janus colloids. The relevance of particle fabrication and partial wetting dynamics of Janus particles at the air–water interface are also highlighted to understand and control two dimensional active motion in presence of thermal Brownian motion.

5.2 Realizing Janus colloid self-propulsion at the fluid interface

Catalytic Janus colloids attached onto at the water surface may show autonomous motion if a reactant is present in the aqueous phase as fuel. For platinum coated Janus colloids, the fuel is hydrogen peroxide and concentrations of a few percent are enough to show directional trajectories and speeds of 10 μm/s.[23] To realize self-propulsion parallel to the interface plane several requirements have to be fulfilled.

First, the largest contact area between the catalytic surface and the liquid containing the fuel is sought. However, the Janus boundary should not remain parallel to the interface, since no propulsive force can then be generated in a direction parallel to the interfacial plane (see Fig. 5.2). The latter requirement excludes amphiphilic Janus colloids to perform self-propulsion parallel to the interface. In fact, amphiphilic Janus particles prefer exposing the hydrophobic (hydrophilic) phase to the hydrophobic (hydrophilic) fluid phase and setting the Janus boundary parallel to the interface, which correspond to an equilibrium contact angle of 90° if we consider spherical Janus particles composed of two hemispherical faces.[24,25] Janus colloids with two hydrophilic faces instead are able to change orientation between the limiting cases where the Janus boundary touches the air-water interface without increasing its free energy (see Fig. 2.6). Note that when both faces of the Janus colloid possess the same equilibrium contact angle, form a wetting perspective the Janus colloid is equivalent to a bare colloid and all orientation correspond to the same interfacial energy. In the latter system, one could expect an active motion interrupted by a thermal Brownian motion corresponding to the orientations for which the catalytic face is pulled out from the aqueous phase.

In real experimental conditions, surface heterogeneity and roughness of colloidal particles can dramatically impact the translational and rotational diffusions and the free energy landscape at the interface as we have already pointed out in Chapter 2 and 4. Contact line pinning may result in contact angle hysteresis and lead to severe slowing down of the translational and rotational diffusions. Hence metastable orientations of Janus particle could be observed which in turn could lead to colloid self-propulsion parallel to the interface.

5.3 Methods

5.3.1 Contact angle of single Janus colloids

The contact angle of single colloids at the water surface was measured both by an optical microscopy technique, and a gel trapping method using scanning electron microscopy SEM.

The immersion of colloids in water was measured by an in situ method as described by Hórvölgyi *et al.*.[26] Janus colloids suspension in water was placed in between two parallel optical microscopic slides. The space between the two slides was changed between 4 and 100 μm. Some Janus particles attach onto the air-water interface. For observations, the sample cell was laid down under an inverted microscope equipped with an oil-phase objective (magnification ×100).

Another way to measure the particle-water contact angle is to use a gel trapping method.[27] An hydrogel was prepared by heating 2 wt % Phytagel (Sigma-Aldrich) in solution in Millipore water at 90°C under magnetic stirring. After cooling down to room temperature the gel was formed (gel point 27-32°C). Beads suspension in water was spread at the gel surface and the sample heated again at 90°C to let particles be trapped at the interface. Immersion depth of beads at gelled water surface is expected to be similar to the one at liquid water surface since the two interfaces have the same surface tension.

To get a replica of the gel interface with the beads, Norland Optical Adhesive 81 (NOA81) was poured over the gelled water surface and then photopolymerized by ultraviolet light for 2 minutes. The solidified NOA81 layer was peeled off taking particles at complementary positions with respect to that at air-gelled water interface. These samples were finally observed by both optical microscopy and SEM. We evaluated the contact angle α by using the software ImageJ (and the "Contact Angle" plug-in). The accuracy of the method is about 10° in the range of contact angle considered here.

5.3.2 Particle tracking and image analysis

Tracking of isolated particles was achieved by using a Basler Scout CCD camera equipped Leica inverted microscope mounted on a Melles Griot optical table and a Leica objective of different magnifications. Videos were typically recorded at a rate of 30 frames per second. The tracking was performed under Labview (National Instruments) using an image correlation-based approach (''Stat Tracker St. Andrews'') to obtain the particle position over time [time t (s), x (µm), y (µm)]. Using IDL software, we treated raw image sequences and by inputting a threshold on the grayscale level we detected the Pt-cap. Counting the number of elements in pixel, the area of Pt-cap detected could be evaluated.

5.4 Results: Fabrication and wetting

5.4.1 Janus colloid fabrication

Pt-SiO_2 Janus colloids were fabricated following the procedure by Love et al.[28] Silica beads (purchased from Microparticles GmbH, radius R = 1.06 ± 0.03 µm, zeta potential = – 13 mV) were cleaned by centrifugation/dilution cycles using Millipore water. This deionized water was produced by a Millipore Milli-Q filtration system with a resistivity of 18 MΩ·cm.

First, a monolayer of silica beads was prepared on a silicon wafer (diameter 10 cm) by drop-casting: drops of particle suspension at a concentration of 0.1 mg/mL were regularly deposited with a syringe onto a silicon wafer to reach an average coverage of about 10%. Observation of the prepared sample shows that the particles are either isolated or form clusters of 4 to 30 particles (as sketched in Fig. 5.1(A)). This is possibly due to capillary force during the evaporation of residual water.

Using plasma bombarded metal sputtering (ALCATEL SCM 400 system), first 10 nm of titanium and then 20 nm platinum were deposited onto the silica beads monolayer. By 30 minutes' sonication, Pt coated silica beads were freed into Millipore water. These Pt-SiO_2 Janus colloids were then cleaned and collected by centrifugation/dilution cycles using Millipore water.

Scanning electronic microscopy (SEM, FEI Quanta 200F) was used to observe the as-prepared Janus colloids. The sample was prepared by making a drop of Janus colloid suspension onto silica wafer and dried. As shown in Fig. 5.1(B) and (C), the SEM images show that the Pt-coated silica particle has two distinct faces. The white faces of the particles correspond to Pt-coated surfaces. The Janus boundary where the Pt-coated face and the bared silica face meet can be "linear" or "wavy". The wavy Janus boundary result probably from the shadowing effect during the metal deposition procedure.[29] When silica beads are closely packed, as sketched in Fig. 5.1(A), the nearby beads act as shields preventing the deposition of metal atoms.

Looking into the finer details of the Pt-coated face, as shown in Fig. 5.1(D), the Pt layer presents some roughness at a characteristic length scale of about 10 nm. When metal atoms are deposited onto a substrate which is rugged, the atoms do not arrive at the same time uniformly at the surface. This random heterogeneity, which is inherent in the process, may create the surface roughness.

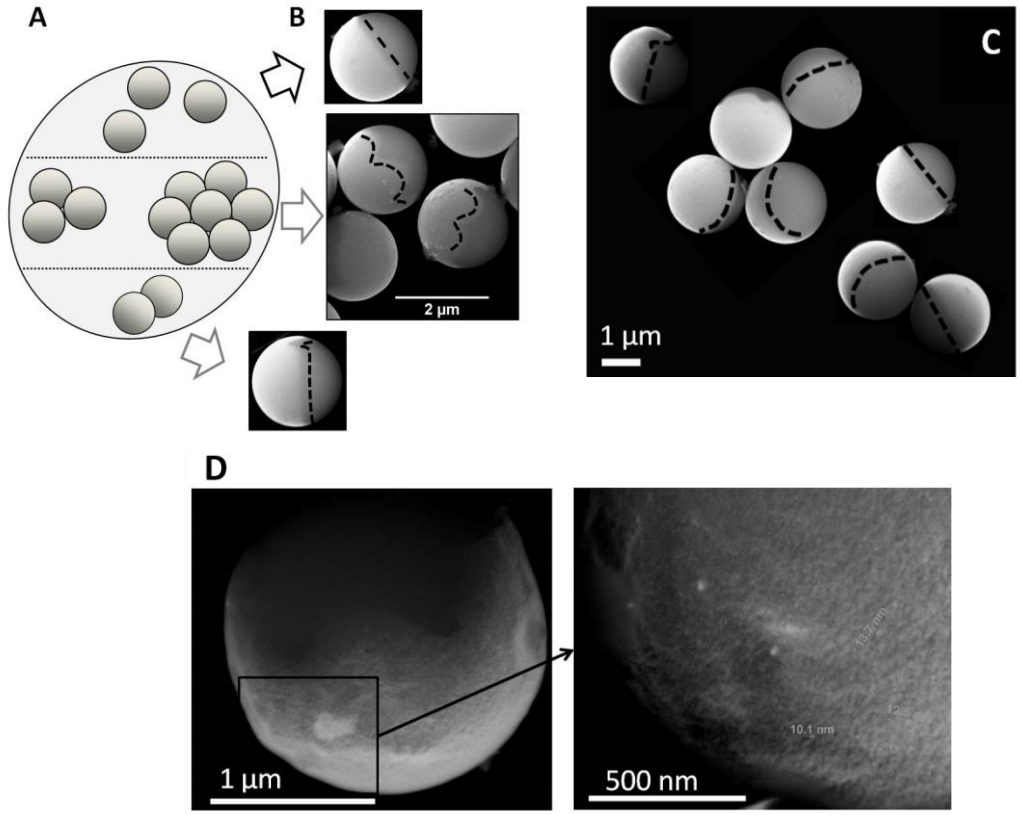

Figure 5.1 (A) Sketch of silica beads monolayer on a silica wafer. (B) and (C) SEM images of Pt-SiO_2 colloids. Dashed lines show the Janus boundaries. (D) SEM images of the Pt-coated surface.

5.4.2 Contact angle and orientation of Janus colloids at the interface

For Janus colloids at the liquid-gas interface, we recall the definition of the contact angle α from the immersion depth of the colloid at the interface; and the orientation angle β defined between the Janus axis (normal to the Janus boundary) and the interface normal, i.e. z-axis, see Fig. 5.2.

Fig. 5.3 shows some images of Janus colloids at the air-water interface obtained by optical microscopy. Janus colloids attached onto the interface from water, where they were originally fully wetted. Hence, during the emersion of the colloid in air the contact line has to recede, and the contact angle measured in Fig. 5.3 can be regarded as the receding contact angle of the Janus colloids (see Fig. 2.7). The average contact angle measured for different Janus colloids is 50° with a standard deviation of 6°.

In Fig. 5.4, SEM images of gel trapped Janus colloids at the interface of solidified NOA81 layer are also shown. Note that the visible part of colloid is the one previously immersed in gelled water. In these measurements, Janus colloids were deposited on top of the gelled water and attached onto the interface from air. In this protocol, the contact line advances on the colloid surface and the contact angle measured in Fig. 5.4 can be considered as the advancing contact angle (see Fig. 2.7) of the Janus colloids, $\alpha_{J,A} = 64 \pm 2°$.[23] From the contact angle results: $\alpha_{J,R} = 50° \pm 6°$ and $\alpha_{J,A} = 64 \pm 2$, we measure a contact angle hysteresis: $\cos\alpha_{J,R} - \cos\alpha_{J,A} = 0.2$, which points to a significant pinning of the contact line on surface defects. Note also that $\alpha_{J,R} = 50° \pm 6°$ and $\alpha_{J,A} = 64 \pm 2°$ can be compared to the contact angle measured for bare silica colloid, $\alpha_{S,colloid} = 61°$, and for platinum coated planar surfaces, $\alpha_{P,surface} = 52°$.[30]

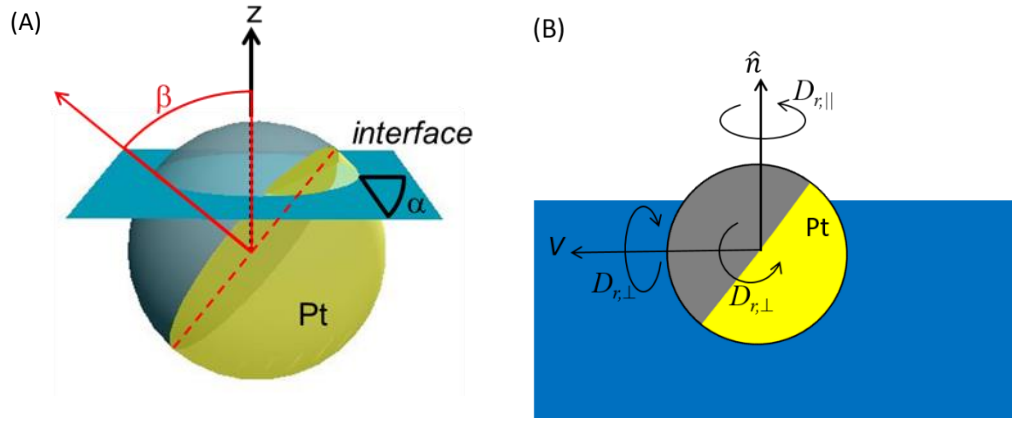

Figure 5.2 (A) Sketch of the contact angle α of the colloid at the air-water interface and the angle β defying the orientation of the Pt cap with respect to the interface. (B) Sketch of a Janus colloid moving parallel to the interface with an active velocity V and owing two rotational diffusion coefficients $D_{r,\|}$ and $D_{r,\perp}$.

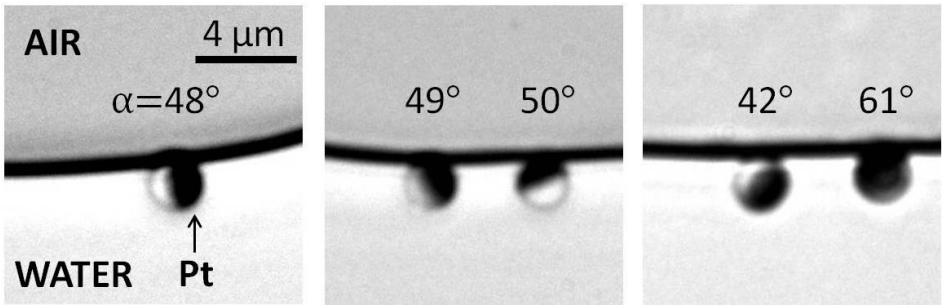

Figure 5.3 Microscopic images of Janus colloids at the air-water interface. The black surfaces of colloids are coated with Pt. Contact angles (α) measured by image analysis are shown.

Both in Fig. 5.3 and 5.4, the orientation β of Janus colloids shows a variety of ranges. Some Janus colloids are straddling the water surface with the air-water interfacial plane across their Janus boundaries. Note that using literature values of the interfacial intensions of silica and platinum one would expect the low energy platinum face to be all wetted by water. Hence, β orientations of the Janus colloids cannot simply be described by the free energy of smooth particle as described in Chapter 2, see Fig. 2.6.[31,32,33]

In order to learn about the possible interfacial orientations, we monitored the orientation of several Janus colloids by the gel trapping procedure and we classified the orientation of Janus particles with respect to the interface.[34] Figure 5.5 displays an optical image together with the distribution of orientation. Three classes of orientation are distinguished: (i) when the Janus boundary is parallel to the air water interface the colloids appear either completely dark, when the Pt face is immersed in water, or completely white when the silica face is immersed in water. When the Janus boundary is not parallel to the interface both black and white domains are clearly distinguished on the particle. Black region of the colloid is the Pt-coated surface. For most of particles, the Pt cap is partially immersed in water. More precisely, 70% out of 250 colloids have the Janus boundaries not parallel to the air-water interfacial plane. For 20% of the particles the Pt face is completely immersed in water ($\beta = 0 \pm 30°$) while only less than 10% of the particle have their silica face completely immersed.

These results point to the existence of metastable particle orientations caused by the contact line pinning (Figs. 5.3, 5.4 and 5.5). Surface defects on which the contact line could pin are clearly observed on the ≈10 nm rough platinum surface (see Fig. 5.1(D)). Note also that we did not find any significant change of the contact angle with the orientation of the Janus colloid or contact line pinning on the wavy Janus boundaries. Thus, contact line pinning affects strongly the interfacial behavior of Janus colloids and results in a contact angle hysteresis and a variety of metastable orientations.

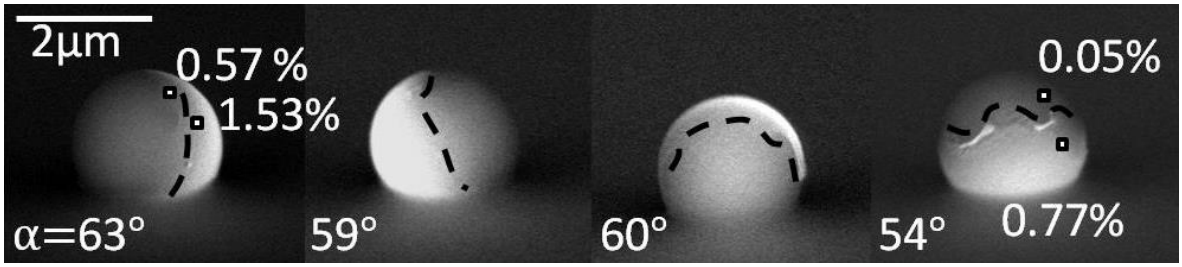

Figure 5.4 SEM images of Pt-SiO_2 beads trapped in the NOA81 layer. Pt atomic percentages are shown for two particles with the white parts corresponding to Pt-coated surfaces.

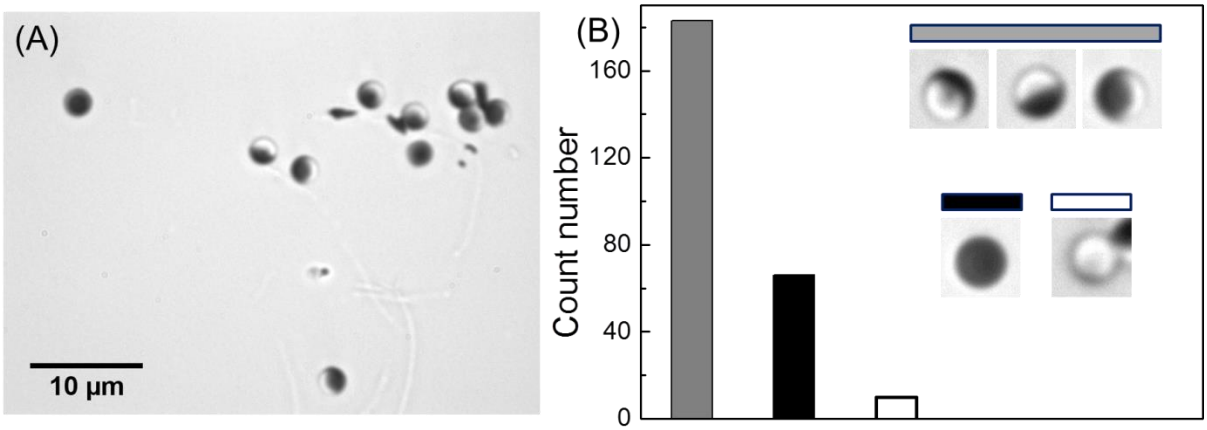

Figure 5.5 (A) Optical microscopy image showing Janus Pt-SiO_2 colloids at interface obtained by a gel trapping method. The visible parts of the particles were in gelled water. Black region represents the Pt-coated surface. (B) Histogram of the particle orientation distribution. The gray, black and white bars represent separately the numbers of particles with Janus boundary rotated out of the interfacial plane (gray), particles with Pt cap immersed in water (black) and particle with Pt-coated surface exposed in air (white).

5.5 Results: Active motion and diffusions

5.5.1 Active trajectories of Janus particles at the air-water interface

In order to investigate the motion of Janus colloids at the surface of water, a water suspension of particles was sprayed onto a bare surface, thus avoiding the use of spreading solvents which might contaminate the interface.[23]

In presence of the H_2O_2 fuel, both active rectilinear-like and circular-like trajectories at the air-water interface were observed (Figs. 5.6 and 5.7). Figure 5.6 displays two dimensional rectilinear-like trajectories for Janus colloids at the water surface under different H_2O_2 fuel concentrations. In the absence of H_2O_2, particles undergo characteristic Brownian motion confining their trajectories in small areas (end-to-end distances of trajectories remain below 4 µm lengths during 20 s). In presence of H_2O_2, directional rectilinear-like displacements in the order of 100 µm have been measured over an observation time of 20 seconds.

Some circular-like trajectories for active Janus colloids at the air-water interface have been observed, see Fig. 5.7. We found that rectilinear-like trajectories represent 72% of the total active trajectories observed; whilst circular-like trajectories correspond to 28%.[35] Circular-like trajectories were also observed in the bulk far from the solid interface of the bottom of the container. Hence, as it will be discussed later, the circular-like particle motion can be safely attributed to the particle fabrication which causes a break of symmetry in the particle geometry.

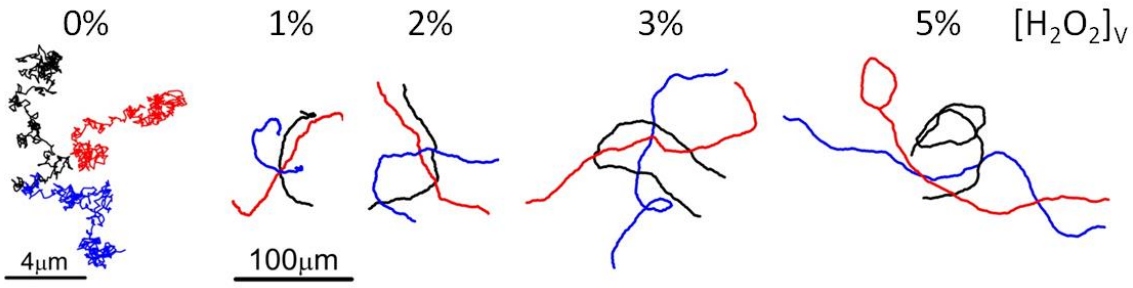

Figure 5.6 Selected rectilinear-like trajectories of Janus particles at the water interface (*xy*–plane) under different fuel concentrations $[H_2O_2]_V$ over 20 seconds. Measurements performed at a field of view of 477 μm × 358 μm.

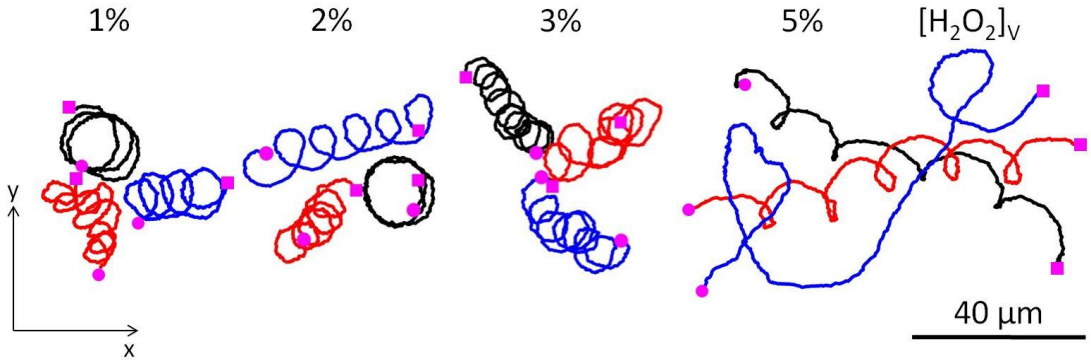

Figure 5.7 (A) Selected circular-like trajectories of Janus particles at the horizontal air-water interface (*x*-*y* plane) under different fuel concentrations ($[H_2O_2]_V$) over 20 seconds. The filled circle represents the beginning of the motion and the filled square is the end.

We attempted to correlate the statistics on the type of active trajectory and the particle fabrication. Hence we scrutinized particle surface defects observed in SEM images. About 40% of the particles show either wavy Janus boundaries or some asymmetric platinum coating (Figure 5.1). However, the correlation between this observation and the 28% observation of circular-like trajectory should be considered only qualitative. It is indeed difficult to establish quantitative criteria on the critical size or shape of the surface defects which would lead to a break of symmetry in the particle geometry and to the observation of circular-like motion.

In the following sections, we will first analyze rectilinear-like active trajectories in order to discuss the persistence of the active motion at the interface (sections 5.5.2 and 5.5.3). Circular-like active trajectories will be described in the following sections in connection with translational and rotational diffusion coefficients and their coupling with the active velocities (sections 5.5.4 and 5.5.5).

5.5.2. Interfacial active velocity of Janus colloids for rectilinear-like trajectories

We used particle tracking videomicroscopy to evaluate the position and the active velocity *V* of the Janus particles at the air-water interface and to learn about Janus particle orientation. By performing image analysis it was indeed possible to obtain information on the position of the platinum coverage during the motion. An example of trajectory of an active colloid moving at the water surface is shown in Figure 5.8. The images below the trajectory (red line) are real images of the Janus particle, which show a darker region which is the coated Pt layer. To enhance the contrast between the two regions, images were binarized using a constant threshold (by implementing a routine in *IDL* software). The resulting images are shown in the insets above the trajectory (Figure 5.8). White color in the binarized images corresponds to the darker part of the colloid in the raw images and it represents the Pt region. The orientation of the Pt layer normal is the same as the moving direction with the Janus particle moving with the platinum segment in the rear. The same observation was done for all beads where the Pt area

could be detected. Hence, it confirms that the motion occurs in the direction opposite to the catalytic site and it demonstrates that the catalytic layer drives the particle to move directionally. Moreover, it rules out that drift due to advection flow is causing the directional motion.

To evaluate the active velocity *V*, we have calculated the mean squared displacement (*MSD*) from the particle position. *MSD* for rectilinear-like trajectories and H_2O_2 concentrations in the range between 0 and 6 v/v % are shown in Figure 5.9(A).

For active colloids in the bulk, the general expression for the two-dimensional projection of the *MSD* reads:[36]

$$MSD = 4D_t\Delta t + \frac{V^2\tau_r^2}{3}\left[\frac{2\Delta t}{\tau_r} + \exp\left(-\frac{2\Delta t}{\tau_r}\right) - 1\right], \tag{5.2}$$

which reduces to :

$$MSD = 4D_t\Delta t + \frac{2}{3}V^2\Delta t^2, \tag{5.3}$$

if the rotational diffusion time $\tau_r = 1/D_r$ is much larger than a given lag time Δt. At the air-water interface, the parameters of the previous equations are different from the bulk values since the colloids are only partially immersed in the bulk liquid.

In Figure 5.9(A), in absence of H_2O_2, the *MSD* is linear with the lag time as expected for random Brownian motion. In the presence of H_2O_2, all *MSD* change quadratically with Δt, as in eq. 5.3, which indicates that rotational diffusion time is much larger than the maximum lag time considered. In this case $\tau_r = 1/D_r$ could not be extracted from our *MSD* results. Note that equation 5.3 leads to very good fits of the experimental data, which provide the active velocity *V* shown in Fig. 5.9(B). *V* increases with the fuel concentration and for $[H_2O_2]_V$ = 6%, the average velocity is ca. 18 μm s^{-1}, which is about twice the velocity measured in the bulk.[23]

We have also determined D_t and found a value very similar to the bulk value $D_{t,b}$, pointing to a slowing down of D_t at the interface given the hydrodynamic prediction $D_t \approx 1.4\ D_{t,b}$ for particle contact angle α between 50° and 64° (see Fig. 4.2(B)).[37]

To check the robustness of our results, we also performed a series of control experiments in order to rule out the effect of drift due to convection.[38] We measured the drift velocities by studying the diffusion of passive silica beads for the same fuel concentrations used for Janus particles. As shown by the filled squares in Figure 5.9(B), velocities around 1 μm s^{-1} have been measured, which are much smaller than the velocities measured in active conditions.

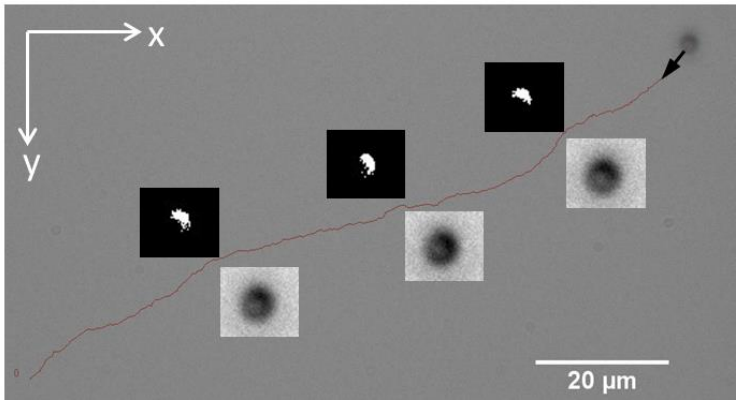

Figure 5.8 Trajectory (red line) of a Janus colloid at 5% $[H_2O_2]_v$ at the water surface. Three pairs of magnified images [raw (below the trajectory) and binarized (above the trajectory)] are inserted from right to left at time 2, 4, 6 seconds respectively. Measurements are performed with a field of view of 125 μm × 94 μm.

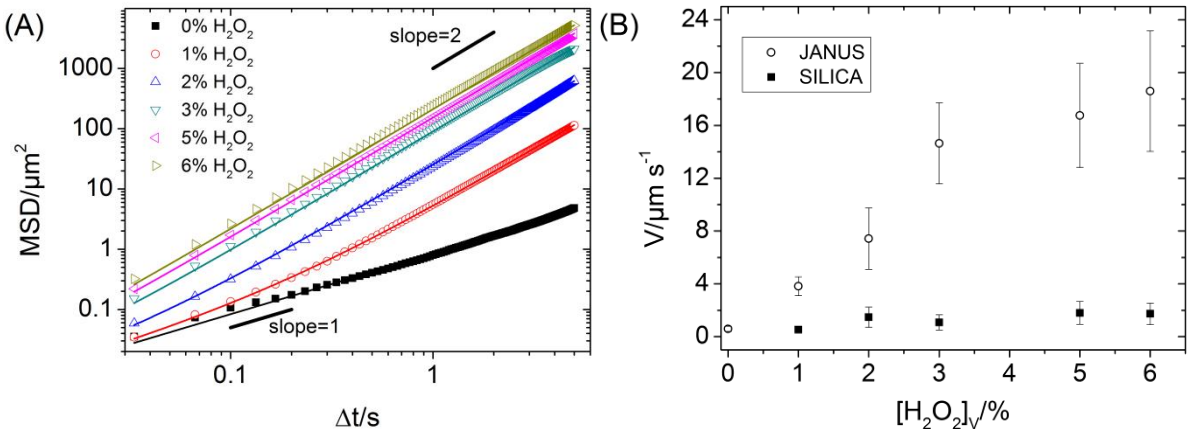

Figure 5.9 (A) Mean squared displacement (*MSD*) as a function of the lag time for different $[H_2O_2]_V$. Solid lines represent best fits of $MSD = 4\,D_t\Delta t + 2/3\,V^2\Delta t^2$. (B) Active velocity V as a function of $[H_2O_2]_V$ for Janus and bare particles.

5.5.3 Interfacial Rotational diffusions for rectilinear-like trajectories

As pointed out before, from the *MSD* analysis we could not gain information on the rotational diffusions of active Janus colloids at the interface. On the other hand, we have observed in Fig. 5.8 that imaging approximately constant thresholded platinum areas points to the expected severe slowing down of rotations about an axis perpendicular to the interface normal and thus a reduced value of $D_{r,\perp}$, see Fig. 5.2(B).[39]

In order to gain some additional insights into the rotational diffusions at the interface, we try to extract information on the motion direction from the particle velocity vector. In particular, changes in the velocity modulus or direction can be observed in the decays of velocity autocorrelation functions. For motion direction changes, the decay is related to the randomization of the direction of the active velocity vector due to the rotational diffusion $D_{r,\parallel}$. Thus, we have calculated the particle discrete velocity $\boldsymbol{v}$, which has two components in the x and y laboratory axis, $v_x(t) = \frac{x(t+\Delta t_1)-x(t)}{\Delta t_1}$ and $v_y(t) = \frac{y(t+\Delta t_1)-y(t)}{\Delta t_1}$ and $\Delta t_1 = 1/30$ s is the lowest time interval dictated by our CCD camera; and modulus $|v| = \sqrt{v_x^2 + v_y^2}$.

Discrete velocity modulus $\langle|v(t+\Delta t)||v(t)|\rangle$ and velocity vector $\langle \boldsymbol{v}(t+\Delta t)\cdot\boldsymbol{v}(t)\rangle = \langle v_x(t+\Delta t)v_x(t)\rangle + \langle v_y(t+\Delta t)v_y(t)\rangle$ autocorrelation functions for rectilinear-like trajectories are shown in Fig. 5.10(A) and (B).

Note that velocity modulus depends on the particle orientation and $\langle|v(t+\Delta t)||v(t)|\rangle$ is intimately connected to the orientation angle β, see Fig. 5.2. Hence, the approximately constant $\langle|v(t+\Delta t)||v(t)|\rangle$ with the lag time indicates that β is not varying significantly during the measurements (see also Fig. 5.8) and confirms the severe slowing down of the out of plane diffusion $D_{r,\perp}$. On the contrary, $\langle \boldsymbol{v}(t+\Delta t)\cdot\boldsymbol{v}(t)\rangle$ show clear decays, which are connected to the change of motion direction at the interface and are related to $D_{r,\parallel}$.

In a purely two dimensional system, for active colloids showing both a propulsion velocity V and an angular velocity modulus ω, the autocorrelation function of the instantaneous velocity $\boldsymbol{v}_i$ reads:[40]

$$\langle \boldsymbol{v}_i(t+\Delta t)\,\boldsymbol{v}_i(t)\rangle = 4D_{t,2D}\delta(\Delta t) + V^2\cos(\omega\Delta t)\exp(-D_{r,2D}\Delta t), \qquad (5.4)$$

where $\delta(\Delta t)$ is the Dirac distribution. The first term is related to the 2D translational Brownian diffusion that is present for both passive and active colloids. The second term accounts for the active motion and the change of motion persistence due to the Brownian rotation.

Given the severe slowing down of out-of-plane rotation, such an equation should still hold in our system with $D_{t,2D}=D_t$ (the translational diffusion coefficient at the interface) and $D_{r,2D}= D_{r,||}$, see Fig. 5.2(B).

Hence, we used equation 5.4 to extract the diffusion $D_{r,||}$ (and the velocity V, which agrees with V by *MSD* analysis (not shown)). Since for rectilinear-like trajectory ω= 0, data shown in Figure 5.10(B) were fitted using the second term of equation 5.4:

$$<\boldsymbol{v}(t+\Delta t)\cdot\boldsymbol{v}(t)> = V^2 \exp(-D_{r,||}\Delta t), \qquad (5.5)$$

for $\Delta t > \Delta t_1$, and assuming a negligible drift velocity. In Fig. 5.10(C), $D_{r,||}$ is compared to the bulk rotational diffusion $k_BT/(8\pi\eta R^3)$ and the rotational diffusion expected for half immersed sphere (α = 90°) in non-slip boundary condition $k_BT/(4\pi\eta R^3)$ and in absence of dissipation due to the interface fluctuations. $D_{r,||}$ shows a certain variability for different particles and trajectories, which explains the relatively large error bars (as standard deviations) shown in Fig. 5.10(C). In any case, it seems that $D_{r,||}$ is comparable or even lower than the bulk value at low fuel concentration. It may agree with the expected value at high fuel concentration being $k_BT/(8\pi\eta R^3) < D_{r,||} < k_BT/(4\pi\eta R^3)$ and the Janus colloid contact angle ($\alpha_{J,R}$ = 50° ± 6° $\alpha_{J,A}$ = 64 ± 2°, see section 5.4.2) lower than α = 90°.

Finally, these results clearly show a significant increase in motion persistence for active Janus colloids at the air-water interface given the severe slowing down of $D_{r,\perp}$, the significant slowing down of $D_{r,||}$ (at low fuel concentrations) and an active velocity V at the interface about twice the bulk value. This result is clearly illustrated in Fig. 5.10(D), where a two dimensional projection of an active bulk trajectory is compared with a trajectory at the interface in similar conditions.

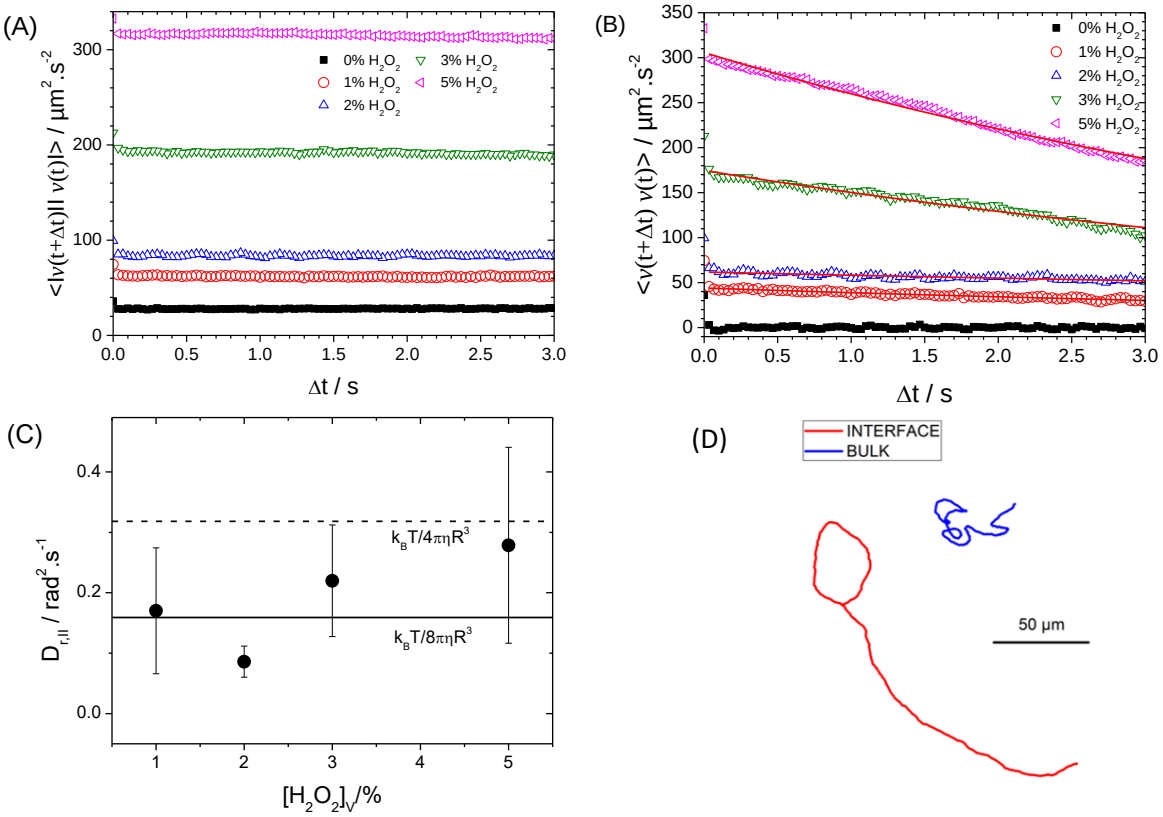

Figure 5.10 (A) Velocity modulus autocorrelation function as a function of the lag time for different $[H_2O_2]_V$. (B) Velocity vector autocorrelation function as a function of the lag time for different $[H_2O_2]_V$. (C) Interfacial rotational diffusion $D_{r,||}$ as a function of $[H_2O_2]_V$. (D) Trajectories of a Janus particle at the water interface and projected trajectory in bulk water at $[H_2O_2]_V$ =5% for t = 16 s.

5.5.4 Interfacial Rotational diffusions for circular-like active trajectories

To further investigate the slowing down of the rotational diffusions for active particles at the interface we now consider the active circular-like trajectories shown in Fig. 5.7.

Ideally symmetrical and spherical Janus colloids are expected to move actively along a straight line, because of the symmetry plane formed by its axis and the *z*-axis; see Figure 5.11(A) and 5.2. For non-ideal Janus colloids as in Fig. 5.11(B), however, this symmetry is broken by the non-uniform surface properties. As a consequence, besides the linear active velocity *V*, there is a finite angular velocity ω about the *z*-axis; see Figure 5.11(B).[41]

In Fig. 5.7, we noted that the rotation direction of the trajectory keeps always the same (in the experimental time window of 20 seconds and for each measurement). We observed both clockwise CW and counter clockwise CCW rotations in all the different experiments and for different beads. Note, however, that for each trajectory, we never observed a switch of the rotation direction during the experiment. In the bulk far from the solid interface, in contrast, we observed that the rotation direction of the projected three dimensional trajectories can switch during the active motion.[35] This observation confirms the severe slowing down of $D_{r,\perp}$ at the interface, which prevents the particle to spin about the motion direction (see Fig. 5.11); and explains why the trajectories at the interface keep always the same rotation direction.

To measure the rotational diffusion coefficient $D_{r,||}$ for circular-like trajectories, we performed image analysis in order to detect the orientation φ of different Janus particles within the interfacial plane (see Fig. 5.11(A)) and calculate the mean squared angular displacement $MSAD(\varphi)$ as shown in Fig. 5.12(A). Data were fitted by:[40]

$$MSAD(\varphi) = 2D_{r,||}\Delta t + \omega^2\Delta t^2. \qquad (5.6)$$

Equation 5.6 was obtained (as eq. 5.4) from a two dimensional Langevin description of the active motion where the propulsion velocity, angular velocity and the rotational diffusion are assumed to be constants and decoupled from each other.[40]

In Fig. 5.12(A), the *MSAD* is linear with the lag time for passive Brownian particles (V=ω=0) and the parabolic behavior is observed in active conditions. The fit of *MSAD* using equation 5.6 leads to the values of $D_{r,||}$ and the modulus of ω. In Figure 5.12(B), we plotted $D_{r,||}$ as a function of ω and the theoretical rotational diffusion coefficients (as in Fig. 5.10(C)). For $\omega < 1.5$ rad.s^{-1}, $D_{r,||}$ is lower than the bulk diffusion coefficient by a factor 2 to 5. For $\omega > 1.5$ rad.s^{-1}, $D_{r,||}$ increases and becomes about 1.5 times $D_{r,b}$. We have already discussed the slowing down of the rotational diffusion for passive Janus particles (ω = 0) in terms of a rotational line friction due to contact line fluctuations $\zeta_{r,L}$ (equation 4.21) in Chapter 4, section 4.5. $D_{r,||}$ also agrees with measurements on low-aspect ratio ellipsoidal particles.[42,43]

The increase of the $D_{r,||}$ with the particle activity ω for circular-like trajectories agrees with the increase of the $D_{r,||}$ with the active velocity V shown in Fig. 5.10(C) for rectilinear-like trajectories. It is important to notice that at high activities $D_{r,||}$ agrees with the hydrodynamic prediction $k_BT/(8\pi\eta R^3) < D_{r,||} < k_BT/(4\pi\eta R^3)$. Hence, these results point to a vanishing of the rotational line friction due to contact line fluctuations in the presence of an increasing persistent velocity. The vanishing of the rotational line friction result can be rationalize considering that the relative motion of the solid particle surface and liquid due to ω leads to a shorter characteristic time τ_L (equation 4.16) or contact line displacement λ, and consequently a decrease of line friction $\zeta_{r,L}$ (equation 4.21). In order to test this hypothesis we should compare the characteristic time of the persistent motion and τ_L describing the contact line dynamics. A time t^* to travel a distance λ associated to the angular velocity ω can be calculated. On the wetted perimeter, the displacement λ defines an arc $\lambda/R = \omega\, t^*$ and $t^* = \lambda/(R\,\omega)$. In the experimental range $0.1<\omega/\text{rad.s}^{-1}<3$, t^* varies from $5\ 10^{-3}$ to $1.6\ 10^{-4}$ s which is comparable to τ_L (equation 4.16, for typical values of λ). Hence, an increase of motion persistence due to ω could indeed affect the rotational line friction.

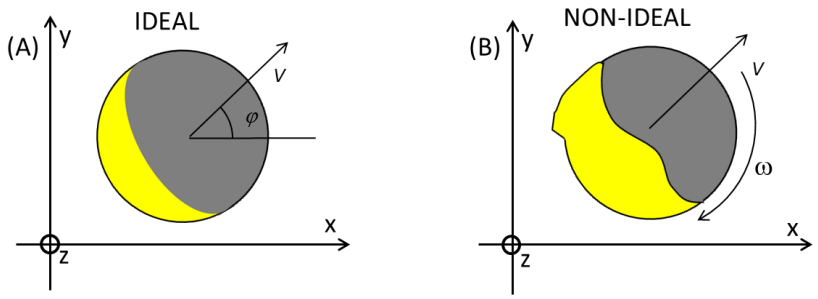

Figure 5.11 Top view sketches of: (A) an ideal symmetric Janus colloid attached onto a gas-liquid interface; (B) a non-ideal Janus colloid with a broken symmetry and related linear active velocity V and angular velocity ω.

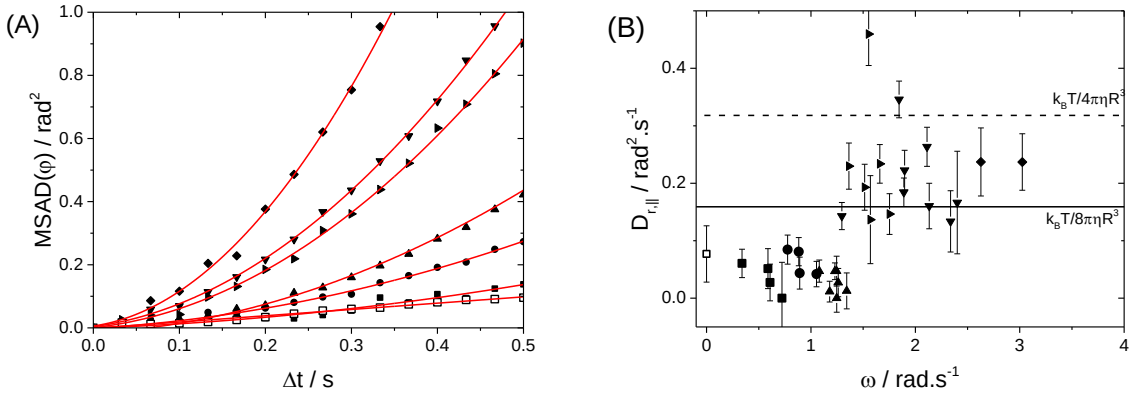

Figure 5.12 (A) Mean squared angular displacement at the air-water interface for a passive (open square symbols) and active Janus colloids of different angular velocities (filled symbols) plotted as a function of the lag time. Solid lines are the fits to the data points using equation 5.6. (B) $D_{r,\|}$ as a function of the particle angular velocity. The point at ω = 0 corresponds to the measurement of Brownian Janus colloid in absence of H_2O_2. Different symbols correspond to different particles and different points are obtained at different times. The solid and dashed lines respectively represent the theoretical bulk rotational diffusion and the rotational diffusion coefficient about the interface normal for an half immersed particle.

Alternatively, we discussed the increase of $D_{r,||}$ with the particle activity in terms of time-dependent fluctuations of the slip velocity on the colloid due to contact line displacement. Indeed, nanometric jumps[42] of the contact line may locally modify the slip velocity at the particle surface and thus induce temporal fluctuations of the velocities, $V = V_0 + \delta V$ and $\omega = \omega_0 + \delta\omega$. Given that the characteristic fluctuation time τ_L of the contact line jumps is shorter than the experimental time scale,[42] the angular mean-square displacement becomes:

$$MSAD(\varphi) = 2\left(D_{r,\|} + \delta\omega^2\tau_L\right)\Delta t + \omega_0^2\Delta t^2. \qquad (5.7)$$

Hence, an additional contribution should be accounted in the linear term of the *MSAD* (see equation 5.6). In equation 5.7, the additional contribution to the linear term of the *MSAD* contains $\delta\omega^2$, which in a good approximation increases with the square of ω. Therefore, this increase could explain the trend of the data of Figure 5.12(B).

5.5.5 Translational diffusion for circular-like active trajectories

For circular-like active trajectories; discrete velocity autocorrelation functions $<\boldsymbol{v}(t+\Delta t)\cdot\boldsymbol{v}(t)>$ for different angular velocities ω are plotted in Figure 5.13(A).

For passive colloids (V=ω=0), the diffusion coefficient D_t can be extracted from the particle

discrete velocity autocorrelation function at Δt=0 s since the mean displacement Δr follows $<\Delta r^2>=4D_t$ Δt and the velocity is:[44]

$$v^2 = \Delta r^2/\Delta t_1^2 = 4D_t/\Delta t_1. \quad (5.8)$$

In Figure 5.13(A) (and 5.12(B)), for both passive and active measurements at the air-water interface, discrete autocorrelation functions show a clear step between $\Delta t = 0$ and $\Delta t = \Delta t_1 = 1/30$ s, which is connected to the first term of equation 5.4. For passive measurements, the autocorrelation drops to zero, since $<\boldsymbol{v}(t+\Delta t)\cdot\boldsymbol{v}(t)> = 0$ for $\Delta t > \Delta t_1$.[45]

In the case of active colloids, at Δt_1 the autocorrelation does not drop to zero but instead gives the square of the propulsion speed, $<\boldsymbol{v}(t+\Delta t_1)\cdot\boldsymbol{v}(t)>\approx V^2$.Since $<\boldsymbol{v}(t)\cdot\boldsymbol{v}(t)>= 4D_t/\Delta t_1+V^2$, D_t can be obtained from: $D_t \approx 1/4\ [<\boldsymbol{v}(t)\ \boldsymbol{v}(t)> - <\boldsymbol{v}(t+\Delta t_1)\ \boldsymbol{v}(t)>]\ \Delta t_1$. In Figure 5.13(B), we plot the ratio between D_t and the calculated diffusion coefficient in the bulk as a function of the angular velocity modulus.

The ratio $D_t/D_{t,b}$ keeps approximately constant in the ω range where $D_{r,||}$ increases (see Figure 5.12(B)). It is important to note that for passive colloids (V=ω=0), the slowing down of D_t is not as severe as $D_{r,||}$ and for this reason it is difficult to discuss on a possible increase of D_t with ω.

Data shown in Figure 5.13(A) were fitted using the second term of equation 5.4 adding a term accounting for a constant drift velocity V_d (note that drift is ubiquitous in diffusion experiments, in particular at the interface due to advection flows):

$$<\boldsymbol{v}(t+\Delta t)\cdot\boldsymbol{v}(t)> = V^2\cos(\omega\Delta t)\exp(-D_{r,||}\Delta t) + V_d^2, \quad (5.9)$$

for $\Delta t > \Delta t_1$. The expected autocorrelation function is therefore an oscillating cosine function damped by the $\exp(-D_{r,||}\Delta t)$ term, which fits the data shown in an excellent way.

In presence of an oscillating function, one could clearly distinguish between V and V_d , being V_d^2 the mean value around which the velocity autocorrelation function oscillates. Values of the drift velocities measured here are comparable to the drifts previously reported for bare particles at different H_2O_2 concentrations:[23] $V_d = 1\pm1$ μm/s for $[H_2O_2]_V = 1$ %, $V_d = 2\pm2$ μm/s for $[H_2O_2]_V = 2$ %, $V_d = 1\pm1$ μm/s for $[H_2O_2]_V = 3$ % and $V_d = 3\pm3$ μm/s for $[H_2O_2]_V = 5$ %, see Figure 5.7. A good agreement is also found between the angular velocity ω obtained by the *MSAD* analysis (orientation angle φ obtained by image processing) and ω by the velocity autocorrelation function. Unfortunately, reliable values of $D_{r,||}$ could be not obtained by the velocity autocorrelation function because of the low damping measured in the lag time range where data can be safely fitted ($\Delta t < 3$ s).

Before ending this section, it is important to point out that for circular-like trajectories, V increases with the angular velocity ω but we did not find a systematic increase of V with the fuel concentration as for rectilinear-like trajectories. We could model this finding by introducing the asymmetry of the particle as a parameter to be accounted in the particle self-propulsion mechanism.

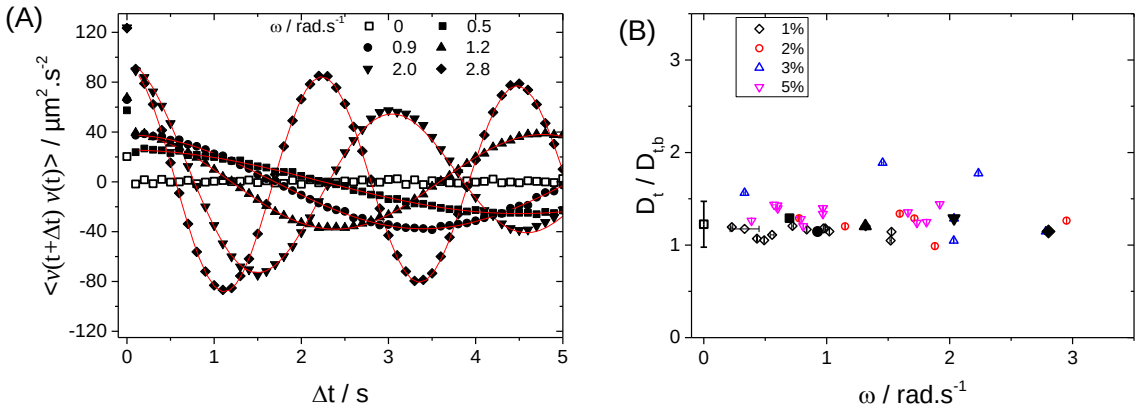

Figure 5.13 (A)Velocity vector autocorrelation function as a function of the lag time Δt for some given ω (in the legend). Solid lines are the fits to the data points using Eq. 5.8. (B) Measurements of translational diffusion at the air-water interface divided by the calculated bulk diffusion $D_{t,b}$ as a function of ω.

Within this model, we can show that particle shape asymmetries even in the nanometer range could affect the active velocities in a comparable way as an increase of few per cent of fuel concentration. Hence, we pointed out to the crucial role of particle fabrication in the control of the Janus colloid active motion.

5.6 Conclusion

We can now summarize the results reported in the previous sections. Janus colloids able to self-propelled at the gas-liquid interface have been fabricated and active motion has been observed. Here, colloids are irreversibly adsorbed onto the interface and their motion is truly two dimensional. We noted that platinum coating roughness and shape may impact dramatically both the wetting and the particle motion at the interface. Janus colloid contact angle hysteresis and metastable particle orientations at the gas-liquid interface have been observed and explained in terms of contact line pinning.

Rectilinear-like trajectories with velocity V tunable with the H_2O_2 fuel concentration as high as 18 μm/s have been measured and represent the 72% of the whole active trajectories observed. These rectilinear-like trajectories can be associated to the particles showing negligible shape asymmetry. The rest of the trajectories observed are circular-like and are performed by particles possessing asymmetric platinum coating shapes, which lead to both active linear V and angular ω velocities.

Compared to the motion observed in the bulk, active motion persistence is highly enhanced due to the slowing down of the rotational diffusion. Rotational diffusion about an axis in the interfacial plane $D_{r,\perp}$ is dramatically slowed down because of the high dissipation occurring close to the contact line.[46,47] This rotation in fact involves the wetting of a dried colloid region and the dewetting of an opposite wetted region. Hence, the corresponding dissipation can be described as in partial wetting and dewetting of drops on solid surfaces.

As described in Chapter 4 for passive Janus and ellipsoidal particles at the interface, rotational diffusion about an axis parallel to the interfacial normal $D_{r,||}$ can be also significantly slowed down.[48] These slowing down can be modeled as an extra friction due to the contact line fluctuations if the particle shape deviates from being spherical. Here, we have also measured a correlation between $D_{r,||}$ and the particle active velocities (V or ω). For low velocities, $D_{r,||}$ is significantly slowed down as for passive particles; but for relatively high velocities $D_{r,||}$ increases and becomes comparable to the hydrodynamic viscous prediction.

To conclude, we have investigated the active motion of Janus colloids in the two dimensional confinement given by a gas-liquid interface. This system can be considered as a model for other complex confinements such membranes, pores and cell compartments. Here, confinement effects dramatically affect motion persistence; and colloid self-propulsion is highly coupled with partial wetting dynamics and Brownian diffusions. We have also shown that both the H_2O_2 fuel concentration and particle shape asymmetry (due to particle fabrication) affect active motion dynamics. Finally, we believe that future investigations focusing on the effects of other forms of confinements on the motion of active particles in diluted and concentrated regimes will contribute to the advancement in the field of active matter. Improving active colloid fabrication to obtain large productions with highly controlled motion will be also required in order to probe dynamics in concentrated active matter systems.

5.7 References

1 P. Tierno, R. Albalat and F. Sagués, *Small*, 2010, **6**, 1749–52.
2 S. Gangwal, O. Cayre, M. Bazant and O. Velev, *Phys. Rev. Lett.*, 2008, **100**, 58302.
3 S. Saha, R. Golestanian and S. Ramaswamy, *Phys. Rev. E*, 2014, **89**, 62316.
4 B. El Pinchasik, H. Möhwald and A. G. Skirtach, *Small*, 2014, **10**, 2670–2677.
5 Z. Wang, H.-Y. Chen, Y.-J. Sheng and H.-K. Tsao, *Soft Matter*, 2014, **10**, 3209–17.
6 J. Howse, R. Jones, A. Ryan, T. Gough, R. Vafabakhsh and R. Golestanian, *Phys. Rev. Lett.*, 2007, **99**, 48102.
7 R. Golestanian, T. Liverpool and A. Ajdari, *Phys. Rev. Lett.*, 2005, **94**, 1–4.
8 S. Ebbens, M.-H. Tu, J. Howse and R. Golestanian, *Phys. Rev. E*, 2012, **85**, 20401.

9 S. Ebbens, D. Gregory, G. Dunderdale, J. Howse, Y. Ibrahim, T. B. Liverpool and R. Golestanian, *Eur. Phys. Lett.*, 2014, **106**, 58003.
10 A. Brown and W. Poon, *Soft Matter*, 2014, **10**, 4016–4027.
11 J. G. Gibbs and Y.-P. Zhao, *Appl. Phys. Lett.*, 2009, **94**, 163104.
12 U. Choudhury, L. Soler, J. G. Gibbs, S. Sanchez and P. Fischer, *Chem. Commun.*, 2015, **51**, 8660–3.
13 S. Ebbens, D. a. DA Gregory, G. Dunderdale, J. R. Howse, Y. Ibrahim, T. B. Liverpool and R. Golestanian, *EPL (Europhysics Lett.*, 2014, **106**, 58003.
14 D. a. Gregory, A. I. Campbell and S. J. Ebbens, *J. Phys. Chem. C*, 2015, **119**, 15339–15348.
15 R. J. Archer, A. I. Campbell and S. Ebbens, *Soft Matter*, 2015, **11**, 6872–6880.
16 A. B. Pawar and I. Kretzschmar, *Langmuir*, 2009, **25**, 9057–9063.
17 J. G. Gibbs and Y.-P. Zhao, *Small*, 2009, **5**, 2304–8.
18 Y. He, J. Wu and Y. Zhao, *Nano Lett.*, 2007, **7**, 1369–75.
19 F. Kümmel, B. ten Hagen, R. Wittkowski, I. Buttinoni, R. Eichhorn, G. Volpe, H. Löwen and C. Bechinger, *Phys. Rev. Lett.*, 2013, **110**, 198302.
20 A. Nourhani, S. J. Ebbens, J. G. Gibbs and P. E. Lammert, 2016, **30601**, 1–5.
21 A. Girot, N. Danné, A. Würger, T. Bickel, F. Ren, J. C. Loudet and B. Pouligny, *Langmuir*, 2016, **32**, 2687–2697.
22 H. Moyses, J. Palacci, S. Sacanna and D. G. Grier, *Soft Matter*, 2016, **12**, 6357–6364.
23 X. Wang, M. In, C. Blanc, M. Nobili and A. Stocco, *Soft Matter*, 2015, **11**, 7376–7384.
24 C. Casagrande, P. Fabre, E. Raphaël and M. Veyssié, *Europhys. Lett.*, 2007, **9**, 251–255.
25 T. Ondarçuhu, P. Fabre, E. Raphaël and M. Veyssié, *J. Phys.*, 1990, **51**, 1527–1536.
26 S. N. Z. Hórvölgyi J. H. Fendler, *Colloids Surf. A Physicochem. Eng. Asp.*, 1993, **71**, 327.
27 V. N. Paunov, *Langmuir*, 2003, **19**, 7970–7976.
28 J. C. Love, B. D. Gates, D. B. Wolfe, K. E. Paul and G. M. Whitesides, *Nano Lett.*, 2002, **2**, 891–894.
29 T. Karabacak, *J. Nanophotonics*, 2011, **5**, 52501.
30 Z. Li, P. Beck, D. a. . Ohlberg, D. R. Stewart and R. S. Williams, *Surf. Sci.*, 2003, **529**, 410–418.
31 B. P. Binks and J. H. Clint, *Langmuir*, 2002, **18**, 1270–1273.
32 J. R. Gardner and R. Woods, *J. Electroanal. Chem. Interfacial Electrochem.*, 1977, 81, 285–290.
33 V. Leo, A. Tusa, Y. C. Araujo and V. Leo, 1999, **155**, 131–136.
34 B. J. Park, T. Brugarolas and D. Lee, *Soft Matter*, 2011, **7**, 6413.
35 X. Wang, M. In, C. Blanc, A. Würger, M. Nobili and A. Stocco, *Langmuir*, , DOI:10.1021/acs.langmuir.7b02353.
36 J. Palacci, C. Cottin-Bizonne, C. Ybert and L. Bocquet, *Phys. Rev. Lett.*, 2010, **105**, 88304.
37 T. M. Fischer, P. Dhar and P. Heinig, *J. Fluid Mech.*, 2006, **558**, 451.
38 T. Gehring and T. M. Fischer, *J. Phys. Chem. C*, 2011, **115**, 23677–23681.
39 M. E. O'Neill, K. B. Ranger and H. Brenner, *Phys. Fluids*, 1986, **29**, 913.
40 S. Ebbens, R. A. L. Jones, A. J. Ryan, R. Golestanian and J. R. Howse, *Phys. Rev. E - Stat. Nonlinear, Soft Matter Phys.*, , DOI:10.1103/PhysRevE.82.015304.
41 D. Debnath, P. K. Ghosh, Y. Li, F. Marchesoni and B. Li, *Soft Matter*, 2016, **12**, 2017–2024.
42 G. Boniello, C. Blanc, D. Fedorenko, M. Medfai, N. Ben Mbarek, M. In, M. Gross, A. Stocco and M. Nobili, *Nat. Mater.*, 2015, **14**, 908–11.
43 G. Boniello, A. Stocco, M. Gross, M. In, C. Blanc and M. Nobili, *Phys. Rev. E*, 2016, **94**, 12602.
44 X. Bian, C. Kim and G. E. Karniadakis, *Soft Matter*, 2016, **12**, 6331–6346.
45 A. P. Philipse, 2011, p. http://userpages.umbc.edu/~dfrey1/ench630/philipse.
46 D. M. Kaz, R. Mcgorty, M. Mani, M. P. Brenner and V. N. Manoharan, *Nat. Mater.*, 2012, **11**, 138–42.
47 T. D. Blake, *J. Colloid Interface Sci.*, 2006, **299**, 1–13.
48 G. Boniello, C. Blanc, D. Fedorenko, M. Medfai, N. Mbarek, M. In, M. Gross, A. Stocco and M. Nobili, *Nat. Mater.*, 2015, Doi:10.1038/nmat4348.

Perspectives

Janus Colloids and Biomimetic Membranes

6.1 Introduction

From Chapter 1 to Chapter 5, I have chosen to present topics on the interactions and dynamics between colloidal particles and interfaces, which are composed of simple fluids. In terms of perspectives, in this chapter I would like to address research challenges and opportunities in investigating transitions and dynamics of Janus particles at complex interfaces as lipid bilayers or biomimetic membranes.

In the following years, I plan to refocus my research activities on biomimetic membranes and biophysics. As a starting project, I wish to apply some of the knowledge acquired in wetting and active motion of Janus colloids to develop tasks on biomimetic membranes and vesicles. A first task is to control endocytosis of colloidal particles inside biomimetic vesicles. Hence, I wish to study the active motion of vesicles in the presence of active colloids partially engulfed by the membrane.

6.2 Context

Endocytosis, exocytosis and phagocytosis of micro- and nano- particles in biological membranes are relevant processes that the cell controls by many passive and active, fuel-consuming mechanisms. Two examples of these processes are connected to toxicity and drug delivery. In the last years, toxicity of particles in biological cells has becoming an important societal issue given the large use of nanoparticles in food, medical and cosmetic products. Still the effects of particles on cell functions are not clear yet, and the key parameters (surface chemistry, size, shape, rigidity, etc) controlling the particle-cell membrane interaction have not be established. In drug delivery, particles can be used as vehicles transporting drug cargo inside the cell; and also in this case there is a lack of knowledge on the particle design to obtain an efficient particle transport and drug deliver. For these reasons, investigating the motion and interaction of particles with membranes is of a paramount importance in order to control endocytosis, exocytosis, in order to support or hinder the wrapping of particles by membranes.

Few experimental investigations have been reported on the different transitions that bare particles may undergo when they come into contact with a biological or biomimetic membrane, see refs 6-10 in Agudo-Canalejo *et al.*.[1] From the theoretical side, it was first predicted that the particle engulfment process is controlled only by the adhesive strength of the particle on the membrane and by the bending energy of the membrane.[2] When the particle approaches the membrane, if the adhesive strength of the particle dominates over the resistance of the membrane to bend, the membrane starts to spread on or it wraps the particle surface. In analogy with the physics of wetting,[3] one can define (i) a free state *F* (non-wetting) of the particle, (ii) a partial engulfed *P* (partial wetting) state, when the membrane wraps only partially the particle surface, and (iii) a complete engulfed *C* (complete wetting) state when all the particle becomes surrounded by the membrane except for a small neck, see Fig. 6.1(A) (Janus particles behave as bare particles if the two faces have similar properties). Such neck can be stable or not and leading, in the last case, to the particle crossing through the membrane.[1,4]

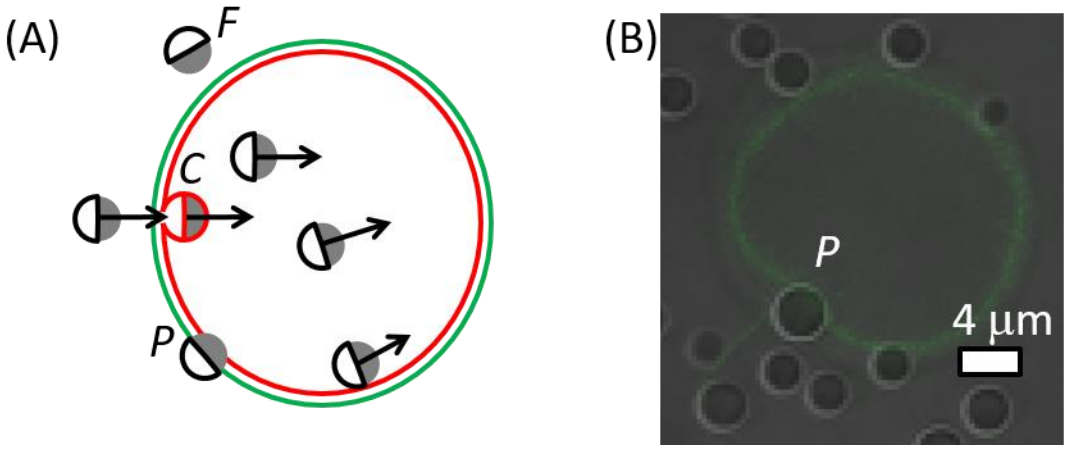

Figure 6.1 (A) Sketch of engulfment regimes: *F* is the free state, *C* is the complete engulfed state and *P* is the partially engulfed state. A bistable *B* regime corresponds to a transition state between *F* and *C* (Janus particles behave as bare particles if the two faces have similar properties).[1] (B) Preliminary experiment (bright field and fluorescent microscopy) showing a fluorescent DOPC phospholipid unilamellar vesicle and silica colloids with one bare silica particle in *P*.

6.3 Objectives

A key aim of my future research is to investigate experimentally active and passive particles in interaction with biomimetic membranes such as lipid bilayers of unilammellar vesicles (see Fig. 6.1). Janus particles possessing two faces with different adhesion properties will be used to control the membrane wrapping and the particle engulfment regimes. First, I aim at finding experimental conditions to realize partial and complete particle engulfment by the membrane. Once partial and complete engulfment regimes will be controlled, I will investigate the self-propulsion of the Janus particles to let the membrane perform active tasks. I will investigate active colloids working both with an internal fuel (as H_2O_2 for Pt-coated particles) and an external field fuel (as electric or light fields). Effects of the internal fuel and external fields on on the lipid membranes and vesicles will be also investigated and controlled. In particular, I plan experimental investigations on (i) vesicle transport by self-propelled particles in partial engulfment and (ii) driven particle endocytosis or encapsulation inside the vesicle in the completely engulfed regime. Self-propelled particles encapsulated inside lipid vesicles may create "active membranes" able to undergo driven shape changes and to perform active motion.

Expected results connected to the two main targets of this project are described in the following.

6.3.1 Four particle engulfment regimes and lateral force due to membrane curvature gradient

Recent theoretical studies have clarified the stability and regimes of particle engulfment[1] and point out to new fascinating phenomena[5] to be scrutinized by accessible experiments. The spontaneous curvature of the membrane *m*, which represents the asymmetry in the bilayer structure of a vesicle, is a new parameter controlling particle engulfment. Hence, a qualitative different behavior is expected depending on the particle original location: if the particle was inside or outside the vesicle. Membranes owing $m>0$ can adopt the shape needed to support exocytosis (i.e. particle transfer from the inside to the outside of the lipid vesicle); whilst for $m<0$ endocytotic (i.e. particle transfer from the outside to the inside of the lipid vesicle) processes can be favored. Two critical particle sizes R_F and R_E determine four distinct engulfment regimes for bare particles. Depending on the local curvature of the membrane and the particle adhesion (which can be tuned by the particle size), particles are expected to either remain free (regime 1: *F*), become completely (regime 2: *C*) or partially (regime 3: *P*) engulfed by the membrane see Fig. 6.1(A). A bistable state (regime 4: *B*) was also predicted, which is characterized by particles able to switch between the free and the completely engulfed state.

If the particles are smaller than the lower critical size min(R_F, R_E), they do not interact with the membrane and remain in a non-adhered state (regime 1: *F*). If the particle size instead exceeds the upper critical size max(R_F, R_E), the particles are completely engulfed by the membrane (regime 2: *C*). For particle sizes in between min(R_F, R_E) and max(R_F, R_E), two regimes can be distinguished: a stable partial engulfment state (regime 3: *P*) if $R_F < R_E$ and a bistable state if $R_F > R_E$ (regime 4: *P*). It is important to note that the both critical sizes depend on adhesion strength, bending and mean curvature of the membrane. However, R_F does not depend on the spontaneous curvature *m* whilst R_E depends strongly on *m*.[1] Hence, different regimes can be also observed for a given bare particle size by tuning *m* by adsorption or depletion of molecular species or surfactants on the outer layer of the lipid membrane.[6,7]

Here, I plan dedicated experimental investigations in order to explore four particle engulfment regimes by tuning both particle and lipid membrane properties. I will start focusing on systems showing weak or ultraweak adhesion of the order of $10^{-5}…10^{-4}$ mJ/m² as DOPC (1,2-Dioleoyl-sn-glycero-3-phosphocholine) phospholipid-silica particle systems.[1] In these systems, typical critical particle sizes (R_F, R_E) are few micrometers, which are easily accessible experimentally by optical microscopy, see Fig. 1(B).

I also consider to investigate lipid membranes showing very low or even negative line tensions such as DMPG (1,2-Dimyristoyl-sn-glycero-3[Phospho-rac-(1-glycerol)]) and phospholipid membranes in the presence of cholesterol or surfactants at different compositions.[8,7,9] The concept of edge tension in lipid bilayers is usually connected to the nucleation of pores in the membrane, which is immersed inside a fluid.[10] In Chapter 1 and 2, the line tension was instead associated to the energy of the line where three phases (solid-gas-liquid) meet. Here, for particle-membrane systems, one should consider the energy of the line defined by a hole of the membrane in contact with a solid particle. As a function of the energy of such (membrane-particle-fluid) line and the bending energy of the membrane, one could observe scenarios different from the ones predicted before. For negative membrane-particle-fluid line tension systems, in order to maximize this line energy gain the membrane could nucleate a hole around the particle. Hence, the membrane would be located at an equatorial plane of the particle without any bending or wrapping on the particle surface.

Agudo-Canalejo and Lipowsky also predicted that the binding energy of a partially engulfed particle depends on the local curvature of the membrane in the absence of the particle.[5] Hence, the free energy of a particle can differ along the membrane regions owing different local curvatures. A local lateral force due to curvature gradient could manifest and act on the partially engulfed particles and move them along the membrane towards regions with lower and higher curvature depending on the original location of the particle. To probe the existence of such lateral force, partially engulfed Janus particles are convenient experimental systems given that they can be designed with one adhesive and one non-adhesive surface domain, see Fig. 6.1(B).[5] In this context, I am currently performing preliminary experiments on bare particles (silica, platinum, titania) with different surface chemistry in order to elucidate on the adhesiveness of the two faces of the Janus particle. In order to create curvature gradients in the membrane and probe the motion of partially engulfed particles, electric fields able to deform the shape of lipid vesicles could be used.[11]

6.3.2 Particle self-propulsion: consequences for vesicle transport and membrane crossing

Once partial and complete engulfment regimes will be controlled, I will exploit the self-propulsion of the Janus particles to let the membrane perform active tasks.

Here, I plan experimental investigations on (i) vesicle transport and (ii) colloid encapsulation inside the vesicle by exploiting particle self-propulsion. Active particles encapsulated inside lipid vesicles may create “Active membranes” able to undergo driven shape changes and perform active motion.

(i) In the case of vesicle transport, I plan to study the active motion of a Janus particle partially engulfed by a vesicle owing a larger but comparable dimension. Here, I plan to design experiments with Janus colloids possessing only one adhesive face and therefore always partially engulfed by the membrane. Janus colloid self-propulsion will be triggered either by adding some fuel (as H_2O_2 for Pt-coated particles) or by applying an external field fuel (as electric or light fields). In this way, I expect to tune the particle velocity and the transport of the particle-vesicle system.

(ii) Another scenario could be predicted in the complete engulfment regime (for Janus colloids

possessing both adhesive faces) when the vesicle dimension is significantly larger than the particle size. In the latter case, the vesicle could deform significantly and the net particle propulsion could accelerate the instability of the membrane neck, which results in the encapsulation of the active particle inside the lipid vesicle, see Fig. 6.1(B). Upon encapsulation of few active particles, I will explore not only the active motion of particles crowded inside the vesicle but also if the interaction between the active particles and lipid membranes leads to the active motion of the whole vesicle or to vesicle shape fluctuations and deformations. Such scenario has been recently theoretically modelled for active particles inside a vesicle or in a rigid compartment.[12,13] Different kinds of motion ranging from enhanced random motion, circling and run-and-circle motion could emerge depending on the membrane rigidity and the interactions of the active particles with the membrane.[13]

Before ending this part, one remark should be made. If the transfer of particles inside the lipid vesicle leads to a lipid coating on the Janus particles, one may wonder if the self-propulsion mechanism is still effective or if the lipid coating inhibits the active motion. If the last scenario occurs, membranes showing low or even negative line tensions could be used to hinder the membrane wrapping on the particle as it was already discussed in the previous section. In these membrane systems, the active particle may cross the lipid membrane by nucleating a hole in the lipid bilayer; thus avoiding a lipid coating on the particle.

6.4 Methods and Experimental plan

I will start investigating experimental systems well characterized in literature as giant unilammellar vesicles GUV made of phospholipids. GUV will be fabricated by electroformation or a gel-assisted method in collaboration with the Mcube team at the Institut Charles Sadron, Strasbourg.[14,15] Bare and Janus colloidal particles in the micrometer range size with different surface coating will be investigated. Janus particles will be fabricated starting from bare particles half coated by thin layers of titanium, gold or platinum by sputtering depending on the self-propulsion mechanism.[16,17,18,19]

These experimental systems will be investigated by optical, fluorescent, confocal microscopy. In the next future, I also wish to develop an expertise on two experimental methods: (1) optical tweezers to control the interaction between particle and membrane, and (2) micropipette experiments to monitor the membrane tension and bending.

In a first set of experiments, I aim at observing and controlling the four engulfment regimes (see section 6.3.1). I will focus on GUV larger than the colloid size and on spherical colloids. The adhesive strength will be tuned by changing the particle size from 500 nm to 5 µm and the surface chemistry of the particle surfaces. Membrane spontaneous curvature will be tuned by adsorption or depletion of molecular species or surfactants on the outer side of the membrane. In a second series of experiments, I aim at investigating the motion of partially engulfed particles due to gradients in the membrane curvature (see section 6.3.1). Particle attached to the membrane will be followed by particle tracking and co-localized with respect to the membrane curvature. Finally, I will focus on self-propelled Janus particles in partial or in complete engulfment regimes (see section 6.3.3). In the latter regime, I aim at encapsulating active particles inside the vesicles to observe active motion of lipid vesicles and active membrane dynamics.

References

1 J. Agudo-Canalejo and R. Lipowsky, *ACS Nano*, 2015, **9**, 3704–3720.
2 R. Lipowsky and H.-G. Döbereiner, *Europhys. Lett.*, 1998, **43**, 219–225.
3 U. Seifert and R. Lipowsky, *Phys. Rev. A*, 1990, **42**, 4768–4771.
4 J. Agudo-Canalejo and R. Lipowsky, *Soft Matter*, 2016, **12**, 8155–8166.
5 J. Agudo-Canalejo and R. Lipowsky, *Soft Matter*, 2017, **13**, 2155–2173.
6 T. P. Sudbrack, N. L. Archilha, R. Itri and K. A. Riske, *J. Phys. Chem. B*, 2011, **115**, 269–277.
7 B. Mattei, R. B. Lira, K. R. Perez and K. A. Riske, *Chem. Phys. Lipids*, 2017, **202**, 28–37.
8 T. Portet and R. Dimova, *Biophys. J.*, 2010, **99**, 3264–3273.
9 A. Tian, C. Johnson, W. Wang and T. Baumgart, *Phys. Rev. Lett.*, 2007, **98**, 18–21.
10 S. A. Akimov, P. E. Volynsky, T. R. Galimzyanov, P. I. Kuzmin, K. V. Pavlov and O. V.

Batishchev, *Sci. Rep.*, 2017, **7**, 1–20.
11 P. M. Vlahovska, R. S. Gracià, S. Aranda-Espinoza and R. Dimova, *Biophys. J.*, 2009, **96**, 4789–4803.
12 M. Paoluzzi, R. Di Leonardo, M. C. Marchetti and L. Angelani, *Sci. Rep.*, 2016, **6**, 34146.
13 C. Abaurrea Velasco, S. Dehghani Ghahnaviyeh, H. Nejat Pishkenari, T. Auth and G. Gompper, *Soft Matter*, 2017, **13**, 5865–5876.
14 A. Weinberger, F. C. Tsai, G. H. Koenderink, T. F. Schmidt, R. Itri, W. Meier, T. Schmatko, A. Schröder and C. Marques, *Biophys. J.*, 2013, **105**, 154–164.
15 Y. M. S. Micheletto, C. M. Marques, N. P. Da Silveira and A. P. Schroder, *Langmuir*, 2016, **32**, 8123–8130.
16 J. Yan, M. Han, J. Zhang, C. Xu, E. Luijten and S. Granick, *Nat. Mater.*, 2016, **15**, 1095–1099.
17 S. J. Ebbens, *Curr. Opin. Colloid Interface Sci.*, , DOI:10.1016/j.cocis.2015.10.003.
18 S. J. Ebbens and J. R. Howse, *Soft Matter*, 2010, **6**, 726.
19 W. Wang, W. Duan, S. Ahmed, T. E. Mallouk and A. Sen, *Nano Today*, 2013, **8**, 531–534.

Acknowledgment

I thank the referees and the members of the jury for having accepted the invitation to assess this work.

During the writing of this Habilitation dissertation, I have made the choice of presenting a selected range of the research I have carried out after my PhD. Consequently I could not describe some relevant contributions I obtained during my postdoctoral positions and other research carried out in Montpellier in the last six years. One important step in my career was my postdoc on nanoparticle stabilised foams and interfaces (LPS, Orsay). This period was very productive and stimulating. For this reason, I want to start to thank Dominique Langevin as the person who influenced the most my scientific career. I thank her for the help, support and encouragement that she gave me.

Before in time, I want to thank Klaus Tauer (MPI Potsdam), who supported me during my PhD. I appreciated the discussions we had, the help he gave me and the lesson how to think "out of the box". I want to thank deeply Helmuth Möhwald (MPI Potsdam) for his support and inspiration. I have learnt fundamental and fascinating aspects of colloid and interface science from him. For the same reason, I want to thank: Dayang Wang, Reinhard Miller, Markus Antonietti and Reinhard Sigel.

Martin In and Maurizio Nobili are extraordinary scientists and persons, who have been helping me and guiding my scientific and personal life in the last six years in Montpellier. I thank them for their advices, discussions, help in proposal writings and teachings in Physics and Physical Chemistry. I am also indebted to Christophe Blanc for the important experimental and theoretical contributions to the activities on active colloids and fluid interfaces. I cannot forget, in this list of people, to thank Michel Gross for discussions on optics and ultrasounds.

I want to thank my Lab director Pierre Lefebvre for his support and kindness during these years. I have also appreciated the work of my Team directors: Julian Oberdisse and Gladys Massiera. I also thank Luca Cipelletti and Christian Ligoure for the help during my first years in Montpellier. I have been very happy and proud to work in the Soft Matter Team in Montpellier and I want to thank all Team members. In particular, I want to thank Laura Casanellas and Domenico Truzzolillo for their friendships and advices.

I would like to express my gratitude to Thomas Zemb and Olivier Diat (ICSM Marcoule) for the support, encouragement and collaboration. I thank Ali Abou-Hassan for introducing me to the field of microfluidics. I need to thank many collaborators and colleagues: Wiebke Drenckhan, Francois Ganachaud Alois Würger, André Vioux, Hubert Mutin, Davide Di Marino, Alexander Böker, Martin Müller, Paolo Malgaretti, Ahmad Mehdi, Gaelle Gassin, Duyang Zang, Bernie Binks, Massimo Bertino, David Carriere, Emanelle Rio, Anniina Salonen, Stergios Pispas, Arnaud Saint-Jalmes, Marc Héran, Benjamin Nottelet, Hervé Cottet and Veronique Pimienta, Ludovic Berthier, Andrea Parmeggiani and Stefano Piccarolo; and I apologize if I forgot anyone.

Now, I thank Carlos Marques and the Mcube Team (ICS, Strasbourg) for the scientific and personal support and for having introduced me to the world of biomimetic membranes.

Finally, I have really appreciated the work of the administrative and technical staff. In particular I wish to thank: Adoration Gabillard, Jean-Christophe Art, Tina Rabeharivelo, Raymond Aznar, Pascal Martinez, Alain Charbit and Pascal Gamet and Christophe Roblin.

List of Symbols

a	characteristic length
A_i	Area
A_H	Hamaker constant
$\mathcal{A}_{eq}$	equilibrium contact angle (line tension)
b	characteristic length (Chapter 1)
b	slip length
B	sliding friction coefficient
B_0	Boussinesq numbers
c_i	concentration
C_0	constant
d	distance/size
$D_{t,i}$	translational diffusion coefficient
$D_{r,i}$	rotational diffusion coefficient
e	elementary charge
E	free energy
E_a	activation energy
f_i	force
$f_{NP,i}$	particle volume fraction
f_0	force per unit length
F_i	Force
g	gravitational acceleration
$g(\alpha)$	function of the contact angle
h_i	distance/height
h_P	Planck constant
J_1	first order deviation parameter
k	line tension
K	spring constant
k_B	Boltzmann constant
k_i^i	numerical friction factor
l	line length/length
l_c	capillary length
l_m	molecular length
l_T	thermal length
L	length/lever arm
MSD	mean squared displacement
$MSAD$	mean squared angular displacement
n	number
N	number
n_i	refractive index
P	energy per unit area
P_0	capillary pressure
q	wave vector
Δr	mean displacement
r	area ratio
r_i	reflection field coefficient
R_i	radius
R_d	droplet base radius
S_0	spreading coefficient
t	time
Δt	lag time
T	temperature
u	displacement
v_i	velocity
v_m	molecular volume
V	active velocity
V_d	drift velocity
V_i	Free energy per unit area
W_i	Work
W	specific energy of a defect

α	contact angle
α_A	advancing contact angle
α_E	equilibrium contact angle
α_L	local contact angle
α_R	receding contact angle
α_S	static contact angle
β	out-of-plane orientation angle
χ	deformation angle
δ_0	distance/height
Δ	phase ellipsometric angle
ε_i	dielectric constant
ϕ	surface coverage
ϕ_i	area fraction
γ_i	liquid-fluid interfacial tension
η_i	viscosity
φ	incident angle
φ	in-plane orientation angle
φ_B	Brewster angle
κ	inverse of the Debye length
λ	line displacement
λ_0	laser wavelength
Π	Disjoining pressure
Θ	in-situ contact angle (ellipsometry)
ρ	density
σ_i	solid-fluid interfacial tension
Σ	local interface curvature
τ_L	characteristic time
τ_r	rotational diffusion time
ν_e	electronic absorption frequency
ω	angular velocity
Ω	power dissipated
ξ	correlation length
ψ_0	surface potential
Ψ	amplitude ellipsometric angle
$\zeta_{r,i}$	rotational friction coefficient
$\zeta_{t,i}$	translational friction coefficient

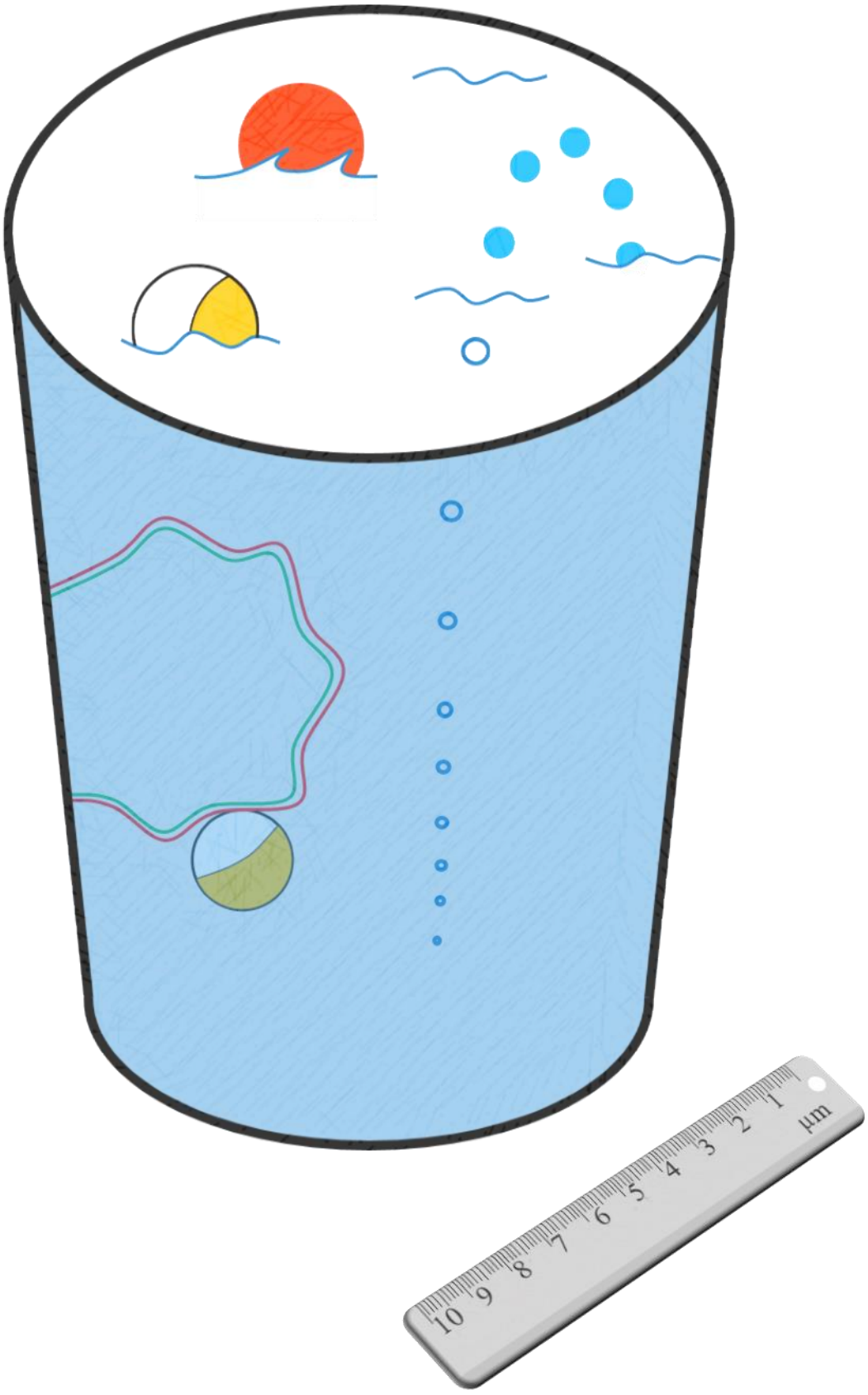
10
9
8
7
6
5
4
3
2
1
µm